MICROSTRUCTURE DESIGN OF MAGNETO-DIELECTRIC MATERIALS
VIA TOPOLOGY OPTIMIZATION

by

YASSER EL-KAHLOUT

Submitted to the Graduate School of Engineering and Natural Sciences
in partial fulfillment of
the requirements for the degree of
Doctor of Philosophy

Sabanci University
Spring 2009

MICROSTRUCTURE DESIGN OF MAGNETO-DIELECTRIC MATERIALS
VIA TOPOLOGY OPTIMIZATION

APPROVED BY:

Asst. Prof. Güllü Kızıltaş Şendur…………………………
(Dissertation Supervisor)

Assoc. Prof. Yunus Erdemli…………………………….

Assoc. Prof. Mahmut F. Akşit……………………………

Asst. Prof. Kürşat Şendur ………………………………...

Assoc. Prof. Meriç Özcan ………………………………

DATE OF APPROVAL: ………………………….

أهديها لأبي، أمي، زوجتي و ولدي

To my Parents, wife and son

Acknowledgement

MICROSTRUCTURE DESIGN OF MAGNETO-DIELECTRIC MATERIALS VIA TOPOLOGY OPTIMIZATION

YASSER EL-KAHLOUT

ME, Ph.D. thesis, 2009

Thesis Supervisor: Asst. Prof. Dr. Güllü Kızıltaş Şendur

Abstract

Engineered materials, such as new composites, electromagnetic bandgap and periodic structures have attracted considerable interest in recent years due to their remarkable and unique electromagnetic behavior. As a result, an extensive literature on the theory and application of artificially modified materials exists. Examples include photonic crystals (regular, degenerate or magnetic) illustrating that extraordinary gain and high transmittance can be achieved at specific frequencies. Of importance is that recent investigations of material loading demonstrate that substantial improvements in antenna performance (smaller size, larger bandwidth, higher gain etc.) can be attained by loading bulk materials such as ferrites or by simply grading the material subject to specific design objectives. Multi-tone ceramic materials have also been used for miniaturization and pliable polymers offer new possibilities in three dimensional antenna design and multilayer printed structures, including 3D electronics. However, as the variety of examples in the literature shows, the perfect combination of materials is unique and extremely difficult to determine without optimization. In addition, existing artificial dielectrics are mostly based on intuitive studies, i.e. a formal design framework to predict the exact spatial combination of dielectrics, magnetics and conductors does not exist.

In the first part of this thesis, an inverse design framework integrating FE based analysis tool (COMSOL MULTIPHYSICS-PDE Coefficient Module) with an optimization technique (MATLAB-Genetic Algorithm and Direct Search toolbox) suitable for designing the microstructure of artificial magneto-dielectrics from isotropic material phases is proposed. Homogenizing Maxwell's Equations (MEQ) in order to estimate the effective material parameters of the desired composite made of periodic microstructures is the initial task of the framework. The FE analysis tool is used to evaluate intermediate fields at the 'micro-scale' level of a unit cell that is integrated with the homogenized MEQ's in order to estimate the 'macro-scale' effective constitutive parameters of the overall bulk periodic structure. Simulation of the periodic structure is an extremely challenging task due to the mesh at micro-level (inclusions much smaller than the periodic cell dimension) that spans over the entire bulk structure turning the computational problem into a very intensive one. Therefore, the proposed framework based on the solution of homogenized MEQ's via the micro-macro

approach, allows topology design capabilities of microstructures with desired properties. The goal is to achieve predefined material constitutive parameters via artificial electromagnetic substrates. Physical material bounds on the attainable properties are studied to avoid infeasible effective parameter requirements via available multi-constituents. The proposed framework is applied on examples such as microstructure layers of non-reciprocal magnetic photonic crystals. Results show that the homogenization technique along with topology optimization is able to design non-intuitive material compositions with desired electromagnetic properties.

In the second part of the thesis, approximation techniques to speed-up large scale topology optimization studies of devices with complex frequency responses are investigated. Miniaturization of microstrip antennas via topology optimization of both the conductor and material substrate via multi-tone ceramic shades is a typical example treated here. Long computational times required for both the electromagnetic analysis over a frequency range and the need for a heuristic based optimization tool to locate the global minima for complex devices present themselves as two important bottlenecks for practical design studies. In this thesis, two new techniques for speeding up the optimization process by reducing the number of frequency calls needed to accurately predict a multi-resonance type response of a candidate design are proposed. The proposed techniques employ adaptive sampling methods along with novel rational function interpolations. The first technique relies on a heuristic based rational interpolation using Bayes' theory and rational functions. Second, a rational function interpolation employing a new adaptive path based on Stoer-Bulirsch algorithm is used. Both techniques prove to efficiently predict resonances and significantly reduce the computational time by at least three folds.

MANYETİK-DİELEKTRİK MALZEME MİKROYAPILARININ TOPOLOJİ OPTİMİZASYON YÖNTEMİ KULLANILARAK TASARLANMASI

YASSER EL-KAHLOUT

ME, Doktora Tezi, 2009

Tez danışmanı: Yrd. Doç. Dr. Güllü Kızıltaş Şendur

Anahtar kelimeleri: Homojenlestirme teorisi, topoloji optimizasyonu, manyetik-dielektrik malzemeler, sonlu elemanlar analizi, malzeme tasarımı, yaklaşım teknikleri

Özet

Elekromanyetik *bant* yapılarına sahip *malzemeler* ve periyodik yapılar gibi yeni malzeme bileşenleri üstün elektormanyetik davranışları dolayısıyla son yıllarda oldukça ilgi çekmiştir. Sonuç olarak, yapay olarak değiştirilmiş malzemelerin teori ve uygulaması ile ilgili kapsamlı bir literatür bulunmaktadır. Fotonik kristalleri (normal, bozulmuş veya manyetik) de içeren örnekler belirli frekanslarda olağanüstü bir kazanç ve yüksek enerji transferi elde edilebileceğini göstermektedir. Malzemelerin yüklenmesi ('loading') konuları ile ilgili son araştırmalar göstermiştir ki anten performasında (daha küçük ebat, daha geniş bant genişliği, daha yüksek kazanç vb.) önemli ilerlemeler ferrit gibi malzemelerin yüklenmesi veya basitçe malzemenin belirli tasarım amaçlarına göre çoklu malzeme sistemlerinden oluşturulması ile sağlanabilmektedir. Minyatürleştirme için çoklu seramik malzemeler ve esnek polimerler üç boyutlu anten tasarımı ve eletroniği içeren çoklu katmanlı baskı devre yapılarında da yeni olasılıklar sunmaktadır. Buna rağmen, literatürdeki bir çok örneğin de gösterdiği gibi malzemelerin istenilen mükemmel bileşimi tek bir yapıya işaret eder ve optimizasyon yöntemlerine başvurulmadan bu birleşenlerin belirlenmesi çok zordur. Ek olarak, varolan yapay dielektrikler daha çok deneme yanılma çalışmalarına dayanmaktadır, yani dielektrik, manyetik ve iletkenlerin istenilen uzaysal birleşimini belirleyebilen formel bir tasarım süreci bulunmamaktadır.

Bu tezin ilk bölümünde, bu ihtiyaca cevap verebilmek için, sonlu eleman tabanlı analiz aracını (COMSOL MULTIPHYSICS-PDE Coefficient Module) yapay manyetik-dielektriklerin mikro yapısını izotropik malzeme fazları kullanarak tasarlanmasına uygun olan bir optimizasyon yöntemiyle (MATLAB-Genetic Algorithm and Direct Search toolbox) entegre ederek bir tersine tasarım yöntemi önerilmiştir. Periyodik mikro yapılardan oluşan etkin elektromanyetik malzeme parametrelerinin hesaplanabilmesi için Maxwell denklemlerinin homojenleştirilmesi bu sürecin ilk adımıdır. Sonlu eleman analiz aracı periyodik yapının makro-ölçekteki efektif/etkin konstitütif parametrelerinin tahmin edilebilmesi için homojen Maxwell denklemlerine entegre edilerek birim hücresinin mikro-ölçek seviyesindeki bir ara vektör alanının belirlenmesi için kullanılmıştır. Periyodik yapının similasyonu nümerik olarak büyük ölçekte bir yapıyı

kapsadığı için hesaplamayı yoğun bir probleme dönüştüren mikro seviyedeki (ihtivaları periyodik hücre boyutlarından çok daha küçüktür) ağ yüzünden çok zorlu bir iştir. Bu nedenle önerilen tasarım süreci, mikro yapıların istenen malzeme özelliklerine göre topoloji tasarım yöntemi kullanılarak mikro-makro yaklaşımıyla elde edilen homojen Maxwell denklemlerinin çözümüne dayandırılmıştır. Amaç yapay elektromanyetik malzeme katmanlarının önceden tanımlanmış konstitütif malzme parametrelerini elde etmektir. Mevcut çoklu-bileşenler kullanılarak gerçekleştirilemeyecek efektif parametre tasarımlarını önlemek amacıyla erişilebilir özelliklerdeki fiziksel malzeme sınırları teorik olarak çalışılmıştır. Önerilen tasarım süreci 'non-reciprocal' manyetik fotonik kristallerin mikro yapı katmanları gibi örneklere uygulanmıştır. Elde edilen sonuçlara göre homojenleştirme teknikleri topoloji optimizasyonu ile birlikte istenen elektromanyetik özelliklerde karmaşık malzeme bileşimlerini tasarlamaya uygundur.

Tezin ikinci bölümünde, karmaşık frekans davranışına sahip çok bilinmeyenli topoloji optimizasyon çalışmalarını hızlandırmak için yaklaşım teknikleri üzerinde durulmuştur. Mikroşerit antenlerin hem iletken hem de dielektirk katmanların çoklu seramik malzeme birleşenlerinin topoloji optimizasyonuyla minyatürleştirilmesi burada konu edilen tipik bir örnektir. Frekansa dayalı elektromanyetik analizler ve karmaşık RF cihazların evrensel optimizasyon çalışmalarında uzun hesaplama zamanları tasarım süreçlerinin pratik olarak yapılamamasında iki önemli unsur olarak ortaya çıkmaktadır. Bu tezde, bir tasarım örneğinin çoklu-rezonans tipi davranışını yaklaşık şekilde ifade ederek gerekli frekans bazlı analiz çağrılarını azaltarak optimizasyon işlemini hızlandıran iki adet yeni teknik önerilmiştir. Önerilen teknikler adaptif örnekleme metodlarına dayalı yeni rasyonel fonksiyon interpolasyonlarını kullanmaktadır. İlk teknik Bayes teorisi ve rasyonel fonksiyonları kullanan buluşsal tabanlı rasyonel interpolasyona dayanmaktadır. İkinci teknikte ise, Stoer-Bulirsch algoritmasına dayalı yeni bir adaptif yol izlenerek rasyonel fonksiyon interpolasyonu kullanılmıştır. Her iki teknik ile de rezonansların etkin bir şekilde tahmin edilebildiği kanıtlanmış ve toplam hesaplama zamanını üçte bire düşürerek tasarım problemlerinde önemli şekilde avantaj sağlandığı gösterilmiştir.

Table of Contents

List of Figures

List of Tables

1 INTRODUCTION

1.1 Motivation

Increasing demand for wideband devices and stringent metrics for multi-functionality within the telecommunications and microwave industry led to significant developments in novel components and sub-systems required for re-configurable, multifunctional, and dynamic devices. Metamaterials (MTM) or engineered materials with unusual properties, possess technological potential that breaks the limitation of current technology and satisfy stringent needs by the potential for developing such novel components and subsystems. MTM's intrinsic unusual properties and their capability to guide and efficiently control electromagnetic waves make them an immense technological breakthrough.

Interest in metamaterials has increased substantially since their discovery in the late 1980's. The immense potential of these structures in applications like communication and sensing systems is primarily due to their capability of controlling amplitudes, group and phase velocities, frequencies, wave-numbers, etc. of propagating and non-propagating electromagnetic modes to an extent that was not previously achievable.

Some aspects in novel applications demonstrate MTM's potential mainly regarding their capability to control electromagnetic modes. Strong controllability of dispersion in waveguides is an extremely attractive MTM characteristic to realize compact and therefore cost efficient phase shifters and delay lines for various applications including communication systems [1]. In addition, MTMs can reduce the size and enhance the communication performance of integrated planar filter components, especially where loss and bandwidth issues of these components is critical [2]. Substrate designs for microstrip based patch antennas and filters [3, 4] and electromagnetic bandgap (EBG) structures [5] are such examples. Also, MTMs are used in frequency selective surfaces (FSS), e.g. for radomes, stealth planes, cellular phones. EBG, FSS, and other MTMs gives the opportunity to mold the radiation characteristics of antennas [6, 7]. Using MTMs, imaging applications became possible proving wide

benefits for sub-diffraction imaging applications [8, 9]. In addition, metamaterials enabled flexibility in controlling electromagnetic wave propagation that present us with the opportunity to optimize the radiation characteristics of light emitting diodes to couple light generated in high refractive index materials into air effectively. Similarly, metamaterial research efforts are made on lasers, where metamaterials (i.e. photonic crystal slab lasers with defect modes) are employed to lower the threshold of lasers [10]. This is not only important in terms of efficiency and modulation bandwidth enhancement, but also will be crucial to realize deterministic single photon sources for quantum computing/communication technologies. Besides, metamaterials, especially plasmonics, are widely used in leaky wave antennas [6, 7, 11] where recent research encourages the transmission of evanescent modes through sub-wavelength structures used in near-field imaging/sensing applications. Development of high-Q resonant structures are desired for efficient filters or for sensing applications; has therefore drawn large interest in the optical data storage community, in order to provide sub-wavelength writing and reading capabilities for future data storage technologies to enhance the capacity beyond 1 TB/in^2 [12, 13]. Another potential application is the capability of Left Handed Materials (LHM) to be used for super-resolution imaging lenses [8, 14]. Incorporating tunable materials into metamaterials or having materials with active and controllable inclusions leads to tunable properties, regardless of the origin of the modulation. Under proper metamaterial configurations, small variations of the constituents may lead to extreme changes of metamaterial characteristics. Consequently, tunable components can be realized effectively in metamaterials [6, 15-18]. Practical applications include highly flexible and nimble cellular phones and low-cost steerable antennas.

As a result, the engineering of artificial materials in order to obtain attractive electromagnetic response has been an immense field of investigation over the past decades. To a broader extent, the intuitive or simulation based design of materials with engineered permeability and permittivity, through carefully designed inclusions and the possible use of electronic components have been expanding through the decade [19-23].

It is fair to say that these periodic structures are usually designed by theoretical consideration [24] based on equivalent circuit theory. Intuition of the expert designers at present is necessary for developing such efficient devices as theory alone provides only basic designs. Nevertheless, this approach encounters difficulties such as the challenge to tune parameters and includes a lot of guesswork and more importantly is very time

consuming. The need for a systematic design methodology for developing advanced microstructural devices became very important. Topology optimization is widely used as a systematic design method since it is the most versatile design method that can deal with geometrical and topological configuration changes at the same time. Hence, in this thesis the main objective is to develop a framework for designing the microstructure of materials with desired effective electromagnetic materials using topology optimization. This is the first formal step in the literature towards designing the microstructure of magneto-dielectric materials via topology optimization and should open new avenues for material design within the electromagnetic community.

1.2 **Metamaterials Modeling**

Modeling is a key factor that affects the accuracy and speed of the design process and is basically the backbone of simulation based design. Numerical modeling of metamaterials provided a temporary answer for simulation based verification for all the promising results proposed experimentally and bridged the gap between inhomogeneous metamaterials described by their discrete elements and the effective media. The need to improve simulation based modeling capabilities was motivated after a thorough numerical investigation of metamaterials' key properties such as transmission, backward phase, negative refraction, and focusing [25]. Efficient algorithms allowed for simulations of large models in 2D or 3D. Numerical simulation has been used rather than the experiment and has proven naturally to be a reliable and efficient way of studying metamaterials.

There are two main metamaterial modeling approaches that stand out in the literature. The first approach is a full wave simulation that solves the electromagnetic wave propagation represented by Maxwell's equations subject to boundary conditions as presented in [26-29]. The second one is an effective simulation based approach that solves the homogenized form of the Maxwell's equations and retrieves the effective parameters [30-35]. Although the full wave simulation approach is quite stable and a lot of studies on accuracy and speed-up measures prove the reliability and efficiency to a satisfactory level, it may not be the best choice to simulate periodic structures as long as the effective bulky parameters or characteristics of the structure are of main concern. This is because meshing at the micro-level (unit cell level) turns the computational

problem into an intensive one. Alternatively, effective simulation based approach focuses on the unit cell alone at the simulation level and predicts the macro-level effective parameters. The effective modeling approach can be classified into three main categories: An equivalent circuit approach as highlighted in [36, 37] where the unit cell constituents are modeled by simple circuit elements; Effective medium theories/mixture formulas which are mainly empirical formulas derived for certain type and shaped inclusions inside a host medium such as Clausius-Mosotti, Maxwell-Garnett, Lorenz-Lorentz relation [38] and Bruggeman [39]; and third is the homogenization based theory [31, 40-45]. Among them, mixing formulas and equivalent circuit approximations are not capable of handling arbitrary unit cell inclusion geometries and their applicability is constrained to only a few number of phase constituents whereas the theory of homogenization can handle any geometrical inclusions and it is unbounded in theory by the amount of unit cell constituents. The theory of homogenization is discussed next and presents the workhorse used as the material model within the design framework proposed in this thesis.

1.2.1 Homogenization theory

In this sub-section we explore key features of the homogenization technique applied within electromagnetic and major applications in literature.

Homogenization refers to replacing the inhomogeneous, periodic material in the microscopic scale with its homogeneous effective equivalent that has the same macroscopic effect as the original inhomogeneous structure. Computation of the homogenized material property of such repetitive composites allows replacing them with their equivalent, single homogenized, material. Hence, the process of homogenization drastically speeds up the numerical simulation process especially when the inhomogeneous unit cells, building blocks, of the composites are much smaller when compared with the size of the entire structure since otherwise very fine meshing during numerical simulations such as in Finite Element Method (FEM) would be required. Homogenization of corrugated interfaces in electromagnetics was studied in [46] where authors treated the corrugated surface as an inhomogeneous transition region (slab) yielding the homogenized surface with the effective reflection dyadic or the surface impedance dyadic. Their model in 1D has an explicit expansion whereas the 2D

model turns into an elliptic problem to be solved. The calculation of effective constitutive parameters at the interface of different media ranging from isotropic to bi-anisotropic was made possible in [47] by taking the boundary conditions of the field components into consideration that generalizes the previous approach. In 2002, the authors in. [48] introduced a method to retrieve the index of refraction ($n=n'+in''$) and the constitutive impedance ($z=z'+iz''$) or equivalently the effective constitutive parameters ($\varepsilon=n/z$ and $\mu=nz$) analytically via reflection and transmission coefficients (called scattering parameters, S-parameters) calculated from Transfer Matrix simulations on a finite length of electromagnetic metamaterials. Although this method is straightforward and gives an acceptable approximation, it does not exactly characterize metamaterials, and presents challenges in deciding upon the sign and branch of the solution (reference plane location in applying the boundary conditions) of the index of refraction and the impedance. Two years later, improvement on this method was made by assigning the reference plane as the first boundary and thickness of the effective slab and forcing n'' to be positive for correct selection of z' which must be positive, especially for cases where it is near zero that can lead to flip in sign [49]. Also, robust mathematical methods were proposed to choose the correct branch of the real part of n. Starr et al. characterized composite metamaterial panels fabricated using commercial multilayer circuit-board lithography, employing a similar direct method (analytical) based on S-parameter measurements leading to complete information on the material parameters [46]. The S-parameter retrieval procedures along with indirect methods, such as Snell's law measurements which can provide complementary information, can form the basis of a semi-automated metamaterial characterization. S-parameter numerical retrieval approaches for lossy bi-anisotropic media was introduced in [50]. In addition to S-parameters' retrieval direct analytical and numerical approaches used in predicting the electromagnetic constitutive parameters, recently [51] proposed an approach based on optimization to reconstruct the frequency-dispersive constitutive parameters of general bi-anisotropic media that produce reflection and transmission data matching the measured ones. Two optimization algorithms were used in this approach, differential evolution, DE, and Nelder-Mead simplex method to obtain the solution at different frequencies.

In addition to S-parameter based homogenization, equivalent circuit theory was often exploited. Equivalent circuit models were developed to calculate the effective constitutive EM parameters by modeling every split ring resonator column along the

axis of the rings as a quasi-solenoid under magnetic induction, hence allowing for calculation of the inductance per ring. The electromagnetic coupling between the split ring resonators equivalences, represented by quasi-solenoids, is integrated into circuit model where the frequency band of the negative permeability is predicted [52].

Effect of the periodicity of the structure on the effective medium model was studied in [53] in order to explain the origin or resonance/anti-resonance coupling and the negative imaginary parts of the constitutive parameters which cannot be explained by the resonance behavior of the EM parameters. This study demonstrates that in addition to the homogenization effective medium theory, periodic effective medium theory should be taken into consideration in composites where the lattice constant is greater than $\lambda/30$.

Existing studies related to retrieval of the constitutive parameters of metamaterials can be collected in two main groups: 1) Via S-parameters either analytically by inverting the reflection and refraction equations (dependent and independent variables), or numerically by optimization and 2) Via large scale equivalents that are either homogeneous (brought about their effective values in a process called inverse homogenization) or circuit models. New approaches are proposed to increase the accuracy through the addition of a corrector term compensating for a possible microscopic effect loss [31]. More importantly, the process of homogenization allows for the approximate modeling of complex shaped inclusions and highly dense composite materials where standard mixing formulas and other existing material models usually fail.

In 1994, Bossavit proposed to adopt homogenization to calculate the effective penetration depth in spatially periodic grids in [30]. This was based for the first time on homogenizing Maxwell's equations to obtain effective permittivity and permeability properties (and applied the results to the skin effect). The process relies on finding averaged parameters over a unit cell in the microscopic scale solving Maxwell's equation via FEM. This work explained the possibility of obtaining chiral or bi-anisotropic materials from simple isotropic constituents and developed computer electromagnetic analysis codes that take this method into consideration from the onset for analyzing chiral materials. Also, these homogenization methods were applicable to steady state cases and not to transient ones where frequency f dependency should be replaced with time t. Bossavit also applied homogenization theory to a 3D Bean's model for superconductivity where he solved for the electric field e and the surface current j

over a "periodicity cell" with periodic boundary conditions iteratively to pass from local Bean's model to an increasingly larger space scale [54]. Bossavit applied this theory to study realization of chiral material via mixing simple constituents [55, 56] as well. The homogenization theory clarifies the cross-dependency of the electric and magnetic flux densities **D** and **B**, on the electric and magnetic field intensities **E** and **H**, respectively, resulting in a chiral material behavior (which rotate the polarization plane of waves) and shows how geometrical chirality at cell level is needed. Improvements on this method were made [57] via asymptotic multi-scale methods and with the unfolding method which were utilized in calculating the effective conductivity for square cylinders and cubes suspended in a host isotropic medium. At high frequencies, however, homogenization becomes harder to implement and a link with standard harmonic analysis must be established [58].

The theory of homogenization itself was introduced with studies conducted in at least three directions. The first one was focusing on a general theory of convergence of operators (namely the H- and G- convergence). The first contributions to this field are found in [59-61] and further developments were made and demonstrated in [62]. The second direction is the asymptotic study of perforated domains consisting of media with many holes [63]. The third direction corresponds to the systematic study of periodic structures by means of asymptotic analysis. Pioneering work in this direction has been done in [45, 64-70]

Extensive efforts have been placed to develop algorithms based on the above three perspectives and researchers have come up with well established algorithms that are able to validate metamaterials' intrinsic properties. However, these have been mainly used to help the designer in adjusting mostly geometrical design parameters to improve desired electromagnetic performance. Quite a few studies have been established in this area and mainly focused on optimizing devices of already known volume and shapes (shape optimization). For example, in [4] numerical simulations and retrieval parameters were employed in a feedback loop to optimize and design dimensions of SRRs in order to improve gain and directivity of antennas and obtain new enhanced radiation patterns. Because of the fabrication constraints imposed on the building block or unit cells of metamaterials, especially for small elements used in high frequency applications where the dimension of the cell should be much smaller than the electromagnetic wave length λ, arbitrary shapes have not been investigated. It is explicitly noted by Yablanovitch [71], "The era of purely intuitive design may be

obsolete. We must now concentrate more on design software, rational design, and the numerical solution of inverse problems. Engineering design is formally a type of mathematical Inverse Problem. The design goal is a certain electromagnetic specification or desired electromagnetic performance. It is necessary to work backward from that goal to the exact design of the dielectric boundary that achieves the objective". In that respect, topology optimization methods present us with an ideal inverse design tool which has not been applied earlier to explore the full potential of artificial magneto-dielectrics for novel applications. The variety of examples show that the perfect combination of materials is unique and extremely difficult to determine without a systematic design procedure [3, 72, 73], which is addressed in this thesis with a material design framework for materials with desired electromagnetic matrix properties

In the next section we demonstrate one of the most flexible design optimization methods and its implementation to structural mechanics, where it emerged from and then within the electromagnetic community along with periodic structures.

1.3 **Topology Optimization**

Since the emergence of the finite element method (FEM) by Courant [74] and its systematic formulation setup in [75], it became the backbone of numerical optimization. The first integration of FEM with optimal structural design was made in [76] and later in [77, 78] then an intensive research was launched in the field of modern structural optimization including a variety of application in civil, mechanical and nuclear engineering. Structural optimization can be divided into three main sub-fields, i.e. size, shape, and topology optimization. The first structural topology optimization is found in 1904 when important principles were established for truss like structures [79]. These principles were extended to grillages in [80]. The basic principles of optimal structural design were formulated in [81-83]. Bendsoe and Kikuchi [84] were the first to introduce a practical FE-based topology optimization for non-truss structures. They introduced the homogenized based topology optimization method (HTBO) to find the optimum layout of a linearly elastic structure to achieve global stiffness. The HBTO method is based on the assumption of a composite material with a micro structure whose properties are

homogenized by a rigorous mathematical procedure. Typically, an algorithm based on the optimality criteria is used to update the size and orientation of voids.

So far, the most popular problem in topology optimization of linear elasticity is that of minimizing compliance. The design principles were also extended to non-linear constitutive models [85]. Although early efforts in structural topology optimization focused on global responses such as stiffness and frequency, later studies dealt with more specific engineering problems such as automotive design, welding for reinforcement, drilling holes for weight reduction. Also, structural topology optimization was extended to dynamical problems including vibration and noise reduction, maximizing safety, minimizing cost etc. In other words, the field of structural topology optimization has expanded significantly, addressing many practical engineering problems including maximum stiffness, maximum eigenvalues, optimum compliant mechanisms or piezoelectric actuators and extreme material properties. It has also been widely employed in industry, with several commercial software packages. Sigmund et al. [86] discussed the numerical instabilities in topology optimization related to checkerboarding, mesh dependence and local minima of topology optimization applications. Comprehensive reviews on the mechanical, structural and computational aspects have been given in the monographs [87-89] and the review articles [83, 84].

In electromagnetics, the concept of sensitivity for finite element analysis and its use in the optimization process for magnetic problems was first introduced in 1988 in [90]. Since then, design sensitivity analysis using the adjoint variable method has been applied almost routinely to the optimization of magnetic devices. Applications include linear [91], non-linear magnetic systems [92] and also linear electrostatic systems [93]. The optimization problems relying on the sensitivity information using the adjoint variable method (AVM) have been restricted to optimizing the shape of specific features of a complete device design. For instance, the pole shape of an electromagnet [94], slot shape in the rotor of an induction motor [95] or the shape of a defect in an aluminum block [91] are examples for such shape optimization problems. Topology optimization follows the exact same approach as in structural mechanics and was introduced to the EM community using Solid Isotropic Material with Penalization (SIMP). As an example, SIMP is applied to the design of a jumping ring, a typical simple magneto-static problem. Although the application was restricted to simple magneto-static problems, it provided an approach for automated topology design in EM. Dyck and

Lowther studied how to interpret the resulting intermediate material distribution by relating it to composites of available materials [96].

Byun et al. [91] who also applied the SIMP method for the topology optimization in EM, dealt with the design of a transformer coil. The problem was to solve an eddy current problem, a simplified case of more common realistic EM applications demanding more complex analysis procedures. Later, the same authors extended the design method to a specific class of inverse problems, where their goal was to find the shape and location of the dielectric material embedded in a material of different permittivity [93]. Consequently, the application area of topology optimization in EM was expanded from magneto-static or eddy current systems to 3D linear electrostatic problems. Also, topology optimization has been extended to wave propagation problems, such as radio-frequency and optical problems. A waveguide was successfully designd for an optic wave propagation problem by [97]. Topology optimization was applied to a design of waveguide components by [98]. Kiziltas et al. [3] developed an optimal design method for enhancing the bandwidth of microstrip patch antennas using the finite element boundary integral method with vector wave propagation analysis. Extension of the topology optimization to vector wave propagation with finite-difference time-domain method was made in [99].

In conclusion, literature reports only a few applications of topology optimization to electromagnetic problems but they are rarely applied to periodic structures and existing studies are strictly focusing on the optimal design targeting the performance of the device only instead of directly focusing on the design of the material itself.

In this thesis, we incorporate the topology optimization with the homogenization theory based on asymptotic expansion analysis in order to design prescribed effective electromagnetic constitutive parameters, i.e. permittivity and permeability tensors. These materials with desired electromagnetic properties can be a part of size, shape, or even topology optimization studies targeting novel electromagnetic device performance. Among others, a typical device performance example relates to the optimal design of antennas with increased bandwidth. Electromagnetic performance is usually measured by the S-parameter responses over a defined range of working frequencies. During the optimization process, optimal design candidates with updated design variables are analyzed using one of the rigorous analysis tool mentioned in Section 1.2. Such a response requires sweeping over a lot of discrete frequency points that makes the analysis tool and consequently the optimization process computationally very costly. As

part of this thesis, this computational challenge arising in large-scale design optimization studies, such as topology optimization, is addressed by developing two different approximation techniques. Therefore, in the next section we review such interpolation techniques and adaptive sampling procedures that reduce the number of frequency calls needed to predict an accurate S-parameter response for complex devices optimized in large scale design studies.

1.4 **Interpolation Techniques for Speeding up Optimization Process**

As discussed in Section 1.3, design optimization has been a difficult, demanding but necessary task for the development of novel commercial radio frequency applications such as miniaturization of antennas without sacrifice in their bandwidth and radiation efficiency. The need for design, preferably design optimization, is pertinent to the competing physics of these metrics, which has been the focus of researchers for the past two decades. It is reasonable to expect that designs resulting from global design optimization studies that allow for full design space exploration including antenna shape, size, feed location and material will lead to novel configurations with enhanced performance. However, global synthesis via heuristic search techniques relies on fast and accurate reanalysis, which presents itself as a bottleneck in large scale electromagnetic search studies. Therefore, unless design studies are limited to only a few number of design variables [100], simulation based electromagnetic design studies can become impractical. To address this issue, two different approximation schemes suitable for the frequency response of electromagnetic systems such as multi-resonance return loss of antennas is investigated. The goal is to develop efficient and reliable schemes that allow for fast and accurate reanalysis within global electromagnetic design optimization studies.

Surrogate modeling techniques [101] are approximation schemes typically used for efficient electromagnetic reanalysis. Most common surrogate modeling approaches rely on the use of polynomials, multiquadrics [102], kriging [103, 104] and artificial neural networks [105]. Surrogate models serve a common central purpose by providing a 'virtual' objective function which can be called by the optimization solver within a design cycle. Variations in the surrogate models are due to training and/or tuning parameters. However, training a model of increased topological complexity leads to an

excessive computational effort and most of the time results in a model that is problem dependent. Also, the resulting approximate objective function is only valid in a constrained sub-domain which is likely to contain the optimum and therefore the approximate surrogate model is only valid in this region.

Basis functions employed within the interpolation models have great influence on the quality of the surface approximation. Among alternatives, rational functions offer an attractive solution for providing approximate resonances due to their inherent pole predicting behavior. Therefore, they are likely to yield a more accurate approximation for a larger class of problems with a reduced computational effort. Hence, their use has resulted in various representations of resonance type responses with reasonable number of support points [106-112].

The first rational based approximation scheme proposed in this thesis employs an easy-to-train and simple decision making classifier based on Bayes' theorem to predict multi-resonance return loss curves of electromagnetic (EM) devices with complex topologies. Bayes' theorem has been extensively utilized for interpolation in signal processing problems [113-115]. For example in [113], Bayesian variational technique is used to successfully predict both the parameters of a linear-in-the parameter model and the form of the noise process to be used, namely Gaussian versus Student-t. This approach is implemented on synthetic data generated by the function $\mathrm{sinc}(x) = \sin(x)/x$ and results show that for a non-Gaussian noise distribution adaptive Student-t form outperforms the Gaussian especially when outliers exist. In [114], Bayesian technique with Gaussian apriori model is used to interpolate 3D x-ray crystallography data in the presence of icosahedral symmetry deteriorated by noise. Here, the Bayesian classifier is also used to determine the basis function used in the interpolators in terms of the statistical assumptions. Fearnhead [115] exhibits a novel algorithm for performing exact Bayesian inference for independent linear regression models on disjoint segments. This approach avoids the problem of diagnosing convergence associated with Markov Chain Monte Carlo method. The algorithm is successfully demonstrated on standard denoising problems, a piecewise constant auto-regression model, and a speech segmentation problem. Unlike many of Bayes interpolation uses in the literature, in this thesis, the proposed method employs the Bayesian classifier in order to infer a controlling parameter that controls the shape of the resulting resonances associated with a rational interpolator of quadratic numerator and denominator. The remaining rational function

parameters are determined by given boundary conditions of the interval of interest which are calculated using a finite element based analysis tool [28].

Selection of sample points adaptively is known to affect the interpolation quality. Nevertheless, most adaptive sampling schemes available are suitable for global curve fittings that, unlike the proposed piecewise rational function, interpolate the whole range with one interpolator [108, 116-118]. The proposed interpolation scheme here again employs the Bayesian classifier in order to adaptively sample the frequency range by bisecting and hence refining the interval under consideration that enhances the interpolation process. The Bayesian trained rational function proves to have a powerful yet, unlike other standard approaches such as Neural Networks, simple approximation capability based on statistics and just a single controlling parameter. Further enhancements in terms of speed are naturally expected if an effective gradient estimator such as the adjoint variable method is used allowing the calculation of sample derivative values at no extra computational cost [90]. In Chapter 4, an in-depth analysis of the proposed interpolation's efficiency and reliability is shown by an example of an individual of a generation in a genetic algorithm applied for designing concurrent dielectric and conductor topologies for miniaturized novel antennas [119].

The aforementioned surrogate models serve a common central purpose: They provide a 'virtual' objective function which can be called by the optimization solver within a design cycle. Variations exist in the training and/or tuning parameters when creating these surrogate models. Unfortunately, training a model of increased topological complexity leads to an excessive computational effort and most of the time results in a model that is problem dependent. Also, the resulting approximate objective function is only valid in a constrained design sub-domain which is likely to contain the possible optimum and therefore the original model can be replaced with an approximate surrogate model only in this region. For problems where the optimization model relies on the calculation of a frequency based electromagnetic response (such as bandwidth or input impedance) of topologically complex devices, the creation of a reliable surrogate model becomes questionable. This is the case particularly as the dimensionality of the design space increases such as in large-scale volumetric synthesis problems.

However, rational functions offer an attractive solution for providing a more global approximation taking into account the entire band of the frequency response into consideration. They also provide additional advantages. First, they are well suited for approximating resonances due to their inherent pole predicting behavior. Also, unlike

surrogate models they do not rely on tuning parameters. Therefore, rational functions are likely to yield a more general approximation valid for a larger class of problems with a reduced computational effort and are more suitable to approximate frequency dependent electromagnetic responses. As a result, their use has resulted in various representations of resonance type curves with reasonable number of support points [106-112]. Solving for the coefficients of the rational function is known as the Cauchy method and is first introduced in [120].

Cauchy method has been employed for the extraction of a circuital model [121], the response of which fits the microwave device reflection and transfer functions of non-lossy systems. Lamperez et al. [122] extended the Cauchy method in [121] to reduce the model order of systems which may be lossy. In addition to the complicated mathematics needed for deducing the resulting expression or equivalent circuits, this technique is restricted to electromagnetic optimization of devices such as filters and multiplexers. Moreover, the solution within a standard Cauchy based method with techniques such as direct inversion becomes more prone to numerical errors as the number of support points increases (by producing a system of linear equations which is ill-conditioned).

A solution alternative to ill-conditioned systems is presented in [112], where Sarkar et al. made use of the Cauchy method by fitting a rational function to samples produced by the method of moment of the far field frequency response of a slit conducting cylinder and/or their derivatives. This technique has the potential of accurately predicting wide-band response utilizing narrow-band information via both interpolation and extrapolation. The computations have been automated later in [111] addressing the issue of adequacy of Cauchy method to certain data at hand. In both of these studies, the order of the optimum rational function is chosen such that the number of unknown coefficients is less than or equal to the rank of the corresponding stiffness matrix and hence the system to be solved becomes over-determined. Stiffness matrices are constructed via singular value decomposition and the total least squares method is employed to solve for the unknown coefficients. These studies show that singular values of the stiffness matrix determine the suitability of the rational interpolation. The proposed methodology allows for incorporating support point and derivative information. However, a frequency response with multi-resonances cannot be approximated via the rank constrained strategy as the rank of the system limits the order of the rational model. Also, since for each newly added point the system is re-solved, it

becomes computationally expensive when integrated with adaptive sampling techniques. An alternative approach to overcome these issues suitable for the solution of the unknown coefficients of a rational interpolation function is a support point recursive technique initially introduced by Stoer and Bulirsch [123] where the Neville approach is applied to rational functions.

Stoer-Bulirsch technique is a recursive method that adds one support point at a time and solves for the unique rational interpolator that passes through all existing support points. This recursive strategy in turn enhances its suitability to adaptive sampling techniques. In adaptive sampling, each new support point is determined based on a certain error norm and its interpolator is found using the available data set. When compared with direct inversion solutions of rational interpolations, Stoer-Bulirsch technique is significantly less prone to numerical errors and is not constrained by the rank of the system.

It is well known that the data set used for interpolation determines the quality of the resulting fitted curve. Therefore, adaptive sampling of a frequency response constitutes a key aspect in interpolation, hence, careful selection of these informative support points to serve as input data to the interpolation technique should result in a more successful interpolation [109, 116, 117]. Frequency data sets have been adaptively constructed and integrated to the proper choice of the rational function within Stoer-Bulirsch technique to establish a fast interpolation scheme. Specifically, in [109] two adaptive sampling algorithms for rational interpolation are proposed. This technique relies on discretizing the frequency range into uniformly distributed intervals among which the appropriate frequency points will be selected from. As the algorithm progresses, uniformly distributed intervals are being refined if necessary. This uniform interval adaptive method alleviates drawbacks such as excessive sampling and outperforms other standard techniques such as the one used by Lehmensiek and Meyer [117]. Yan et al. [124] proposed adaptive sampling through rational functions created by following alternative Neville paths based on diagonal paths representing *increments* of the numerator and denominator by one after a specific switching grid is chosen so that that part of the resulting path is parallel to the main diagonal one.

One dimensional adaptive sampling within standard Stoer-Bulirsch technique has been upgraded to multi-dimensional fitting in [116]. Specific disadvantages still remain: The adaptive sampling parameters are not problem independent and need to be retuned for each new response, and the Stoer-Bulirsch interpolations are constructed based on a

pre-determined standard diagonal path which is not optimized, hence resulting interpolations even if adaptively constructed can be further improved for accuracy and computational efficiency. In this thesis, we propose as a second approximation technique, an adaptive sampling technique that works on a set of candidate support points which are generated only if necessary according to a chosen quality error norm unlike selecting it from a fixed predefined set of uniform data as proposed in [109]. The proposed technique is based on a generalized Neville algorithm which allows for an off-diagonal path as suggested in [125] in opposition to the conventional diagonal paths in standard Stoer-Bulirsch technique. However, since both the path followed to construct the interpolator and the samples selected directly affect the quality and computational cost of the interpolation process, an optimized route is expected to result in more reliable and cost effective interpolations. To address this issue, the idea of a generalized Neville path is integrated here to an adaptive sampling strategy. Also, to further enhance the performance of an adaptive Neville path, the resulting algorithm is optimized for numerical stability and integrated to an initial diverse sampling. The resulting generalized Stoer-Bulirsch algorithm is analyzed and compared with standard Stoer-Bulirsch technique and interpolation schemes with proposed enhancement features. Results demonstrate the capability of the optimized method to overcome three common problems of existing methods: premature convergence, catching significant resonances and avoiding spurious oscillations. As a result, the proposed generalized Stoer-Bulirsch algorithm leads to approximations with reduced number of samples and enhanced accuracy norms.

1.5 Objective and Contributions of the Thesis

In this thesis, a formal design scheme relying on integrating an accurate modeling/analysis tool that simulates the performance of heterogeneous material structures with spatial distribution of magneto-dielectric constituents with a versatile optimization method is proposed. The material model employed in the proposed design framework is based on the mathematical theory of homogenization using asymptotic expansion and is capable of calculating the effective constitutive parameters of a composite magneto-dielectric material. Consequently, the resulting framework allows for the design of material topologies with arbitrary inclusion geometries and multi-

phases. This composite substrate is described by spatially periodic parameters and its effective constitutive parameter is calculated using the PDE-Coefficient Form module of the commercial FEA solver COMSOL. The material simulation model is linked with a global genetic algorithm tool to design the unit cell topology of the periodic structure. The goal is to design materials microstructures with desired constitutive parameters employing off-the-shelf isotropic constituents.

A second objective is related to addressing a well-known computational bottleneck existing in large-scale optimization studies of complex electromagnetic devices with multi-resonance type frequency response. The goal here is to develop rational function interpolations integrated with adaptive sampling schemes capable of predicting multi-resonant type responses accurately and with a few number of frequency sampling points. This is expected to reduce the computational cost needed for re-analysis in predicting the S-parameter response and consequently speed up the optimization process of novel electromagnetic devices.

Contributions of this thesis can be summarized as follows:

1) Develop a formal inverse design methodology for the microstructure of magneto-dielectrics with desired effective constitutive parameters by
   a) Extending topology optimization to design the unit cell of the structure
   b) Implementing the asymptotic expansion based homogenization theory applied on Maxwell's equations in order to calculate the effective constitutive parameters

2) Develop an efficient interpolation technique for accurately predicting multi-resonant type frequency scattering parameter responses of electromagnetic devices with minimum number of sampling frequency points by
   a) Heuristic based technique (implementing Bayes' theory) that infers resonances inside the interval of interest and adaptively samples frequency points.
   b) Extending Stoer-Bulirsch algorithm to follow a non-diagonal path incrementation of the rational function order and exploiting this scheme to increase the interpolation accuracy and reduce the number of sampling frequencies.

Application areas of the thesis are

1) Magneto-dielectric slabs with desired constitutive anisotropic parameters (permittivity/permeability tensors)

2) Layers of non-reciprocal magnetic photonic crystals

3) Large scale topology optimization of microstrip patch antennas

1.6 **Outline of the Thesis**

The thesis is organized as follows: Chapter 2 comprises background on homogenization theory using asymptotic expansion applied to Maxwell's equations, implementation of the design framework with validation examples, and a study on bounds of effective parameters. Chapter 3 is devoted to the design of dielectric layers for non-reciprocal magnetic photonic crystals using the developed formal design methodology. Chapter 4 and Chapter 5 describe rational function interpolation schemes via Bayes' theory and Stoer-Bulirsh algorithm's non-diagonal path, respectively. Remarks and future work ideas are mentioned in Chapter 6.

2 HOMOGENIZATION THEORY APPLIED TO ELECTROMAGNETICS

2.1 Homogenization of Maxwell's Equations

The theory of homogenization by the asymptotic method is well established in literature [45]. The homogenized constitutive parameters represented by the permittivity and permeability tensors of Maxwell's equations are derived in this chapter and will be used in this thesis as a part of developing a formal design framework with the goal of obtaining the homogenized/effective material tensors ε_{eff} and μ_{eff}. The governing equations are manipulated as discussed next.
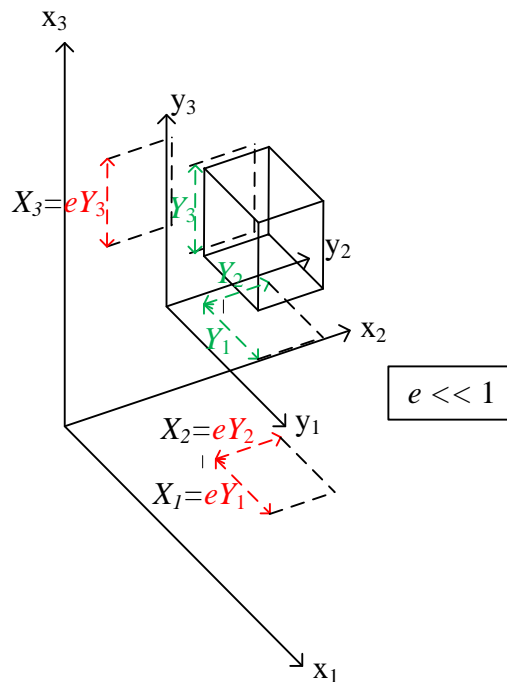
Figure 2.1 Three dimensional unit cell represented in the microscale $\mathbf{y} = \begin{bmatrix} Y_1 & Y_2 & Y_3 \end{bmatrix}^T$ and the macroscale $\mathbf{x} = \begin{bmatrix} X_1 & X_2 & X_3 \end{bmatrix}^T$ coordinate systems where e is the lattice constant

If we assign a coordinate system $\mathbf{x} = \begin{bmatrix} X_1 & X_2 & X_3 \end{bmatrix}^T$ in $\mathbf{R}^3$ space to define the domain of the composite material $\boldsymbol{\sigma}$, then assuming periodicity, the domain can be regarded as a collection of parallelepiped cells of identical dimensions eY_1, eY_2, and eY_3 where Y_1, Y_2, and Y_3 are the sides of the base cell in a local (microscopic) coordinate system $\mathbf{y} = \begin{bmatrix} Y_1 & Y_2 & Y_3 \end{bmatrix}^T = \mathbf{x}/e$ and e is a small quantity representing the lattice constant or the unit cell dimension, Figure 2.1. Therefore, any dependency on $\mathbf{y}$ can be considered $\mathbf{y}$-periodic for a fixed $\mathbf{x}$ in the macroscopic level. Moreover, it is assumed that the form and composition of the base cell varies in a smooth way with the macroscopic variable $\mathbf{x}$. We consider two matrices

$$\mathbf{a}^e(\mathbf{x}) = \left[\mathbf{a}_{ij}^e(\mathbf{x}) \right] \text{and } \mathbf{a}_{ij}^e(\mathbf{x}) = \mathbf{a}_{ij}\left(\frac{\mathbf{x}}{e} \right) \tag{2.1}$$

$$\mathbf{a}_0^{\ e}(\mathbf{x}) = \left[\mathbf{a}_{0ij}^{\ e}(\mathbf{x}) \right] \text{and } \mathbf{a}_{0ij}^{\ e}(\mathbf{x}) = \mathbf{a}_{0ij}\left(\frac{\mathbf{x}}{e} \right) \tag{2.2}$$

where both functions $\mathbf{a}_{ij}(\mathbf{y})$ and $\mathbf{a}_{0ij}(\mathbf{y})$ are $\mathbf{y}$-periodic. We consider the boundary value problem associated with the equation

$$rot\left(\mathbf{a}^e \, rot(\mathbf{u}_e) \right) + \mathbf{a}_0^e \mathbf{u}_e = \mathbf{f} \text{ in } \boldsymbol{\sigma} \tag{2.3}$$

where $\mathbf{a}^e$ and $\mathbf{a}_0^e$ are 3×3 matrices representing the constitutive parameters that can vary with respect to space and frequency, rot is the curl operator and $\mathbf{f}$ is a vector representing the source term, and $\boldsymbol{\sigma}$ is the unit cell domain.

We will study the behavior of the vector variable $\mathbf{u}_e$ as e approaches zero. Let the operator working on the field quantity $\mathbf{u}_e$ called $\mathbf{A}^e$ be defined as follows

$$\mathbf{A}^e = rot\left(\mathbf{a}^e \, rot \right) + \mathbf{a}_0^e \tag{2.4}$$

Without loss of generality we will let $\mathbf{a}_0^e = \lambda \mathbf{I}$, where $\mathbf{I}$ is the identity matrix, in which case the expression is incapable of representing full anisotropic properties but this

condition will be relaxed later. Using the chain rule of differentiation

$$rot_x \, \mathrm{f}(x, y) = rot_x \, \mathrm{f} + rot_y \, \mathrm{f} \frac{\partial y}{\partial x} = rot_x \, \mathrm{f} + rot_y \, \mathrm{f} \, e^{-1},$$ the operator $\mathbf{A}^e$ can be rewritten as

$$\mathbf{A}^e = e^{-2}\mathbf{A}_1 + e^{-1}\mathbf{A}_2 + e^0\mathbf{A}_3 + \mathbf{a}_0^e \tag{2.5}$$

where the operators on the right hand side are given by

$$\begin{aligned}
\mathbf{A}_1 &= rot_y \mathbf{a}^e rot_y \\
\mathbf{A}_2 &= rot_y \mathbf{a}^e rot_x + rot_x \mathbf{a}^e rot_y \\
\mathbf{A}_3 &= rot_x \mathbf{a}^e rot_x
\end{aligned} \tag{2.6}$$

The field vector $\mathbf{u}$ is expanded asymptotically as,

$$\mathbf{u} = \mathbf{u}_0(\mathbf{x}, \mathbf{y}) + e^1\mathbf{u}_1(\mathbf{x}, \mathbf{y}) + e^2\mathbf{u}_2(\mathbf{x}, \mathbf{y}) + \cdots \tag{2.7}$$

Substituting the last equation along with the expanded operator given by (2.5) and (2.6) into the boundary value problem (2.3) and manipulating proves that $\mathbf{u}_0$ is a function of $\mathbf{x}$ alone and for simplicity is denoted by $\mathbf{u}$

$$\mathbf{u}_0 = \mathbf{u}_0(\mathbf{x}) = \mathbf{u} \tag{2.8}$$

and the following relation is obtained

$$rot_y \mathbf{a}^e \left(rot_y \mathbf{u}_1 + rot_x \mathbf{u}\right) = \mathbf{0} \tag{2.9}$$

Now, let us define a vector quantity $\mathbf{w}$ as

$$\mathbf{w} = \mathbf{a}^e \left(rot_y \mathbf{u}_1 + rot_x \mathbf{u}\right) \tag{2.10}$$

Averaging $\mathbf{w}$ over the problem domain $\boldsymbol{\sigma}$, it becomes a function of $\mathbf{x}$ alone because of the $\mathbf{y}$-periodicity over the domain and can be written with the aid of the averaging operator $\mathcal{M}$ or equivalently $\tilde{\mathbf{w}}$ as

$$\mathcal{M}(\mathbf{w}) = \tilde{\mathbf{w}} = \tilde{\mathbf{w}}(\mathbf{x}) \tag{2.11}$$

Using (2.9), (2.10), (2.11) and noting that the rotation with respect to y for a function of x alone is zero, $rot_y \tilde{\mathbf{w}}(\mathbf{x}) = \mathbf{0}$ we can write

$$rot_y(\mathbf{w} - \tilde{\mathbf{w}}) = \mathbf{0} \tag{2.12}$$

Equation (2.11) can be rearranged as

$$\mathcal{M}(\mathbf{w} - \tilde{\mathbf{w}}) = \mathbf{0} \tag{2.13}$$

From equation (2.12), it can be deduced that there exists a scalar function $\Psi(\mathbf{x}, \mathbf{y})$ the gradient of which is equal to the quantity $\mathbf{w} - \tilde{\mathbf{w}}$.

$$\mathbf{w} - \tilde{\mathbf{w}} = -grad_y \Psi(\mathbf{x}, \mathbf{y}) \tag{2.14}$$

Using (2.10) and recalling the identity $div_y(rot_y \mathbf{v}) = 0$ for any vector quantity $\mathbf{v}$, the following relation can be obtained

$$div_y\left((\mathbf{a}^e)^{-1}\mathbf{w}\right) = div_y(rot_y \mathbf{u}_1 + rot_x \mathbf{u}) = 0 \tag{2.15}$$

Substituting (2.14) into (2.15) yields:

$$-div_y\left((\mathbf{a}^e)^{-1} grad_y \Psi\right) = -div_y\left((\mathbf{a}^e)^{-1}\tilde{\mathbf{w}}\right) \tag{2.16}$$

The solution of the last equation is crucial for calculating the effective parameters as will be shown later. The solution is simplified by introducing a field quantity parameter $\boldsymbol{\theta}$ according the following relation.

$$\Psi = \mathbf{0} \cdot \tilde{\mathbf{w}} \tag{2.17}$$

Equation (2.16) can be rewritten using the last relation as

$$-div_y\left(\left(\mathbf{a}^e\right)^{-1} grad_y \theta^j\right) = -div_y\left(\left(\mathbf{a}^e\right)^{-1}\mathbf{e}_j\right) \tag{2.18}$$

where $\mathbf{e}_j$ is an identity vector in the corresponding axis. Equation (2.18) is solved for each problem space dimension, i.e. for a three-dimensional problem, $j = 1,2,3$.

Using (2.14) and (2.17) and noting that $\mathbf{w}$ can be written as

$$\mathbf{w} = \left(\mathbf{I} - grad_y \mathbf{\theta}\right)\tilde{\mathbf{w}} \tag{2.19}$$

where $grad_y \mathbf{\theta}$ for a three-dimensional problem is defined as the following

$$grad_y \mathbf{\theta} = \begin{bmatrix} \theta^1_{,y_1} & \theta^2_{,y_1} & \theta^3_{,y_1} \\ \theta^1_{,y_2} & \theta^2_{,y_2} & \theta^3_{,y_2} \\ \theta^1_{,y_3} & \theta^2_{,y_3} & \theta^3_{,y_3} \end{bmatrix} \tag{2.20}$$

Averaging $\left(\mathbf{a}^e\right)^{-1}\mathbf{w}$ in (2.10) yields

$$\mathcal{M}\left(\left(\mathbf{a}^e\right)^{-1}\mathbf{w}\right) = rot\mathbf{u} \tag{2.21}$$

Substituting (2.19) into the last equation gives:

$$\mathcal{M}\left(\left(\mathbf{a}^e\right)^{-1}\left(\mathbf{I} - grad_y \mathbf{\theta}\right)\right)\tilde{\mathbf{w}} = rot\mathbf{u} \tag{2.22}$$

We will define a new operator which will account for homogenization, $\mathcal{H}$, working on $\left(\mathbf{a}^e\right)^{-1}$ as follows

$$\mathcal{H}\left(\left(\mathbf{a}^e\right)^{-1}\right) = \mathcal{M}\left(\left(\mathbf{a}^e\right)^{-1}\left(\mathbf{I} - grad_y \mathbf{\theta}\right)\right) \tag{2.23}$$

And hence $\tilde{\mathbf{w}}$ in (2.22) can be written in terms of the $\mathcal{H}$ operator as

$$\tilde{\mathbf{w}} = \mathcal{H}\left(\left(\mathbf{a}^e\right)^{-1}\right)^{-1} rot\mathbf{u} \tag{2.24}$$

When the last equation is compared with (2.10), we conclude that the operator $\mathcal{H}$ is the homogenization operator that yields the effective property as $\tilde{\mathbf{w}}$ and $rot\mathbf{u}$ in (2.24) are the average quantities of $\mathbf{w}$ and $\left(rot_y\mathbf{u}_1 + rot_x\mathbf{u}\right)$, respectively, in (2.10). Applying (2.22) on the operator $\mathbf{A}^e$ given by (2.4) we get the homogenized operator as follows:

$$\mathcal{H}\left(\mathbf{A}^e\right) = rot\left(\mathcal{H}\left(\left(\mathbf{a}^e\right)^{-1}\right)^{-1} rot\right) + \lambda \tag{2.25}$$

According to Theorem 11.4 in [45], if the operator $\mathbf{a}_0^e$ is anisotropic which is a general case, the homogenized operator can be written as

$$\mathcal{H}\left(\mathbf{A}^e\right) = rot\left(\mathcal{H}\left(\left(\mathbf{a}^e\right)^{-1}\right)^{-1} rot\right) + \mathcal{H}\left(\mathbf{a}_0^e\right) \tag{2.26}$$

The wave equation is represented by

$$rot\left(\boldsymbol{\mu}^{-1}rot(\mathbf{E})\right) - \omega^2\boldsymbol{\varepsilon}\mathbf{E} = -j\omega\mathbf{J}_i \text{ in } \boldsymbol{\sigma} \tag{2.27}$$

where $\mathbf{E}$ and $\mathbf{J}_i$ are the electric field and the induced current, i.e. $\mathbf{u}$ and $\mathbf{f}$, respectively. In the above derivations when $\left(\mathbf{a}^e\right)^{-1}$ and $\mathbf{a}_0^e$ are replaced by the permeability and permittivity tensors $\boldsymbol{\mu}$ and $\boldsymbol{\varepsilon}$, respectively, the homogenized permittivity and permeability tensors can be finally defined as in equations (2.27) and (2.28) below.

$$\mathcal{H}(\boldsymbol{\mu}) = \mathcal{M}\left(\boldsymbol{\mu}\left(\mathbf{I} - grad_y\boldsymbol{\theta}\right)\right) \tag{2.28}$$

$$\mathcal{H}(\boldsymbol{\varepsilon}) = \mathcal{M}(\boldsymbol{\varepsilon}(\mathbf{I} - grad_y\boldsymbol{\theta})) \qquad (2.29)$$

2.2 Numerical Implementation of the Homogenized Material Model

In this section we make use of the homogenized form of the permeability and the permittivity dyads given by (2.28) and (2.29) and numerically implement them in order to calculate the effective properties at the macro-scale level. The operator $\mathcal{M}$ is a straightforward operator since it is simply a volumetric averaging operator. Nevertheless, the intermediate field $\boldsymbol{\theta}$ requires careful consideration because it requires the solution of a partial differential equation given by (2.18). Towards that goal, we employ a finite element based solution environment using COMSOL MULTIPHYSICS and utilize the Coefficient Form module. The objective is to solve this boundary value problem that is periodic in $\boldsymbol{\theta}$ on the boundaries of the unit cell.

Figure 2.2 shows a unit cell that is discretized into 9 x 9 discrete sub-cells filled with material phases of different properties.
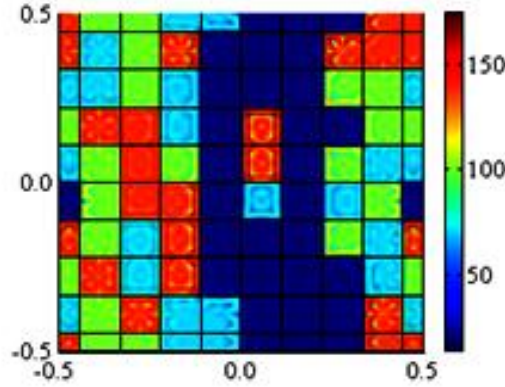
Figure 2.2 A typical two-dimensional periodic unit cell composed of four constituents with different permittivities $\varepsilon \in \{20, 70, 100, 140\}$ distributed discretely in a 9 x 9 cell configuration.

The most general form of the Coefficient Form module PDE in COMSOL is as:

$$div(-\mathbf{c}grad\,\mathbf{u} - \mathbf{au} + \mathbf{Y}) + \boldsymbol{\alpha}\mathbf{u} + \boldsymbol{\beta}grad\,\mathbf{u} = \mathbf{f} \qquad (2.30)$$

To emulate the PDE to be solved for in (2.18), $\boldsymbol{\alpha}$, $\boldsymbol{\beta}$, and $\mathbf{Y}$ correspond to zero matrices and $\mathbf{c} = \boldsymbol{\varepsilon}$. Therefore, the coefficients of the PDE are discontinuous at the

boundaries of two adjacent constituents inside the unit cell. The right hand side corresponds basically to the divergence of these discrete coefficients that are equivalent to Dirac delta functions at the constituents' boundaries with infinite values. The integral of the right hand side across a boundary equals the difference of the constituents' coefficients of the domains sharing that boundary. However, the Dirac δ distribution cannot be expressed as a function that COMSOL Multiphysics is able to calculate numerically. Therefore, this challenge is overcome by preserving the finite element method's weak formulation of the right hand side in its original form. The weak formulation is obtained by multiplying the partial differential equation by an approximate solution field, v, and manipulation using integration by parts over the solution domain. The right hand side of the weak formulation at the constituent boundaries is assigned the coefficient difference value Φ multiplied by the approximate solution field v directly as indicated by (2.31).

$$\int_\sigma \delta v = \Phi v \tag{2.31}$$

Practically, we set the source term $\mathbf{f}$ on the right hand side of (2.29) to zero and assign the constituent boundaries with the corresponding coefficient difference Φ.

Periodicity condition requires θ to be equal at opposite boundaries of the unit cell which completes the boundary value unit cell problem defined in (2.18). Figure 2.3 depicts the solved intermediate θ field distribution for the material distribution of the unit cell in Figure 2.2.
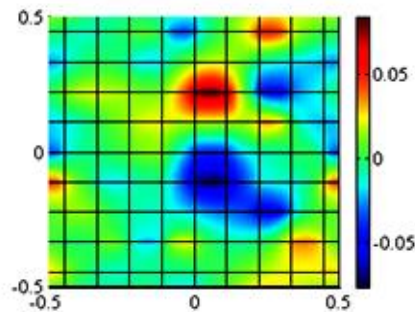
Figure 2.3 Intermediate θ^2 field distribution obtained via COMSOL for material distribution of unit cell in Figure 2.2

The field data is then post-processed in MATLAB and the homogenized constitutive parameter is solved using (2.29). The homogenized permittivity tensor ε_{eff} calculated for the unit cell example in Figure 2.2 is equal to, $\begin{bmatrix} 46.28 & 0.22 \\ 0.23 & 69.19 \end{bmatrix}$

2.2.1 Validation of the homogenized material model

The material model based on homogenization was introduced and implemented in previous sections. In this section, results of the proposed material model are compared with results obtained from mixing formulas for different inclusions and unit cell configurations shown in Figure 2.5 and Figure 2.6.

| | | |
| (a) | (b) | (c) |
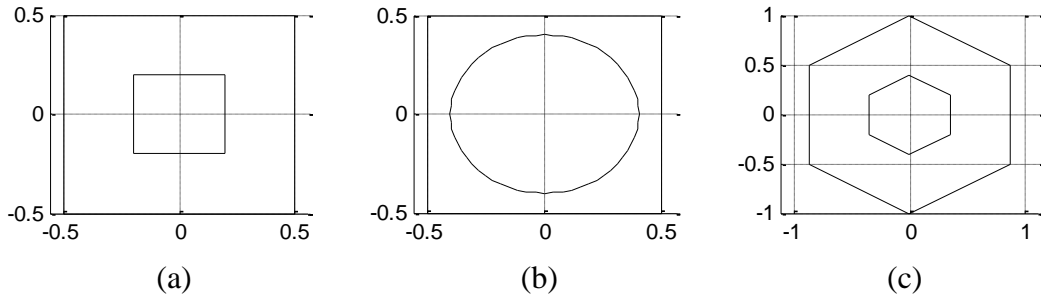
Figure 2.4 A square shaped unit cell with (a) square and (b) circular inclusions, and (c) a honeycomb shaped unit cell with a honeycomb inclusion. Volume fraction of the inclusions is 0.4

Figure 2.4 depicts a square shaped unit cell with (a) square and (b) circular inclusions, and (c) a honeycomb shaped unit cell with a honeycomb inclusion with a volume fraction of 0.4 each. The volume fraction is the ratio of the inclusion volume to the volume of the unit cell.

Mixing formulas such as the Maxwell-Garnett and Bruggeman are discussed in detail in [126] and results obtained using these formulas are depicted in Figure 2.5. Results belong to unit cells with a host and inclusion permittivity of 1 and 80, respectively. Figure 2.6 presents results for the same mixing formulas for unit cells with reverse host and inclusion permittivities. Simulations to obtain homogenized material model results were run at a uniform volume fraction sampling with a stepsize of 0.025 ranging from a volume fraction of 0, i.e. no inclusion, to 1 with no host configuration for the square and the honeycomb cases, and from 0 to 0.775 volume fraction for the

circular inclusion since higher volume fractions are geometrically not attainable for circular inclusions. As the results show, proposed material model shows a close behavior to the Maxwell-Garnet curve for all volume fractions. A small deviation is observed in the circular case at higher inclusion volume fractions with all results attaining values between predictions of the Maxwell-Garnet and Bruggeman curves.

As a second validation, the numerical implementation of the material model is simulated with fabricated designs in literature. Figure 2.7 compares the proposed model with Banks et.al. [41] for unit cell configurations with 2.7 and 1.003 of host and circular inclusion dielectric constants and with results of Zouhdi et al. in Figure 2.8 for unit cells with 1 and 80 of host and square inclusion dielectric constants, respectively. A perfect match of the results as observed for both comparisons proves the reliability of the homogenization based modeling tool.
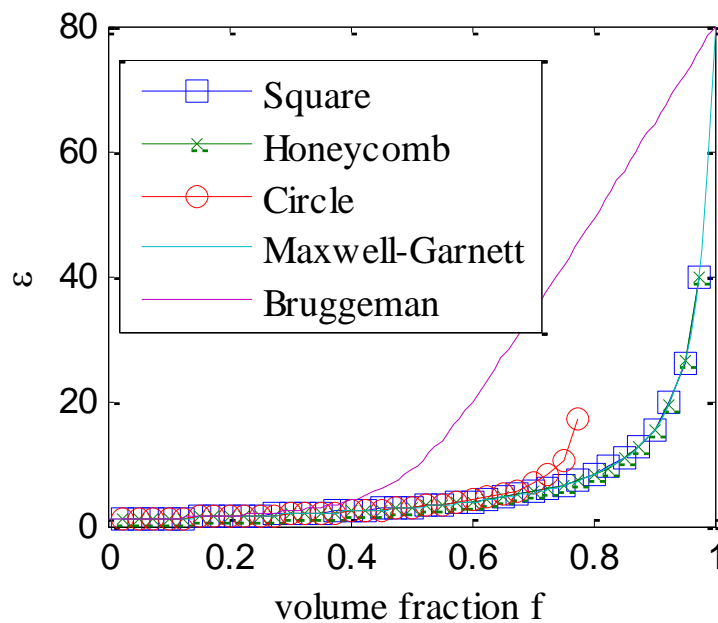
Figure 2.5 Effective dielectric constant vs. volume fraction of different inclusions in various unit cell configurations: Square in square, honeycomb in honeycomb and circles in square unit cells. Comparison is done with Maxwell Garnett, Bruggeman of host to inclusion ratio of 1-80
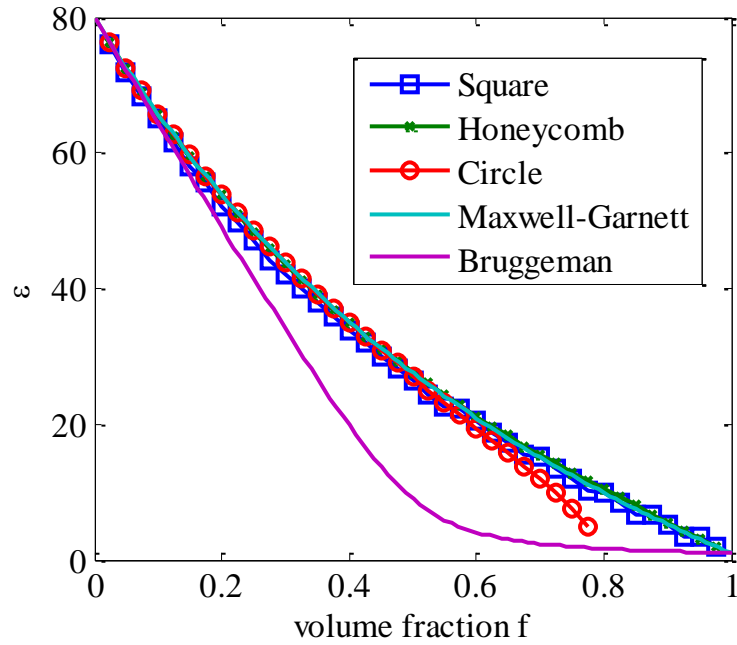
Figure 2.6 Effective dielectric constant vs. volume fraction of different inclusions in various unit cell configurations. Comparison is done with Maxwell Garnett, Bruggeman of host to inclusion ratio of 80-1
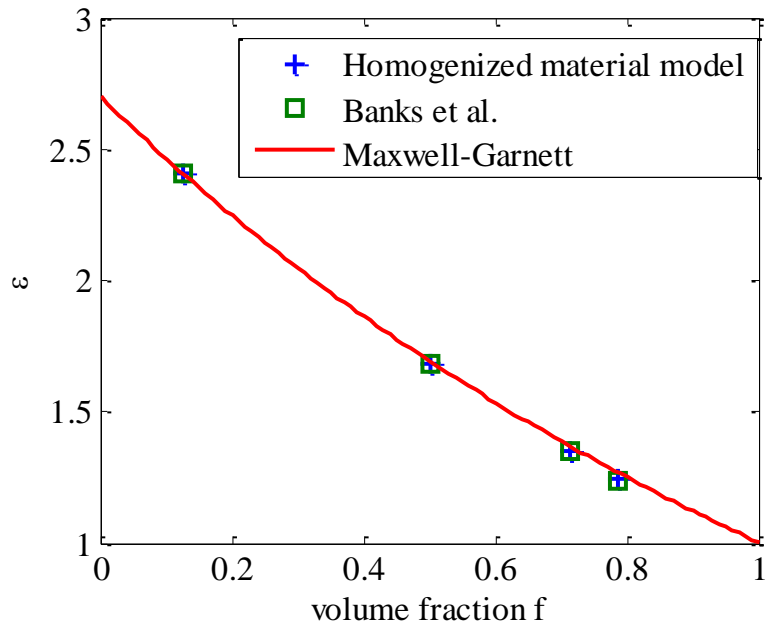
Figure 2.7 Comparison of proposed homogenized based method against model proposed by Banks et al. and Maxwell-Garnett formula
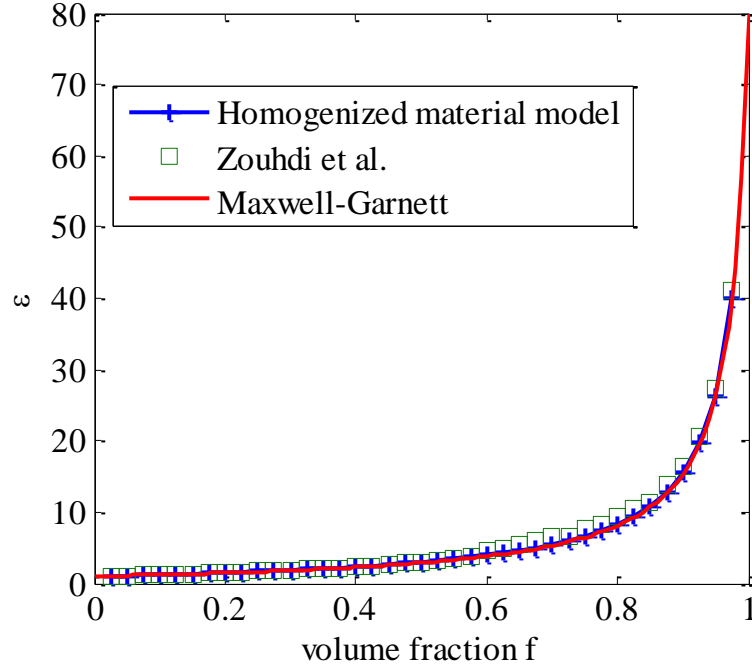
Figure 2.8 Comparison of proposed homogenized based method against model proposed by Zouhdi et al. and Maxwell-Garnett formula.

2.3 **Bounds on the Effective Tensor of Constitutive Parameters**

Before moving towards using the earlier derived material models in design studies targeting desired dielectric and/or magnetic properties of the material matrices represented by their permittivity and permeability matrices, one needs to assure that the constituent material phases are physically able to produce these characteristics. This can be done under certain conditions using the so called 'bounds study' relying on the use of mixing formulas. The randomness of the constituents geometry inside the unit cell gave rise to the birth of different mixing formulas in literature to calculate the effective parameters and it is fair to say that no mixing rule can be claimed universal. The pioneers of the effective characterization include the Maxwell Garnett mixing rule [127], the Bruggeman mixing formula [39] and coherent potential. The general form of the mixing formula [126] is given by

$$\frac{\varepsilon_{eff}-\varepsilon_e}{\varepsilon_{eff}+2\varepsilon_e+\nu\left(\varepsilon_{eff}-\varepsilon_e\right)} = f\frac{\varepsilon_i-\varepsilon_e}{\varepsilon_i+2\varepsilon_e+\nu\left(\varepsilon_{eff}-\varepsilon_e\right)} \tag{2.32}$$

where ε_{eff} is the effective permittivity, ε_e is the host permittivity, ε_i is the inclusion permittivity, f is the volume fraction of the inclusion in the unit cell and the non-dimensional parameter ν is the formula type deterministic parameter; $\nu = 0$ returns the Maxwell-Garnett formula, $\nu = 3$ results in the coherent potential formula ,and $\nu = 1$ yields the Bruggeman mixing formula.

There are still many other mixing formulas [128]. If the inclusions are not spherical, their average polarizaition is higher and the mixing rules have to be modified accordingly. As will be shown later in this thesis, for separate non-intervening inclusions, Maxwell Garnett is closer to the simulation results whereas other simulation studies in literature show that when clustering effect is allowed, Bruggeman formula is more precise. Also, one should bear in mind that these formulas are all applicable to two phase constituents only.

The bounds are similar to the mixing formulas; they are functions of the dielectric constants of the constituents (host and inclusion) and the volume fractions of the inclusion. The intuitive bound on the effective parameter is the one limited by the constituent constitutive parameters;

$$\min\{\varepsilon_i, \varepsilon_e\} \leq \varepsilon_{eff} \leq \max\{\varepsilon_i, \varepsilon_e\} \tag{2.33}$$

A more restrictive material bound called the Wiener bound [129] is given as follows

$$\frac{\varepsilon_i \varepsilon_e}{f\varepsilon_e + (1-f)\varepsilon_i} \leq \varepsilon_{eff} \leq f\varepsilon_i + (1-f)\varepsilon_e \tag{2.34}$$

where the lower bound is the inverse of the volumetric average of the permittivity inverse and the upper bound is merely the volume averaging of the compound. This bound is only applicable to inclusion of aligned plates. The applied electric field must be parallel (perpendicular) to the plates giving rise to no (maximum) depolarization and maximum (minimum) contribution to the effective parameter. A more restrictive effective parameter limit is also available through the Hashin-Shtrikman bound [130] as follows

$$\varepsilon_e + \cfrac{f}{\cfrac{1}{\varepsilon_i - \varepsilon_e} + \cfrac{(1-f)}{3\varepsilon_e}} \leq \varepsilon_{eff} \leq \varepsilon_i + \cfrac{1-f}{\cfrac{1}{\varepsilon_e - \varepsilon_i} + \cfrac{f}{3\varepsilon_i}} \tag{2.35}$$

The lower limit here is basically the Maxwell Garnett formula whereas the upper bound is the inverse of the Maxwell Garnet obtained by exchanging the inclusion and the host in the formula. Research studies in the late 70's restricted the limits even further [131, 132]. By assuming $\varepsilon_e \prec \varepsilon_i$ high order bounds are derived with tuning parameters related to the unit cell shape and the symmetry of the inclusions.

These formulas are restrictive and need much attention regarding their assumptions for practical applications. Sihvola [133] considers two main deviation examples where the effective permittivity can either be higher or lower than their constituents. The first one is due to cross-coupling effects where the real part of the effective permittivity is out of limits of its constitutive component values in both directions. For example, Sihvola shows that the effective permittivity can violate the upper limit for lossy mixtures (conductor inclusions where the coupling of the polarization and conduction currents affects the electrodynamic processes within the unit cell). He also presents an example where values violating the lower bounds are observed in a magnetoelectric example where the electric-electric interaction is not enough and the material response is a six-by-six-dyadic and a single component of this material matrix can display unexpected properties (exceeding the limits) in the homogenized form at the macroscale level. The permittivity in these examples is no longer scalar; either a complex number or a tensor. The bounds have to be reprinted in higher dimensions in order to treat these cases. The other cause of violation is due to the statistical character of random materials. Bounds, which are usually derived for special statistical topological configurations, can be broken due to the statistical nature of their constituent distribution inside the material. Bounds on the effective tensor of two phases parameters were derived and developed in [134-136] by putting limits on the Taylor expansion coefficients of the Pade Approximation of the effective parameter tensors. Nevertheless, the focus was on the structural limit represented by the volume fraction of a known calculated or measured effective permittivity. Beche et al. [137] derived the theoretical formulation of the bounds on effective dielectric tensors based on a composition method and a statistical discretization approach. In this thesis we follow their formulation with same notation given as:

$$\varepsilon_{eff}^{y_1 \circ y_2} = \begin{bmatrix} \dfrac{\varepsilon_2 \left(f_1 \varepsilon_1 + f_2 \varepsilon_2 \right)}{f_1 \varepsilon_2 + f_1 f_2 \varepsilon_1 + \left(f_2 \right)^2 \varepsilon_2} & 0 & 0 \\[4mm] 0 & \dfrac{\varepsilon_2 \varepsilon_1 \left(f_1 + f_1 f_2 + \left(f_2 \right)^2 \right)}{f_1 \varepsilon_2 + f_2 \varepsilon_1} & 0 \\[4mm] 0 & 0 & \left(f_1 \right)^2 \varepsilon_1 + f_1 f_2 \varepsilon_2 + f_2 \varepsilon_2 \end{bmatrix} \qquad (2.36)$$

$$\varepsilon_{eff}^{y_2 \circ y_1} = \begin{bmatrix} \dfrac{\varepsilon_2 \varepsilon_1 \left(f_1 + f_1 f_2 + \left(f_2 \right)^2 \right)}{f_1 \varepsilon_2 + f_2 \varepsilon_1} & 0 & 0 \\[4mm] 0 & \dfrac{\varepsilon_2 \left(f_1 \varepsilon_1 + f_2 \varepsilon_2 \right)}{f_1 \varepsilon_2 + f_1 f_2 \varepsilon_1 + \left(f_2 \right)^2 \varepsilon_2} & 0 \\[4mm] 0 & 0 & \left(f_1 \right)^2 \varepsilon_1 + f_1 f_2 \varepsilon_2 + f_2 \varepsilon_2 \end{bmatrix} \qquad (2.37)$$

where ε_1 and ε_2 are the dielectric constants of the two phase constituents with volume fractions f_1 and f_2, respectively. The superscripts $y_1 \circ y_2$ ($y_2 \circ y_1$) are mathematical representations denoting the composition of y_1-y_2 (y_2-y_1) which is the integral over y_2 (y_1) of the limits in the y_1 (y_2)-direction of infinitesimal perpendicular strips of the unit cell. For more details the reader is referred to [137]. Note that the volume fractions of the constituents must add up to unity relating f_2 to f_1 through the following formula

$$f_2 = 1 - f_1 \qquad (2.38)$$

Relations in (2.35) and (2.37) account for the bounds of the effective permittivity tensor. As an example, we examine theses bounds for commercially available shades of MCT powders, with lowest possible value of $\varepsilon_1 = 20$ and highest available value of $\varepsilon_2 = 140$. Using the relations (2.36) and (2.37) we plot the corresponding effective permittivity tensors over the volume fraction $f_1 = [0 \ 1]$ as shown in Figure 2.9.
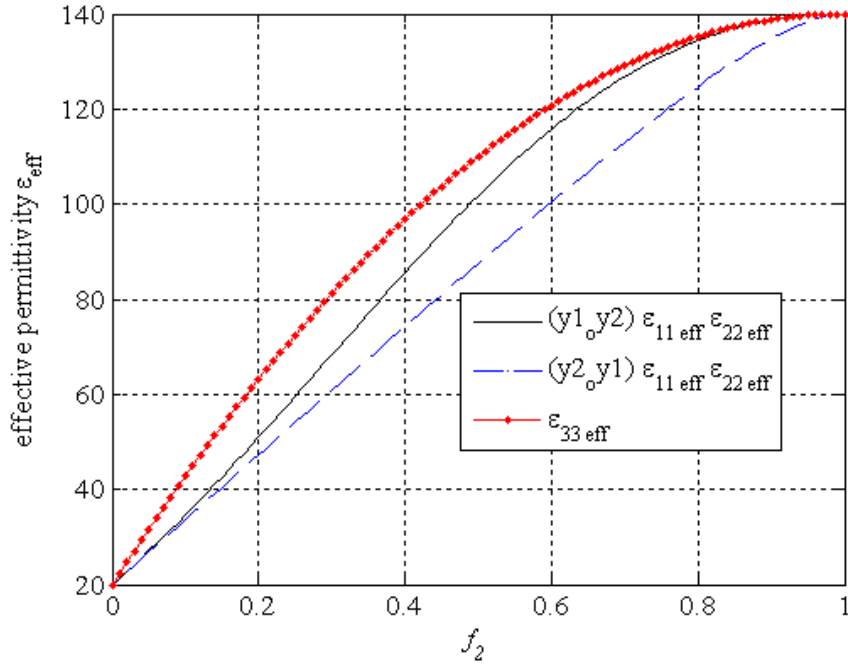
Figure 2.9. Upper (solid) and lower (dashed) limits of the effective permittivity in the x-y plane and the effective permittivity in the z direction where no material variation exists (dotted line)

The dashed and solid lines represent the lower and the upper bounds on ε_{11} and ε_{22}, respectively. Hence, according to the bound plot, for instance an effective dielectric constant of 45 or 70 cannot be obtained using the shades 20 and 140 alone since it lies out of the bounds. In the next section we will present an example where this restriction is overcome by using additional shades that lie between the extreme limits given above. Although the bounds above are not valid for more than two phases and one cannot check for the feasibility of such anisotropic desired properties using more than two shades, the application of given bound formulations for all combinations of possible shades (20,70,100,140) as shown in Figure 2.10 point for the feasibility of an effective dielectric constant range of 45 and possibly 70 since intuitively the original bounds for shades 20 and 70 alone are practically enlarged with a larger combined/union region residing inside the limit curves by the addition of other phases such as constituents with dielectric constants of 70 and 100.
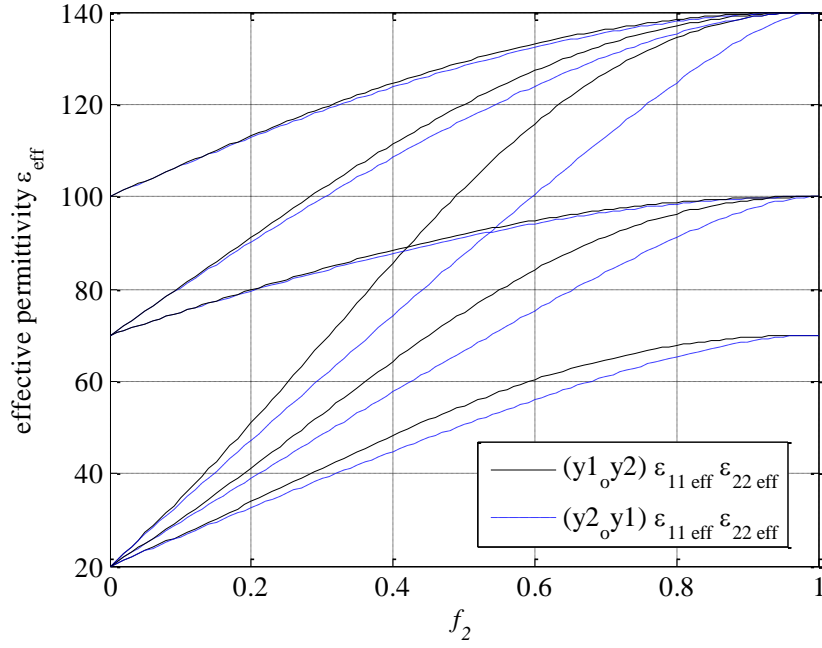
Figure 2.10. Upper (Solid) and lower (dashed) limits of the effective permittivity in the x-y plane for six constituent pairs (20,70), (20,100), (20,140), (70,100), (70,140), and (100,140) informally pointing for the feasibility of achieving effective elements of the dielectric constant of 45 and 70 using the four shades.

2.4 **Design Optimization Framework**

The design optimization framework is built by integrating the material model illustrated in the last section with a genetic algorithm optimizer using the Genetic Algorithm and Direct Search toolbox of MATLAB. The objective function within design studies corresponds to minimizing the error norm (e_{eff}) between the desired $\mathbf{\varepsilon}_{des}^{\mathcal{H}}$ and calculated $\mathbf{\varepsilon}^{\mathcal{H}}$ effective parameter tensors as

$$e_{eff} = \left\| \mathbf{\varepsilon}^{\mathcal{H}} - \mathbf{\varepsilon}_{des}^{\mathcal{H}} \right\|$$ (2.39)

The unit cell is discretized into design cells (see Figure 2.2) and the permeability/permittivity of each design cell is assigned as a design variable.

The Genetic Algorithm and Direct Search toolbox include routines for solving genetic optimization problems using direct search, genetic algorithm, and simulated annealing. The genetic algorithm is a method for solving optimization problems that is based on natural selection, the process that drives biological evolution. The genetic

algorithm repeatedly modifies a population of individual solutions. At each step, the genetic algorithm selects individuals at random from the current population to be parents and uses them to produce children for the next generation. Over successive generations, the population "evolves" toward an optimal solution. One can apply the genetic algorithm to solve a variety of optimization problems that are not well suited for standard optimization algorithms, including problems in which the objective function is discontinuous, non-differentiable, stochastic, or highly nonlinear. The objective function at hand is complex and therefore using gradient based optimization tools the solution would likely get trapped in local minima. Therefore, genetic algorithm seems a good choice for locating the global minimum of the objective function (2.39). The genetic algorithm is performed by calling the function ga that in its simplest form is given as follows

$$[\mathrm{x\ fval}] = \mathrm{ga}(\,\text{@fitnessfun, nvars, options}) \qquad (2.40)$$

where @fitnessfun is the function to be minimized, nvars is the number of design variables and options is a structure that stores the genetic algorithm tuning parameters. The fitness function @fitnessfun calls a Matlab m-file that takes the design variable values from a set of continuous or discrete values that stand for the constituents constitutive parameters of the discretized design cells. The fitness function then prepares the COMSOL model and updates the PDE coefficients $\left(\mathbf{a}^{e}\right)^{-1}$ and the weak form, Φ given by (2.31), of the boundary conditions between the design cells of the right hand side of (2.18) and also imposes periodicity at the unit cell boundaries. COMSOL PDE Coefficient Form Module then solves for the $\boldsymbol{\theta}$ field distribution and the results are then post-processd by another MatLab file to solve for the effective parameters according to (2.23).

A typical list of tuned genetic algorithm parameters for this problem with 9x9=81 design variables is given as the following: population size = 80; selection strategy function = remainder; scattered crossover function; scale parameter value = 0.75 and shrink mutation parameter value = 0.5.

2.4.1 Validation of the design framework

In this subsection four validation examples are demonstrated including an initial sanity check which proves that the design framework has the capabilities to design electromagnetic materials with both desired isotropic and anisotropic constitutive parameters from isotropic constituents.

2.4.1.1 Design of isotropic dielectric material tensor with homogenous phase

The isotropic design case tackled here is intended to validate the design framework by targeting an isotropic permittivity $\varepsilon_{des}^{\mathcal{H}} = 70$ using two material shades of $\varepsilon \in \{20,70\}$ which includes the desired homogeneous phase itself, hence serves as a sanity check example. The design unit cell is discretized into a 20x20 design variable cells that will be occupied by the material shades. The genetic algorithm converges to the correct naïve solution $\varepsilon^{\mathcal{H}} = 70$ in 357 generations. The genetic algorithm tuning parameters are shown in Table 2.1. Figure 2.11 depicts the convergence history of the GA optimization process.

Table 2.1 Genetic algorithm tuning parameters of the validation examples of the proposed design framework

		Validation example		
		isotropic homogeneous substrate	isotropic Inhomogeneous substrate	Anisotropc
Population size		60	20	80
Elite count		2	2	2
Crossover fraction		0.9	0.9	0.9
Maximum generations		500	500	500
Selection function		remainder	remainder	remainder
Cross over function		scattered	scattered	scattered
Mutation function	Scale	0.75	0.75	0.75
	Shrink	0.5	0.5	0.5
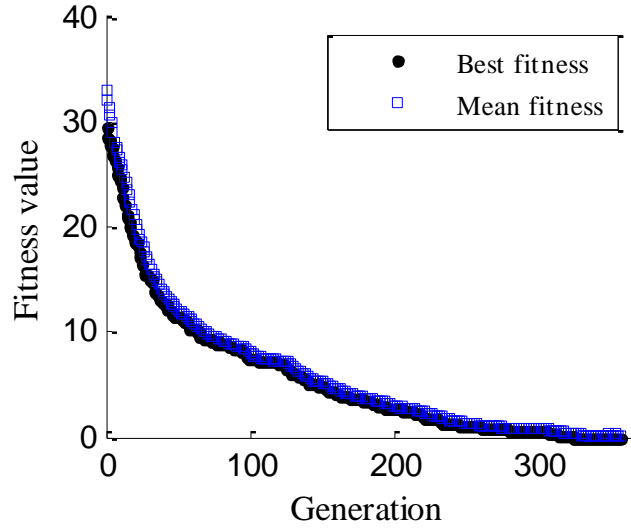
Figure 2.11 GA convergence history of a sanity check case of a unit cell with 20x20 design variable cells. Two material shades of $\varepsilon \in \{20,70\}$ with a desired isotropic $\varepsilon_{des}^{\mathcal{H}} = 70$ returns a homogeneous phase substrate of $\varepsilon^{\mathcal{H}} = 70$

2.4.1.2 Design of isotropic dielectric material tensor with inhomogeneous phases

In this design case conducted for the validation of the design framework, the same targeted isotropic permittivity of the last example $\varepsilon_{des}^{\mathcal{H}} = 70$ is desired with the constituents $\varepsilon \in \{1,100\}$, this time excluding the target phase dielectric constant of 70. The optimum design converged in 226 iterations as shown in the convergence history in Figure 2.14. The genetic algorithm tuning parameters used are given in Table 2.1. The error norm used in the optimization procedure according to relation (2.31) returns a value of 0.020908 for the optimum design with a homogenized dielectric tensor of $\varepsilon^{\mathcal{H}} = \begin{bmatrix} 70.01 & -0.02 \\ -0.01 & 70.00 \end{bmatrix}$. The resulting optimum material design distribution is shown in Figure 2.16. The volume fraction of the inclusion with $\varepsilon = 100$ returns a perfect match with the Maxwell-Garnet mixture formula both predicting a value of 69.94 for the dielectric constant.
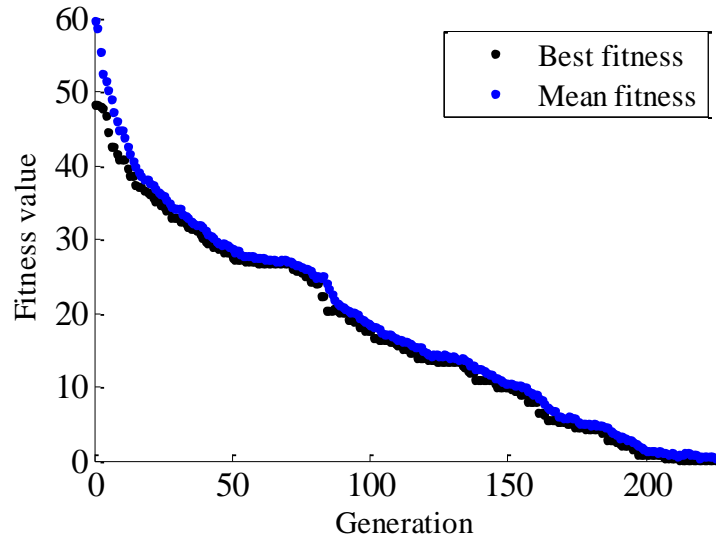
Figure 2.12 Genetic algorithm convergence history of a unit cell with 20x20 design variable cells: two material shades of $\varepsilon \in \{1,100\}$ with a desired isotropic $\varepsilon_{des}^{\mathcal{H}} = 70$ returns a material tensor of $\varepsilon^{\mathcal{H}} = \begin{bmatrix} 70.01 & -0.02 \\ -0.01 & 70.00 \end{bmatrix}$
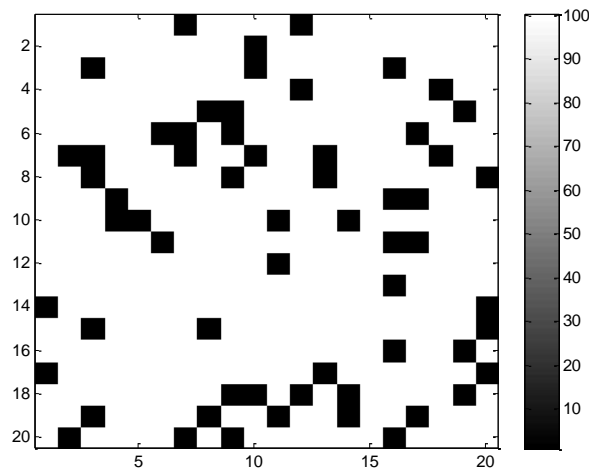
Figure 2.13 Resulting optimum material design of the example in Figure 2.12. Black and white shades are phases with dielectric constants 1 and 100, respectively

2.4.1.3 Design of an anisotropic dielectric material tensor

An anisotropic design case is conducted in this validation example for a desired permittivity tensor of

$$\boldsymbol{\varepsilon}_{des}^{\mathcal{H}} = \begin{bmatrix} 45 & 0 \\ 0 & 70 \end{bmatrix}.$$

The design unit cell is discretized into two different mesh sizes of 20x20 and 9x9 design variable cells. The design variables are selected from a subset of four material shades with different dielectric constant values of $\varepsilon \in \{20,70,100,140\}$. The genetic algorithm converges when the average change in the fitness value is less than a chosen tolerance value of 10^{-6}. The genetic algorithm returns an optimum dielectric material tensor of $\boldsymbol{\varepsilon}^{\mathcal{H}} = \begin{bmatrix} 45.52 & 0.00 \\ 0.03 & 69.47 \end{bmatrix}$ for the 20x20 discretization case with an error norm of 0.54 and $\boldsymbol{\varepsilon}^{\mathcal{H}} = \begin{bmatrix} 45.11 & 0.09 \\ 0.10 & 69.88 \end{bmatrix}$ for the 9x9 discretization case with an error norm of 0.15 defined according to (2.31). The convergence history of each run is depicted in Figure 2.14. As expected, the 9x9 configuration with 81 design variables converges faster than the 20x20 design configuration with 400 design variable cells (84 vs. 206 generations, respectively) because it has less number of design variables and consequently spans much smaller design search space. Nevertheless, the small error norm of the optimum design of the 9x9 cell proves that this number of discrete cells is enough to fulfill the design target requirements. The optimum material design obtained using the 20x20 discretization is shown in Figure 2.15. The material distribution of the optimum design using the 9x9 discretization is shown in Figure 2.16 (a) as a single unit cell and its 3x3 array configuration in Figure 2.16 (b) that was also fabricated. More specifically, a 3x3 array configuration obtained using a repetition of the unit cell design resulting from the first scheme is fabricated as shown in Figure 4 using Dry Powder Deposition (DPD) and commercial MCT ceramic powders (Trans-Tech Inc.) [138]. The resulting fabricated substrate in pressed form is shown in Figure 2.16 (b).
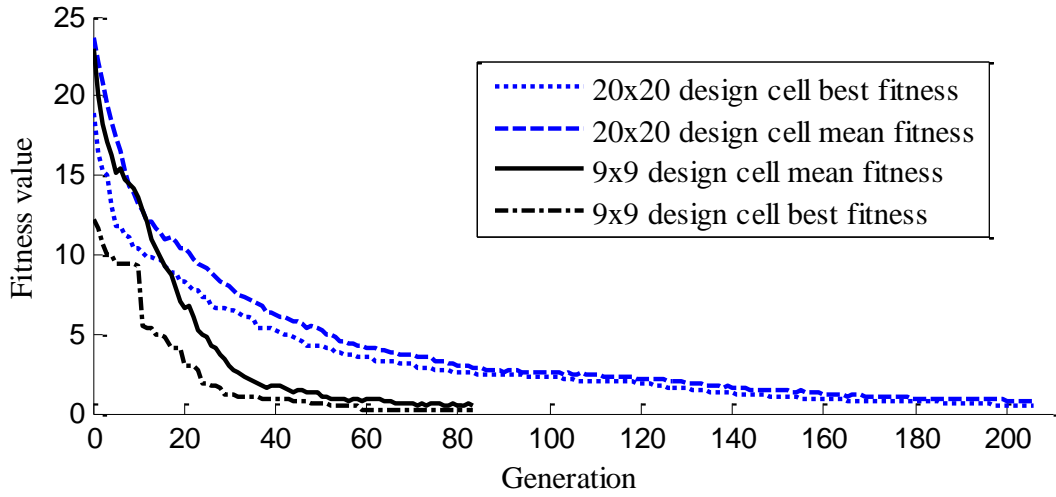
Figure 2.14 Genetic algorithm convergence history of a unit cell discretized with 20x20 and 9x9 design variable cells. Shades of $\varepsilon \in \{20,70,100,140\}$ with a desired anisotropic $\mathbf{\varepsilon}_{des}^{\mathcal{H}} = \begin{bmatrix} 45 & 0 \\ 0 & 70 \end{bmatrix}$ returns a homogenized substrate with $\mathbf{\varepsilon}^{\mathcal{H}} = \begin{bmatrix} 45.52 & 0.00 \\ 0.03 & 69.47 \end{bmatrix}$ of the 20x20 case and $\mathbf{\varepsilon}^{\mathcal{H}} = \begin{bmatrix} 45.11 & 0.09 \\ 0.10 & 69.88 \end{bmatrix}$ of the 9x9 case.
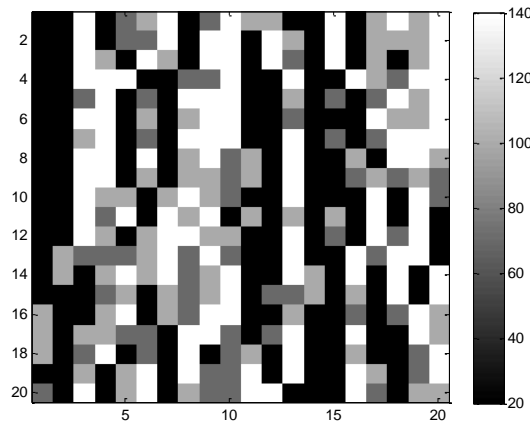
Figure 2.15 Optimum design of the 20x20 design example explained in Figure 2.14
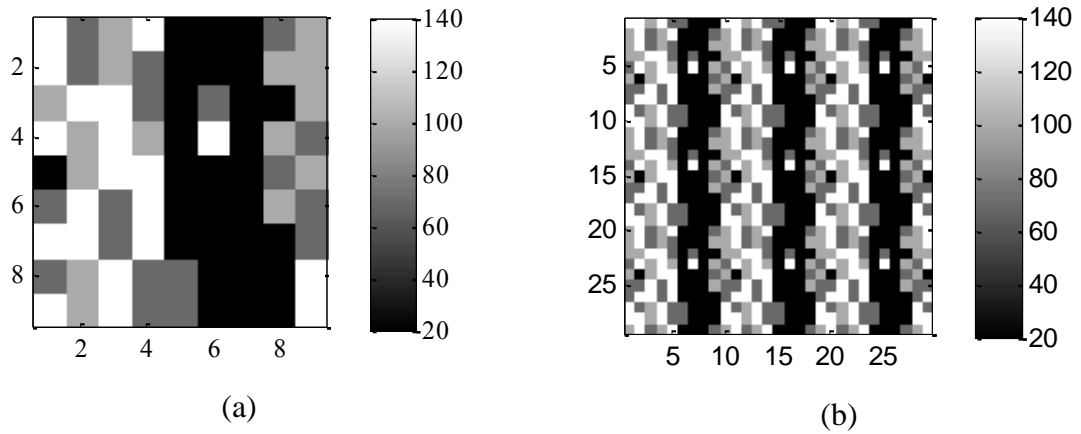
Figure 2.16 (a) Optimally designed unit cell for a homogenized substrate of the 9x9 design case explained in Figure 2.14 and (b) a 3x3 array of the design unit cell to be fabricated
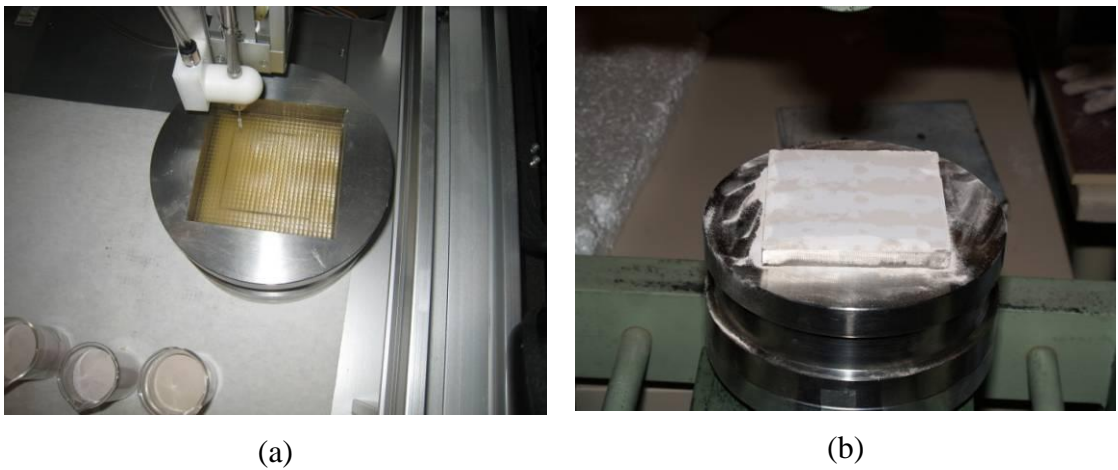
Figure 2.17 Automated dispensing machine in action when depositing available ceramic powder shades into a grid box $(10\,\text{cm} \times 10\,\text{cm})$ with desired material distribution of the 3x3 array of the 9x9 design variable configuration shown in Figure 2.16 (b) resulting in a desired deposited substrate

3 DESIGN OF MAGNETIC PHOTONIC CRYSTALS VIA HOMOGENIZED DIELECTRIC LAYERS

In this chapter we present an example of the application of the proposed synthesis framework to magnetic photonic crystals. Photonic crystals have been utilized in radio-frequency applications due to their extraordinary propagation characteristics [139-142]. Recently, a new class of photonic crystals was introduced from available material structures of rutile (TiO$_2$) and CVGs (Calcium Vanadium Garnett) [143]. When compared with photonic bandgap structures, they exhibit much larger gain and less volume. In what follows we briefly review the characteristics of these photonic crystals and present their key advantages.

Any photonic crystal supports slow electromagnetic modes associated with a vanishing group velocity $\partial\omega/\partial k = 0$ as shown in Figure 3.1. Regular band-edge (RBE) photonic crystals display this slow electromagnetic mode as the operational frequency approaches the band-edge frequency after which the propagation is prohibited. This slow down is associated with accumulation of electromagnetic energy and consequently radiating power.

Photonic bandgap materials gained attention after their introduction by Yablonovich [144] where an experiment was conducted and the modes of the well-known wood-pile structures were studied. Since the analytical formulation being established by Figotin et al. [145, 146] in 1996, a lot of research focused on the experimental investigation of various periodic dielectric structures (woodpiles, buried dots, cubic lattices, gratings, etc). Matching and total transmittance is difficult to achieve specifically for near the band edge frequency. Recent studies on photonic crystals overcome this drawback by working at frequencies far from the band edge or exhibit a degenerate band edge that flattens the $k - \omega$ band diagram and therefore a group velocity of zero is obtained at a wider range or bandwidth. More specifically, two types of crystals were proposed for near perfect matching of the incident wave at the interface of the crystal, namely degenerate band edge crystals (DBE) and magnetic photonic crystal (MPC) with a single inflection point (SIP). The DBE crystal (Figure 3.1 b) consists of dielectric layers only and has a transmittance rate of $\Delta\omega_{\mathrm{d}}^{1/4}$

compared with $\Delta\omega_{\mathrm{d}}^{1/2}$ of the regular band edge material (RBE) where $\Delta\omega_{\mathrm{d}}$ is the difference between the operational and band edge frequencies. Also the group velocity decreases faster in DBE's and is proportional to $\Delta\omega_{\mathrm{d}}^{3/4}$ as compared with $\Delta\omega_{\mathrm{d}}^{1/2}$ in RBE crystals. The latter, non-reciprocal Magnetic Photonic Crystals (MPC) are crystals with two misaligned anisotropic dielectric layers and one magnetic layer. They possess a transmittance coefficient of unity and a slower group velocity ($\Delta\omega_{\mathrm{d}}^{2/3}$). Figure 3.1 (a) – (c) depicts the band diagram of typical regular band edge crystals (RBEs), DBEs, and non-reciprocal MPCs.
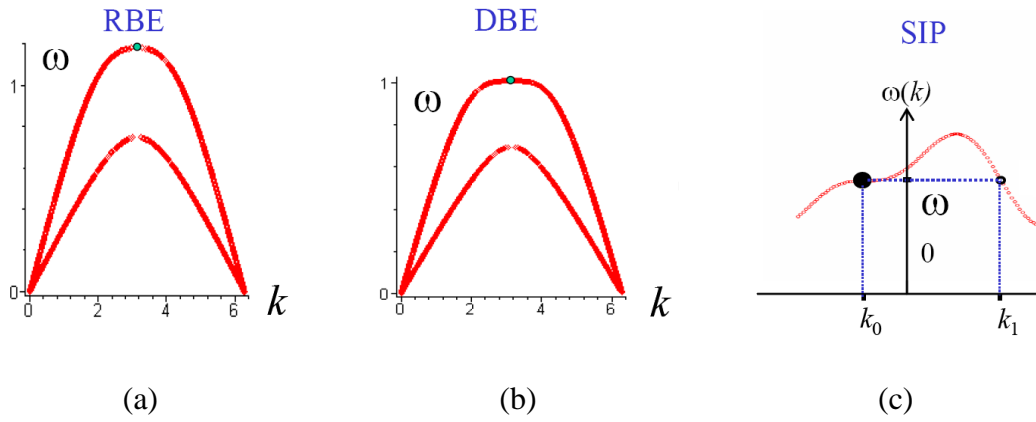
Figure 3.1 Band diagrams of typical (a) regular band edge (RBE), (b) degenerate band edge (DBE), and (c) magnetic photonic crystals (MPC's) associated with single inflection point (SIP)

Non-reciprocal magnetic photonic crystals as shown posses a single inflection point around which the group velocity and its first derivative with respect to the wavelength are zero and the third derivative is a finite non-zero value in order to force it to be as far as possible from the band edge frequency and enhance the transmittance; more details about the analytical formulation of the concept is discussed in [147, 148].

One-directional photonic crystals have been investigated in several studies by Mumcu et al. [5, 143, 149-151]. They also proposed to realize them by anisotropic layers of dielectrics such as rutile and a ferromagnetic layer of CVG, as demonstrated in Figure 3.2. The permittivity and permeability tensors of rutile are given as follows

$$\boldsymbol{\varepsilon}_A = \varepsilon_0 \begin{bmatrix} \varepsilon_a + \delta\cos 2\phi_A & \delta\sin 2\phi_A & 0 \\ \delta\sin 2\phi_A & \varepsilon_a - \delta\cos 2\phi_A & 0 \\ 0 & 0 & \varepsilon_{az} \end{bmatrix} \tag{3.1}$$

$$\boldsymbol{\mu}_A = \mu_0 \begin{bmatrix} 1 & 0 & 0 \\ 0 & 1 & 0 \\ 0 & 0 & 1 \end{bmatrix} \tag{3.2}$$

where $\phi_A = -\pi/12$ is the misalignment angle between the principal axes of the two dielectric layers, $\varepsilon_a = 125$, $\delta = 40$, and ε_0 and μ_0 are the free-space permittivity and permeability constants, respectively.
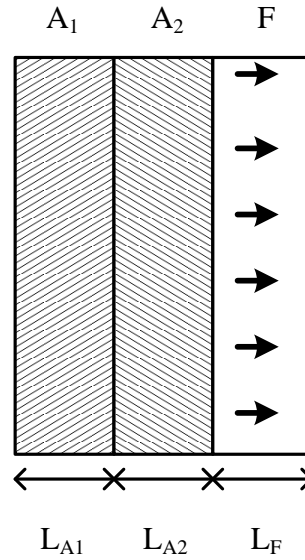
Figure 3.2 One-directional magnetic photonic crystal unit cell structure.

Optimization of these structures is attempted by chirping the layers thicknesses shown in Figure 3.2 or shuffling them as discussed in [149, 150, 152, 153] in order to enhance the single inflection point behavior or harness the amplitude growth inside the crystal in order to achieve higher gain. In these studies, optimal designs were restricted to the only available anisotropic material found in nature such as rutile. Since it will allow for larger choices of materials for their realization with possibly improved performances, the material layers themselves of the MPC are targeted within the design. Our goal in this chapter is to prove that we can realize anisotropic dielectric layers that

are macroscopically equivalent to rutile from off-the-shelf isotropic materials using the material design framework proposed in this thesis.

3.1 **Realization of an Effective MPC Dielectric Tensor**

A unit cell of a one-dimensional magnetic photonic crystal consisting of two dielectric layers A_1 and A_2 and a magnetic layer F is shown in Figure 3.2. The periodicity of the unit cell of the photonic crystal is in the z-direction which is also the propagation direction. The layers are assumed homogeneous and infinite in the x and y-directions. The electric and magnetic fields occupy the plane perpendicular to the plane of propagation, i.e. the x-y plane. Therefore, the key parameters that affect the propagation characteristics (and therefore are to be designed for) have no z-coupled components in the dielectric permittivity tensor and therefore can be written as a 2×2 matrix as follows

$$\mathbf{\varepsilon}_A = \varepsilon_0 \begin{bmatrix} \varepsilon_a + \delta \cos 2\phi_A & \delta \sin 2\phi_A \\ \delta \sin 2\phi_A & \varepsilon_a - \delta \cos 2\phi_A \end{bmatrix} \tag{3.3}$$

The misalignment angle ϕ_A of each layer is given in [143]: $\phi_A = 0$ for the first layer, A_1, and $\phi_A = -\pi/12$ for the second layer, A_2, $\varepsilon_a = 125$, and $\delta = 40$ in (3.3) the following matrices are obtained

$$\mathbf{\varepsilon}_{A_1} = \begin{bmatrix} 165 & 0 \\ 0 & 85 \end{bmatrix} \text{ and } \mathbf{\varepsilon}_{A_2} = \begin{bmatrix} 159.64 & -20 \\ -20 & 90.36 \end{bmatrix} \tag{3.4}$$

Although the second layer can be obtained by the rotation of the first layer by $15°$ around the z-axis in the clockwise direction, we treat it as a separate design problem in order to assess the capability of the framework to design fully anisotropic matrices and negative entries. To start with, in the next section we first apply the bound study introduced in Section 2.3 to investigate feasible designs.

3.1.1 Bound investigations of effective MPC tensors with off-the-shelf dielectrics

Within the available off-the-shelf dielectric shades, we start with 4 available constituents of $\varepsilon \in \{20,70,140,240\}$. Using (2.36) and (2.37) we calculate the lower and upper limits of the effective constitutive parameters of the following shade-pair combinations: $\varepsilon \in \{20,70\}$, $\varepsilon \in \{20,140\}$ $\varepsilon \in \{20,240\}$, $\varepsilon \in \{70,140\}$, $\varepsilon \in \{70,240\}$, and $\varepsilon \in \{140,240\}$. As can be deferred from the calculated bound curves in Figure 3.4, the desired anisotropic dielectric properties of 165 and 85 per the MPC material matrices in (2.36) and (2.37) cannot be obtained using any of these shade-pairs only. However, it can be seen that the desired values lie between the maximum and minimum limits of a couple of shade pairs (20,70), (20,140), (20,240), (70,140), (70,240), and (140,240). For instance, if we examine the (20,140) and (20,240) shade limits we can see that desired values of 165 and 85 lie between the lower and upper bounds. Although this is not a rigorous method of determining the achievability of desired constitutive matrices with more than two shades, it gives an intuitive idea about the feasibility to obtain these properties. In addition, it directly indicates that a two-shade composite of the mentioned permittivities does not meet specified needs for the realization of MPC crystals.
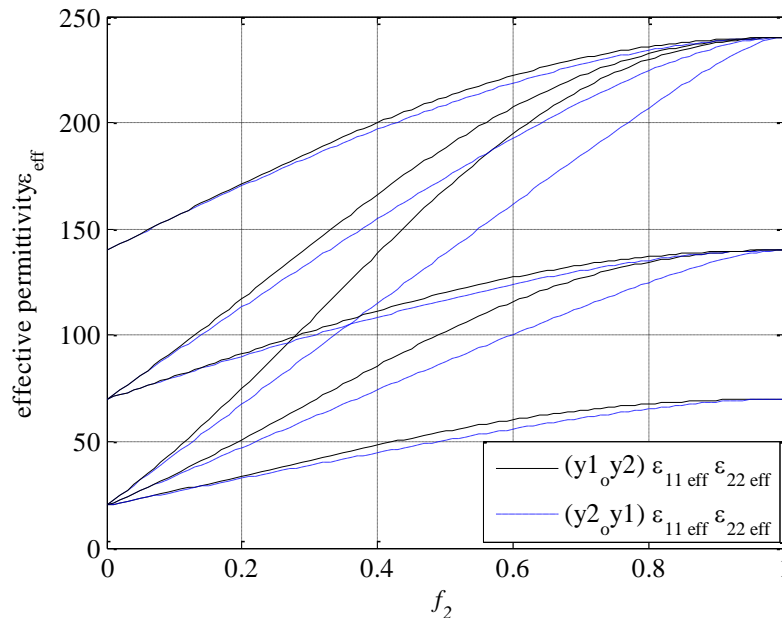
Figure 3.3. Upper (solid) and lower (dashed) limits of the effective permittivity in the x-y plane for six constituent pairs (20,70), (20,140), (20,240), (70,140), (70,240), and (140,240): informally pointing for the feasibility of achieving an effective elements of the dielectric constant of 165 and 85 using the four shades.

3.1.2 Design results of an MPC material tensor using off-the-shelf dielectrics

Similar to the bound study in Section 2.3, the actual design process starts with the available 4 shades of dielectric constants $\varepsilon \in \{20,70,140,240\}$. The design unit cell is discretized into 9x9 variable cells. The design variables are selected from a subset of four material shades with different dielectric constant values of $\varepsilon \in \{20,70,140,240\}$. The genetic algorithm using the material model proposed here converges when the average change in the fitness value is less than a set tolerance value of 10^{-6}. As a result, the genetic algorithm returned an effective dielectric tensor of $\boldsymbol{\varepsilon}^{\mathcal{H}} = \begin{bmatrix} 165.04 & -0.01 \\ -0.01 & 85.07 \end{bmatrix}$ for the first layer A_1 with an error norm of 0.08 and an effective dielectric tensor of $\boldsymbol{\varepsilon}^{\mathcal{H}} = \begin{bmatrix} 155.80 & -14.68 \\ -14.74 & 94.24 \end{bmatrix}$ for the second layer A_2 with an error norm of 6.5825. It is noted that the error norm (calculated according to (2.39)) of the 'optimally' designed A_2 layer is relatively larger than zero. Alternatively, instead of using the resulting A_2 layer as is, it is known that by rotating the resulting A_1 layer by 15 degrees in the clockwise direction, the desired optimum material tensor given by (3.3) should be achieved. Hence, re-investigating the resulting design topologies given by Figure 3.4 and Figure 3.5, the design cell size seems to be too large turning the design domain resolution not fine enough to represent the second layer A_2 by a 15 degrees rotation of the designed layer A_1. In order to overcome this problem, the number of design cells was increased to 18x18 and the optimization process was restarted with the last generation of the earlier algorithm that resulted in the design shown in Figure 3.6 for layer A_2 with a 9x9 cell discretization. The design with finer discretization converged to an effective dielectric tensor of $\boldsymbol{\varepsilon}^{\mathcal{H}} = \begin{bmatrix} 159.55 & -19.96 \\ -19.97 & 90.37 \end{bmatrix}$ with an error norm of 0.10. The resulting optimum material design is shown in Figure 3.6. Convergence histories of the three design cases for layers A_1 and A_2 mentioned above are depicted in Figure 3.7. It is noted that the diagonal matrix with only 9x9 design variable cells has the fastest convergence history around 160 generations.
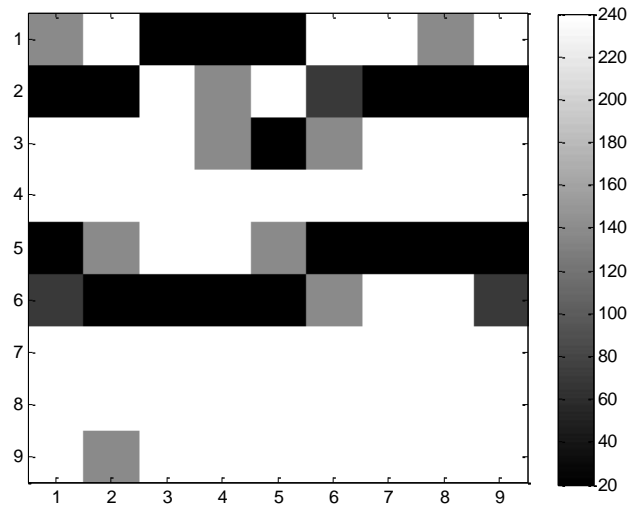
Figure 3.4 Optimum design of layer A_1 with a 9x9 discretization using dielectric shades of $\varepsilon \in \{20,70,140,240\}$
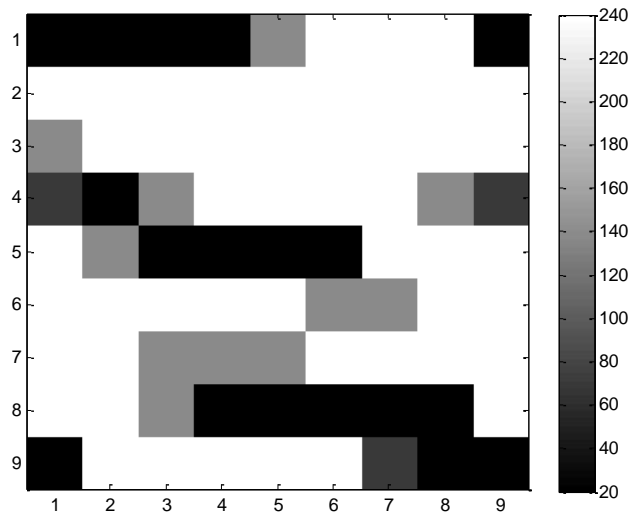
Figure 3.5 Optimum design of layer A_2 with a 9x9 discretization using dielectric shades of $\varepsilon \in \{20,70,140,240\}$
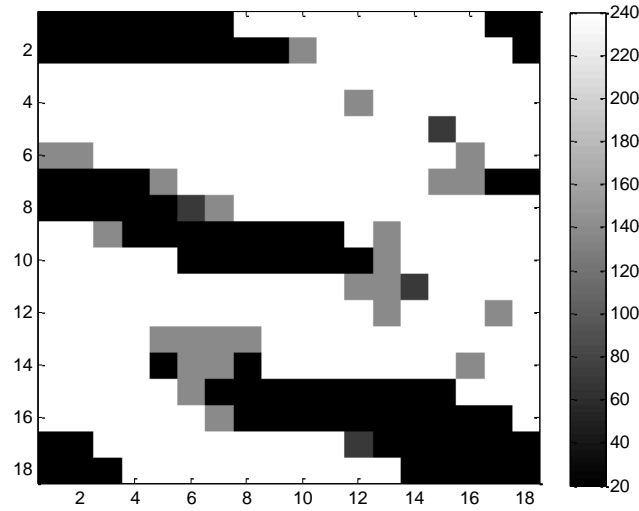
Figure 3.6 Optimum design of layer A_2 with 18x18 design variable cells and using dielectric shades of $\varepsilon \in \{20,70,140,240\}$
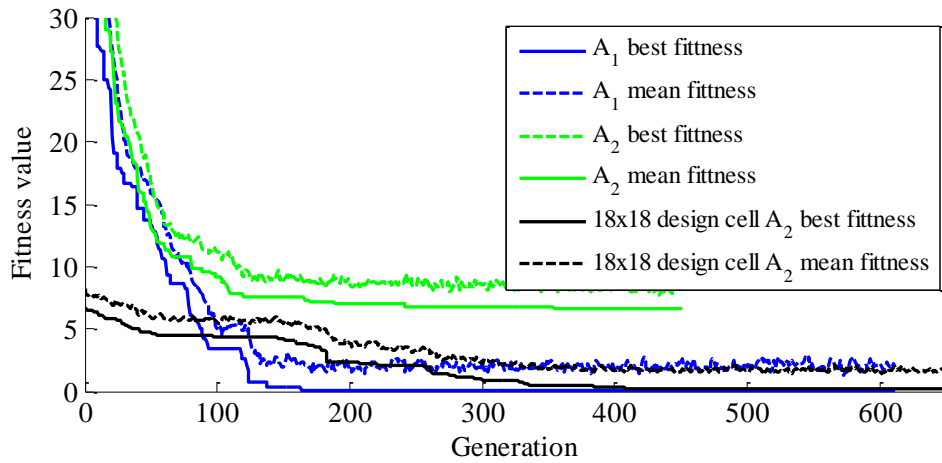
Figure 3.7 Genetic algorithm convergence history of the design for layers A1 and A2 via 9x9 discretization (blue and green) and for layer A2 via 18x18 discretizaiton (black)

3.2 **Analysis of the Non-Reciprocal MPC with Designed Dielectric Material Tensor**

In this section the magnetic photonic crystal made of layers A_1 and A_2 designed in Section 3.1.2 (shown in Figure 3.4 and Figure 3.6, respectively) is analyzed via simulations in order to validate its desired performance exhibiting a single inflection point at the frequency of interest. We first validate the simulation results for the MPC studied in Figure 6 of reference [149] with dielectric material tensors corresponding to

designed layers A_1 and A_2 integrated to ferromagnetic layers with L_f=0.3975 L_A and L_A=0.5695 mm, as shown in Figure 3.2. All the dielectric and magnetic dielectric tensors are assumed to be invariant with frequency as the frequency range of interest where the design is shown to exhibit a single inflection point is very narrow and around 10 GHz. In order to simulate the MPC, COMSOL Multiphysics RF module was used. More specifically, first an eigenvalue analysis is conducted in order to determine the eigenfrequency to start with and then the simulation is swept over the wave vector k using harmonic analysis to obtain the dispersion diagram. Figure 3.8 shows the total energy density distribution for an MPC unit cell model with an eigenfrequency of 9.987 GHz at Bloch wavenumber of 3. It is noted that the thickness in the x-y directions (1/20 of the unit cell length) are much shorter than the in the wave propagation direction (z-direction) in order to prevent modes in the eigenfrequency analysis from forming along the x or y-direction. The MPC is homogeneous in the x-y plane and the periodicity at the boundary directions of the finite thickness in this plane ensures this assumption. A simulation model in 3D is required to be able to express the layers' constitutive parameters in an appropriate tensorial form.
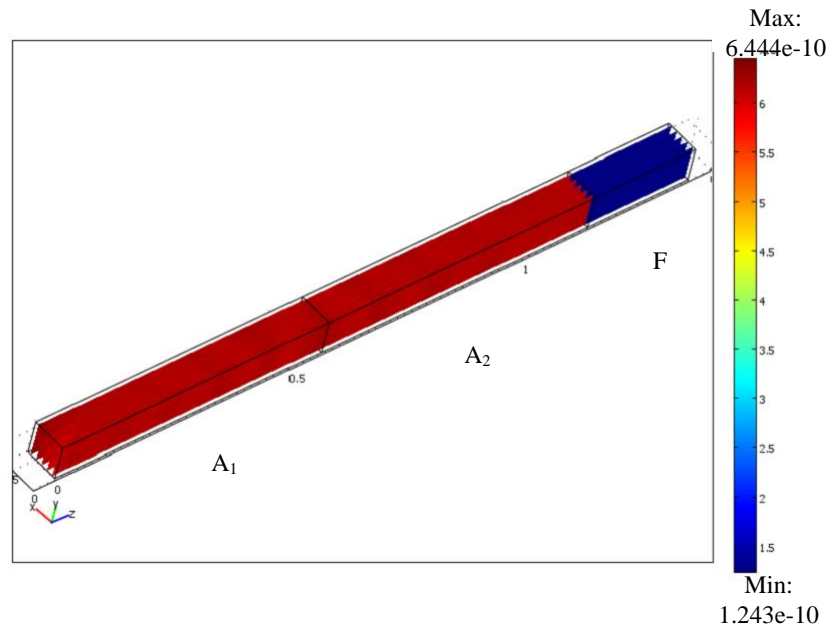
Figure 3.8 Time averaged total energy density distribution [J/m^3] for a non-reciprocal magnetic photonic crystal unit cell modeled in COMSOL Multiphysics RF module

The results of the simulated band diagram of the original MPC with rutile dielectric layers of A_1 and A_2 and the designed layers with isotropic constituents obtained in Section 3.1.2 shows a perfect agreement as shown in Figure 3.9.
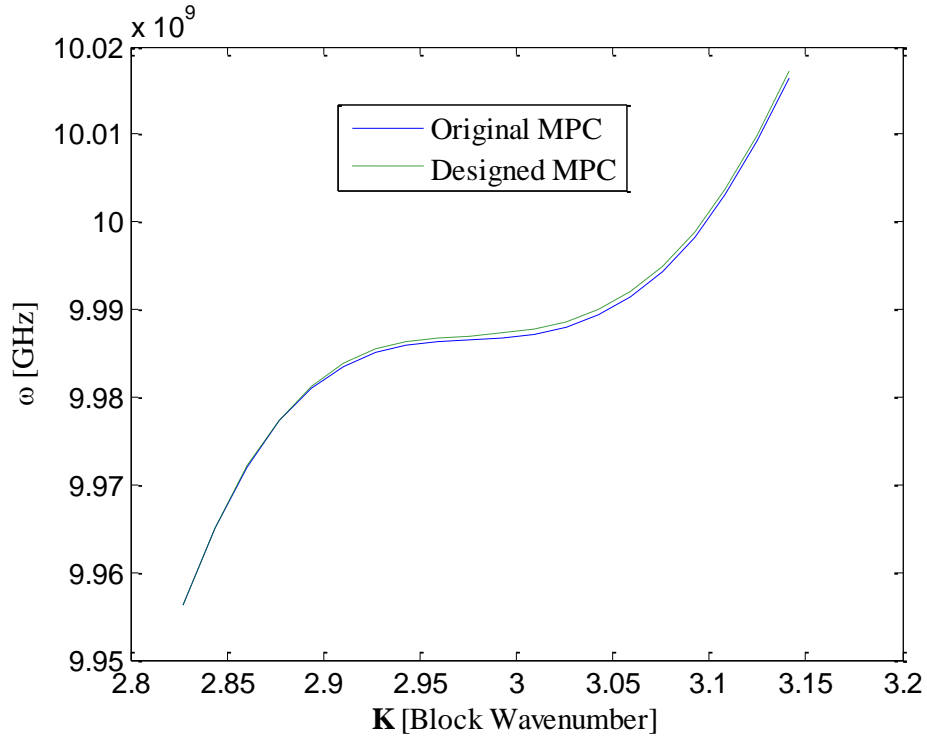
Figure 3.9 Comparison of the dispersion relation of the non-reciprocal MPC with original dielectric layers (made of rutile) vs. the designed layers (from off the shelf materials)

3.3 **Conclusion**

This chapter presented an application of the material design framework developed in Chapter 2 to design dielectric layers for MPC's. Results show that this method is capable of realizing desired anisotropic electromagnetic constitutive parameters using simple off-the-shelf isotropic materials. This is the first step towards opening a new avenue where novel material designs are no longer restricted to a limited number of available materials. In short, desired properties or device performances can be directly linked to material constitutive parameters that are not readily available nor can be easily realized but designed from scratch for their alternatives via the proposed design tool. Future work includes realization and measurement of designed MPC's.

4 SPEED-UP TECHNIQUES BASED ON BAYESIAN TRAINED RATIONAL FUNCTIONS

Design optimization has been a difficult, demanding but necessary task for the development of novel commercial radio frequency applications such as miniaturization of antennas without sacrifice in their bandwidth and radiation efficiency. The need for design, preferably design optimization, is pertinent to the competing physics of these metrics, which has been the focus of researchers for the past two decades. However, global synthesis via heuristic search techniques relies on fast and accurate reanalysis, which presents itself as a bottleneck in large scale electromagnetic search studies. Therefore, unless design studies are limited to only a few number of design variables [100], simulation based electromagnetic design studies can become impractical. In this chapter, an approximation scheme suitable for the frequency response of electromagnetic systems such as multi-resonance return loss of antennas is investigated The proposed technique allows for fast and accurate reanalysis within electromagnetic design optimization studies.

Basis functions employed within the interpolation models have great influence on the quality of the surface approximation. Among alternatives, rational functions offer an attractive solution for providing approximate resonances due to their inherent pole predicting behavior. Therefore, they are likely to yield a more accurate approximation for a larger class of problems with a reduced computational effort. Hence, their use has resulted in various representations of resonance type responses with reasonable number of support points (points where the functional values are known) [106-112].

The rational approximation scheme proposed in this chapter employs an easy-to-train and simple decision making classifier based on Bayes' theorem to predict multi-resonance return loss curves of electromagnetic (EM) devices with complex topologies.

The Bayesian classifier infers a controlling parameter that controls the shape of the resulting resonances associated with a rational interpolator of quadratic numerator and denominator. The remaining rational function parameters are determined by given boundary conditions of the interval of interest. In addition, selection of sample points adaptively is known to affect the interpolation quality. The Bayesian classifier is also

used in adaptively sampling the frequency range by bisecting and hence refining the interval under consideration. The Bayesian trained rational function proves to have a powerful yet, unlike other standard approaches such as Neural Networks, simple approximation capability based on statistics and just a single controlling parameter.

This chapter is organized as follows: Section 4.1 presents the theory of Bayesian based rational functions. The method is applied on a design optimization example of a patch antenna with multi-resonant return loss response in Section 4.2. Results and conclusion follow in Sections 4.3 and 4.4.

4.1 Background on Bayesian Trained Rational Functions

In this section, the theoretical background of the proposed rational function interpolation scheme based on the Bayesian classifier is presented. In the following subsections we introduce the reader to rational functions in Section 4.1.1 and Bayes' theory in Section 4.1.2. The proposed Bayesian trained rational function is presented later.

4.1.1 Rational functions

Rational functions provide the advantage of well approximating resonances due to their inherent pole predicting behavior. Therefore, they are likely to yield an accurate approximation valid for a larger class of problems with a reduced computational effort and therefore are well suited for approximating frequency dependent electromagnetic responses. As a result, their use has resulted in various representations of resonance type curves with reasonable number of support points [106-112].

The general form of the rational function is given by a ratio of two polynomials of orders N and D respectively and is given as follows:

$$\phi(x) = \frac{a_0 + a_1 x + a_2 x^2 + \cdots}{1 + b_1 x + b_2 x^2 + \cdots} = \frac{a_0 + \sum_{n=1}^{N} a_n x^n}{1 + \sum_{d=1}^{D} b_d x^d} \tag{4.1}$$

where x is the independent variable (usually frequency in EM applications), ϕ is the rational interpolation of the response, and $(a_0 \cdots a_N)$ and $(b_1 \cdots b_N)$ are coefficients to be

solved for that determine the rational function response. The roots of the denominator (also called poles of the rational function) give rise to the rational function attaining infinite value, which physically corresponds to a sharp resonance. As will be explained later in Section 4.1.3, complex roots correspond to less sharp resonances than real roots.

4.1.2 Bayes theorem

The Bayes theorem shows how one conditional probability (such as the probability of a hypothesis given observed evidence) depends on its inverse (in this case, the probability of that evidence given the hypothesis). The theorem expresses the posterior probability (i.e. after evidence E is observed) of a hypothesis H in terms of the prior probabilities of H and E, and the probability of E given H. In its simplest setting involving only discrete distributions, Bayes' theorem relates the conditional and prior probabilities of events *A* and *B*, where *B* has a non-vanishing probability P with the following formula:

$$P(A) = \frac{P(A/B)P(B)}{P(B/A)} \qquad (4.2)$$

A classifier is a mapping from a feature/evidence $\mathbf{x}$ to a discrete set of classes/hypotheses. A naive Bayes classifier is a simple probabilistic classifier based on applying Bayes' theorem (from Bayesian statistics) with strong (naive) independence assumptions. A more descriptive term for the underlying probability model would be 'independent feature model'. Estimating the prior probabilities of the feature $\mathbf{x}$ and the probability of $\mathbf{x}$ given class C and noting that the probability of the class C is the same for all classes, the likelihood or posterior probability of the evidence $\mathbf{x}$ in its most general form is given as follows

$$p(\mathbf{x}) = \frac{1}{(2\pi)^{d/2} |\mathbf{\Sigma}|^{1/2}} \exp\left(-\frac{1}{2}(\mathbf{x}-\mathbf{\mu})^T \mathbf{\Sigma}^{-1}(\mathbf{x}-\mathbf{\mu})\right) \qquad (4.3)$$

where $\mathbf{x}$ is the attribute's variable vector and $\mathbf{\mu}$ and $\mathbf{\Sigma}$ are the *mean* vector and *covariance* matrix of evidence of the training set belonging to each class C,

respectively, and d refers to the dimension of the problem. Despite their naive designs and apparently over-simplified assumptions, naive Bayes classifiers often work much better in many complex real-world situations than one might expect.

4.1.3 Bayesian trained rational function

The numerator and denominator of the selected rational function y as expressed in equation (4.4) for the proposed interpolation scheme here are polynomials of second order. The order of the denominator is chosen to closely follow the behavior of the return loss curve by allowing for a pole existence that emulates a resonance for each interval. To ensure smooth interpolations of successive intervals for a multi-resonance response curve (see Figure 4.8 in Section 4.2), function values and first order derivatives are imposed as constraints at the interval endpoints. The rational function's general form is given as

$$y = \frac{\beta_1 + \beta_2 x + \beta_3 x^2}{1 + \beta_4 x + \beta_5 x^2} \tag{4.4}$$

where the coefficients $\beta_1 \cdots \beta_5$ are solved such that 4 boundary conditions within the interval of interest are satisfied. The fifth coefficient is left out and could be determined based on another imposed interpolation constraint such as a second derivative requirement. Here, instead of following the standard approach to determine the remaining coefficient, a heuristic based approach is followed by employing the Bayes' theorem such that the control of a possible existence of a pole inside the interval is possible. For mathematical convenience, the fifth parameter β_5 is linked to the forth parameter β_4 by the following relation

$$\beta_5 = \frac{coef}{4} \beta_4{}^2 \tag{4.5}$$

This relation yields a new parameter, $coef$, which essentially replaces β_5 and can be tuned such that the rational function possesses a pole (a resonance) by enforcing the real part of the denominator root to lie inside the interval of interest. In addition, it is

responsible for creating an imaginary part of the pole that in turn determines the sharpness of the resonance as will be discussed later.

In a normalized interval with endpoints $x_0 = 0$ and $x_1 = 1$, the boundary conditions are given by $y(0) = y_0$, $y'(0) = y_0'$, $y(1) = y_1$, $y'(1) = y_1'$ as shown in Figure 4.1. Solving for these boundary conditions using (4.4) and (4.5), the coefficients $\beta_1 \cdots \beta_4$ are analytically determined as:

$$\beta_1 = y_0$$
$$\beta_4 = \frac{-b \pm \sqrt{b^2 - 4ac}}{2a}$$
$$\beta_2 = y_0' + y_0 \beta_4$$
$$\beta_3 = y_1 \left(1 + \beta_4 + \left(\frac{coef}{4} \right) \beta_4^2 \right) - \beta_1 - \beta_2$$

$$(4.6)$$

where

$$\begin{cases} a = -\left(\frac{coef}{4} \right) y_1' \\ b = y_1 - y_0 - y_1' \\ c = 2(y_1 - y_0) - \left(y_1' + y_0' \right) \end{cases}$$

Complex value solutions for these coefficients are allowed as they still yield real values for function and derivatives at endpoints and hence satisfy the imposed boundary conditions.
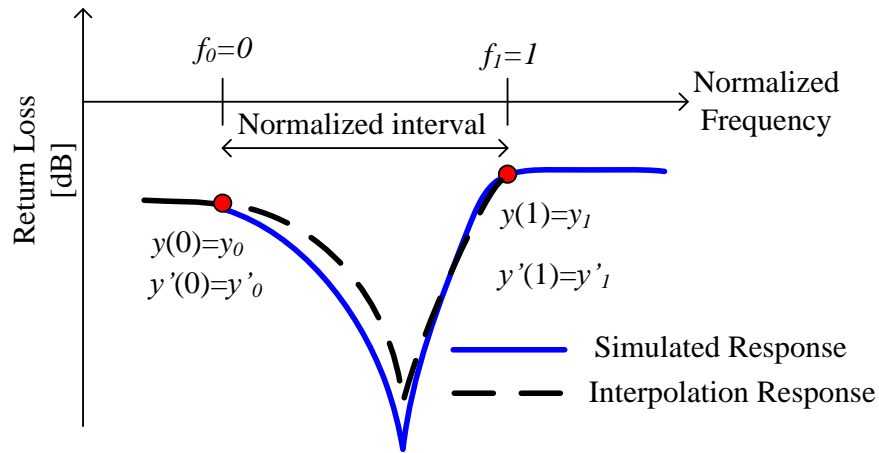
Figure 4.1 Enforced boundary conditions in normalized frequency intervals

The poles of the rational function are determined by the roots of the denominator, denoted by r, and therefore result in singularities in the form of sharp resonances. Moreover, certain function characteristics can be easily deferred based on the characteristics of the root denominator r. If the real part of r attains a value between 0 and 1, i.e. falls inside the normalized interval, then the rational function naturally possesses a pole inside the interval of interest. Whenever the function variable x equals the real part of the complex pole r, the denominator approaches a minimum value without changing sign. Hence, the rational function is highly likely to attain a resonance since this x value with a zero imaginary part is the closest to the complex root. If the interval contains a resonance, complex roots are desired since they do not allow the denominator to change sign and consequently enforce occurrence of poles as depicted in the response shown with the dashed curve in Figure 4.2 as opposed to the solid curve behavior observed in the case of real valued roots. Although a possible remedy to the sign change problem of the real root is simply to take the negative of the norm, the poles still cause singularities which physically correspond to existence of very sharp resonances attaining infinite values and are not common in electromagnetic responses of practical devices. Therefore, the selection of the parameter $coef$ plays a significant role in determining three important behavior characteristics: 1) The existence of the root inside the normalized interval, 2) the data type of the root (complex versus real), and 3) the imaginary to real part ratio of the complex root that controls the sharpness of the resonance. The effect of the parameter $coef$ on the resulting interpolation response function is depicted in Figure 4.3.

(a)   (b)

Figure 4.2 Typical rational function responses with a) real poles and b) complex poles
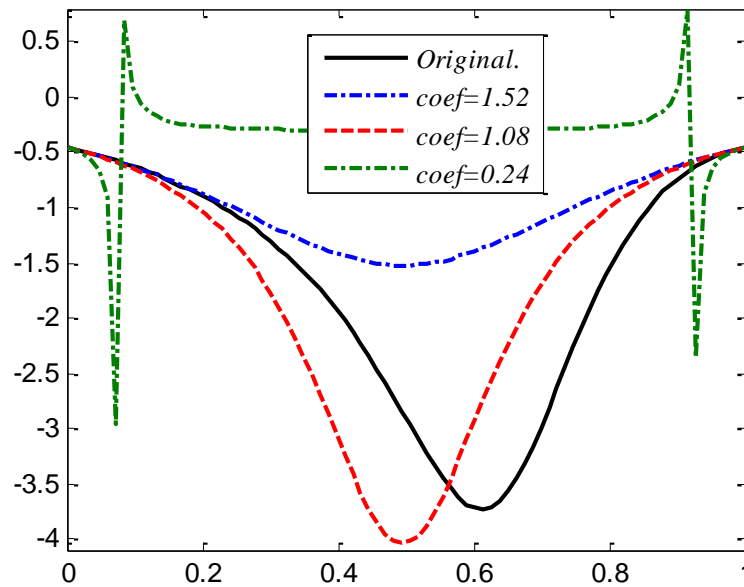
Figure 4.3 Effect of parameter *coef* on the interpolation response

Using the rational function in (4.5) and the β coefficient descriptions in (4.6) ,the roots of the denominator of the rational function given by (4.4) can be represented in terms of *coef*, y_1', b and c as shown in (4.7). Since the objective is to solve the inverse problem, i.e. assign the root to a certain value, (4.7) is solved for *coef* which is a nonlinear relation and hence requires suitable iterative solvers such as Newton-

Raphson, Levenbrg-Marquardt, etc. The parameters sgn_1 and sgn_2 can be either positive or negative and hence their sign combinations give rise to four different root possibilities given by (4.7). The roots $r_{1,2}$ are assigned to each endpoint of the scaled interval $[0\ 1]$ and the resulting coefficients $coef_1$ and $coef_2$ refer to the left and right endpoints with $r = 0$ and $r = 1$, respectively. These are responsible for attaining real roots at the endpoints. Among possible solutions for $coef_1$'s and $coef_2$'s, the chosen solution set is the one within the range $[coef_1\ coef_2]$ that does not allow for a *coef* solution at the endpoints and hence a real root inside the interval does not exist. Moreover, complex root findings are ensured by satisfying the condition $coef \succ 1$ as can be easily shown using (4.7).

$$r_{1,2} = \frac{b}{c \cdot coef} \quad \frac{-\frac{sgn_1 sgn_2 \sqrt{1 - coef} \sqrt{b^2 + coef \cdot y'c^2}}{c \cdot coef}}{+\frac{sgn_1 \sqrt{b^2 + coef \cdot y'c^2}}{c \cdot coef}} \tag{4.7}$$
$$\frac{b\, sgn_2 \sqrt{1 - coef}}{c \cdot coef}$$

If the original data is not available inside the interval, tuning the parameter *coef* to closely follow the response is not possible. This problem can be overcome by heuristically determining the optimum value for the parameter *coef* using Bayesian classifier [154]. The training set consists of optimum *coef* values for different response curve intervals and imposed boundary conditions, similar to the representative interval response shown in Figure 4.1. The optimum *coef* values are found using brute-force calculations by sweeping intervals $[coef_1\ coef_2]$ with small increments in order to minimize the error square norm between the interpolated and simulated/original response. The Bayesian classifier learns from the probabilistic nature of the training set and assigns classes of discrete *coef* values to test sets accordingly. The goal is to classify boundary conditions of intervals in order to minimize the probability of *coef* 's misclassification. In d-dimensions the general multivariate normal probability density function can is given by (4.3). The *coef* parameter to be assigned to the interval is

appointed to the class with maximum likelihood. The classes are assigned discrete *coef* values closest to the optimum before the classifier is trained.

Since adaptive selection of sample points is known to affect the interpolation quality, a semi-adaptive procedure is employed here that allows for selecting sample points by bisecting the interval of interest. This, although restricted by only bisecting the interval under consideration, allows for non-uniform sampling and hence creation of uneven interval lengths. Therefore, another classifier 'bisect', relying on the same attributes used in training the *coef* classifier is defined for producing an unevenly distributed sample data within the semi-adaptive scheme.

Additional attributes such as interval length or a combination of attributes are also considered in order to enhance the training process. Similarly, occurrence of positive and negative slopes at the boundaries is taken into account by considering the norm of the attributes leading to a better training performance. This improvement is linked to the symmetry characteristics of an interval containing a resonance. For example, a highly positive slope followed by a slightly negative slope is likely to contain a similar resonance to that interval which has a symmetric behavior, namely an interval with a slightly positive slope followed by a highly negative slope. To take this characteristic into account, a new attribute is used in the form of the product of the maximum slope norm of intervals and the interval length, i.e. $y'_{max}\Delta x$. Figure 4.4 (a) depicts the resulting likelihood of the two classes of the 'bisect' classifier x, namely 'bisect the interval' (blue) and 'do not bisect the interval' classifier (red) versus the attribute $y'_{max}\Delta x$. As a result, a high overlap between the classes' likelihood can be observed. Figure 4.4 (b) shows the attribute distribution across various intervals used in the training set.
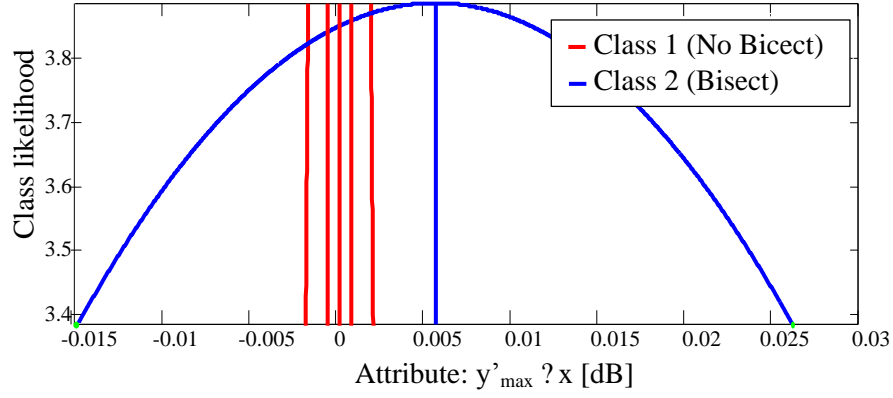
(a)
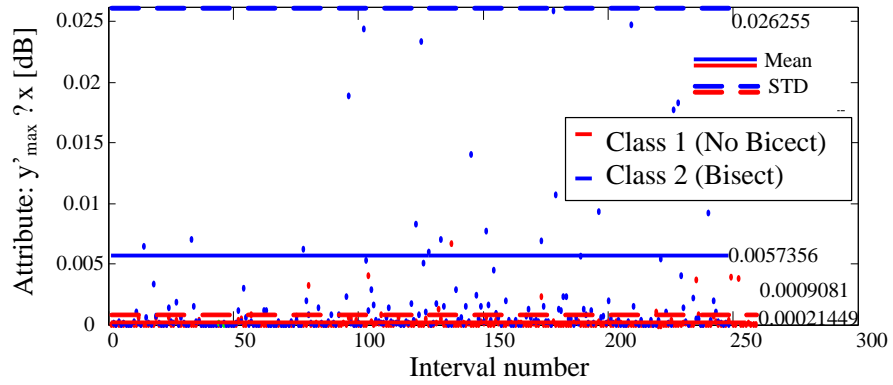
(b)

Figure 4.4 (a) Likelihood distribution versus attribute and (b) attribute distribution versus interval number for attribute $y'_{max}\Delta x$ of 'Bisect' classifier with (blue) and without (red) bisect classes.

Based on experiments, the original plane attributes represented by the boundary conditions suffer from even more overlaps and consequently exhibit worse performance. One way to account for this problem is to scale the attribute by a factor that depends on the attribute value itself. The aim is to suppress the values that are significantly lower than some threshold value. The chosen suppression formula is given in (4.8).

Since the boundary conditions imposed at interval endpoints are used to predict the response behavior inside the interval, the attribute likelihoods are highly overlapping which results in a more complicated classifier training process and deteriorates the classification results. The overlapping problem can be detected by investigating the likelihood distribution of both classes of the 'bisect' classifier versus an attribute value. Several improvements are performed on the attributes in order to separate their

likelihoods and enhance the classification results. For example, the training data of each attribute for the *coef* Bayesian classifier is scaled with respect to the mean value.

$$y = \left(bx^c\right)^{supfac} \tag{4.8}$$

Figure 4.5 depicts the response of a linear function input according to relation (4.8) with a selected threshold value of $x = 0.8$ around which the output is observed to be suppressed more for values below the threshold and less suppressed otherwise. The suppression increases as the penalty factor *supfac* increases and the parameters b and c are determined according to the threshold value. Implementation of this suppression formula to the attribute of $y'_{max}\Delta x$ shown in Figure 4.4 resulted in a significant reduction of the earlier overlap and a more robust training set attribute as shown in Figure 4.6.
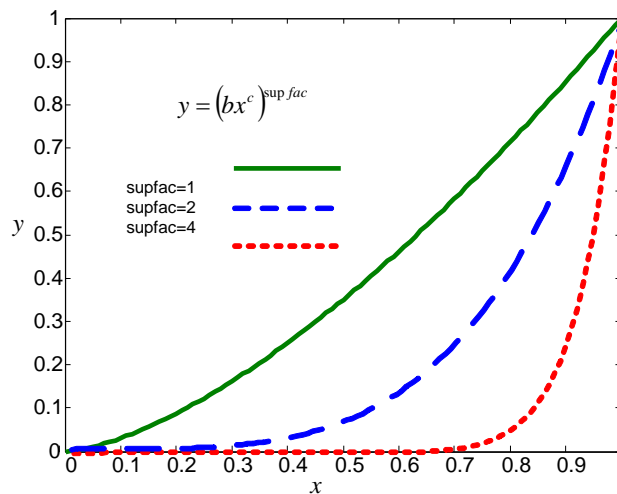
Figure 4.5 Effect of penalization factor *supfac* on the response of a linear function input according to the relation (4.8). The threshold around which the values are suppressed is chosen as $x = 0.8$.
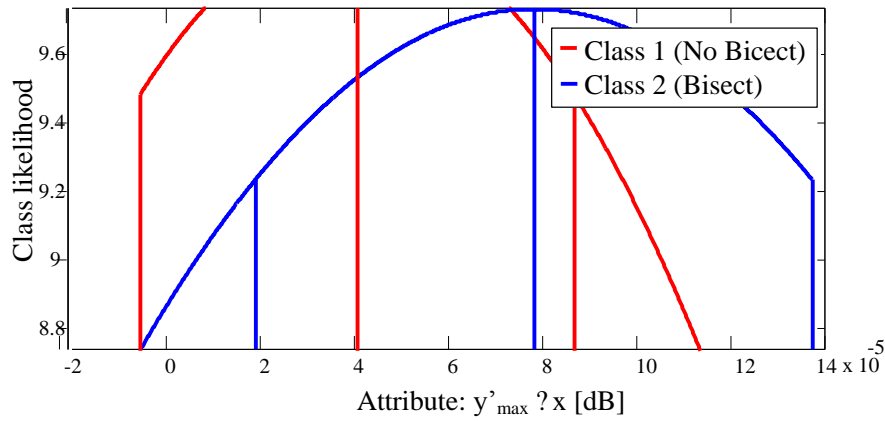
(a)
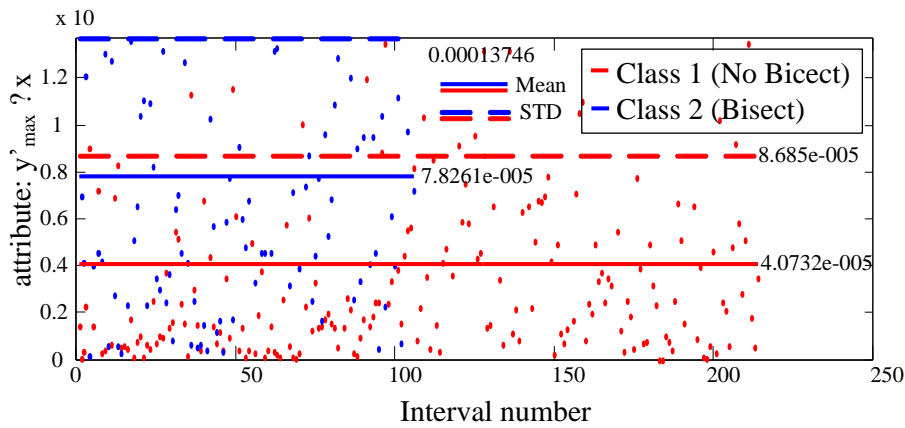
(b)

Figure 4.6 Suppressing the attribute $y'_{max}\Delta x$ in Figure 4.4 yields more separate classes represented by (a) their likelihood and (b) attribute value distribution

4.2 **Example Application of Interpolation Scheme**

In this section the proposed Bayesian based rational interpolation scheme is applied to approximately predict the return loss response of a microstrip antenna. The resulting approximation is used in a heuristic/global based optimization scheme integrated to a topology optimization method in order to find the optimum conductor patch and material distribution of the substrate that maximizes the antenna bandwidth [3] subject to given size requirements.

The design domain for the material is comprised of the volumetric space that the dielectric material of the antenna substrate occupies, see Figure 4.7. It is 0.3715 cm thick and covers a surface area of $2.5\,\text{cm} \times 2.5\,\text{cm}$. The design domain of the printed surface conductor comprises the entire top surface of the substrate. The substrate is

discretized into $2 \times 20 \times 20 = 800$ triangular-prism-shaped finite elements. A design cell is considered to be a square prism composed of two adjacent triangular prisms and therefore reduces to a total of 400 design cells. The permittivity of each volumetric design cell is taken as a material design variable. The design domain for the conductor is similarly discretized into $2 \times 20 \times 20 = 800$ triangular finite element cells corresponding to a total of 400 square conductor design cells. Each design cell is essentially a design variable of on/off type representing presence or absence of conductor material in that specified design cell.
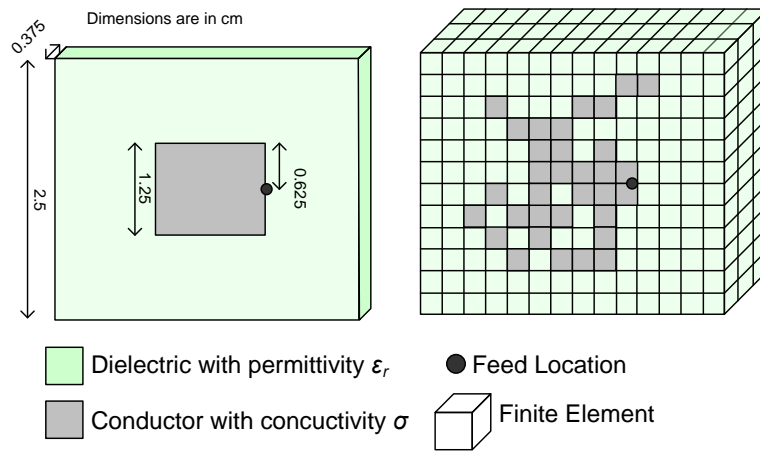
Figure 4.7 Patch antenna: a) with homogeneous substrate (left) b) with arbitrary metallization and dielectric distribution (right)

The training data set of the classifier belongs to the return loss response of the microstrip antenna. Genetic Algorithm is used in the optimization process and during the design process will call for multiple reanalysis of the full-wave bandwidth response of the large scale design problem. In order to accurately predict the return loss response used for calculating the fitness function represented by the bandwidth, a frequency sampling with 10 MHz intervals is needed. Figure 4.8 depicts the return loss curve of an arbitrary individual generated during a trial GA optimization process. The dashed line is a wrong prediction of the return loss curve that would lead to a wrong fitness value of the candidate individual because of insufficient sampling of the frequency range with 100 MHz intervals. The analysis tool used in generating simulated bandwidth response curves is a Finite Element Boundary Integral model based on a Fast Spectral Domain Algorithm, FSDA. It has been successfully validated in various radiation and scattering problems [3, 26]. The design process with simulations for 101 frequency points within the desired frequency range and N individuals of a micro-GA algorithm would call the

FSDA model $101 \times N$ times for each generation until the optimization algorithm converges. Hence, the computational time to reach convergence is likely to correspond to impractical timespans.
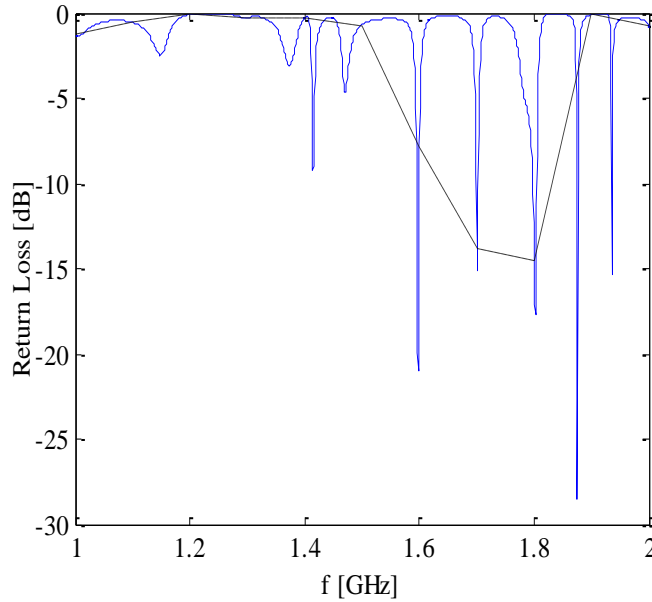
Figure 4.8 Simulated return loss response of a microstrip patch antenna with multiple sharp resonances in a [1 2] GHz working frequency range linearly interpolated with 1001 (solid) and 11 uniform samplings (dashed)

The proposed Bayesian based rational fitting scheme is integrated to the full wave simulator in order to interpolate the return loss response over a 1- 2 GHz frequency range for each design candidate. The optimization process is performed based on return loss analysis using the proposed Bayesian based rational interpolation with either a frequency sweep of 50 MHz or the semi-adaptive scheme using the 'bisect' classifier. The results of the interpolation scheme employed within the design process are presented in the next section.

4.3 **Results**

The resulting rational interpolation response relies on the use of first order derivative values at sampled data points. These are computed numerically with 1% variable perturbation via forward finite differences. Alternatively, they can be computed

analytically via the adjoint method [90] to reduce the computation time further. To isolate the effect of gradient calculations on the computational savings via interpolations, Bayesian based interpolation results are compared with both naïve linear interpolation and linear interpolation using double number of sample data. Former case is equivalent to the computational time savings if the adjoint variable method was used and the latter is representative for the case of forward differencing. The error norm for comparing resulting fittings in terms of their accuracy is chosen as the standard root mean square between interpolated and original return loss values. Original curves correspond to linear interpolations with a frequency sampling interval of 1 MHz with a total of 1001 sample points in the working frequency range of 1-2 GHz. A total of 220 intervals with known boundary conditions and interval lengths belong to return loss curves of 22 different design candidates that were used to train the Bayesian classifier and predict the optimum parameter *coef* of the fitted curves. The accuracy of the three interpolation schemes are compared in Figure 4.9 indicating an overall error increase of the proposed interpolation by 14% over the double sampled linear fitting and an increase by 1% when compared with naïve linear interpolation. However, despite the seemingly poor performance of the Bayesian based interpolation, better matched poles and hence qualitatively better approximated responses are observed for that fitting scheme calling for a reinvestigation of the chosen error norm. In fact, a more appropriate error measure to predict occurrence of poles and the actual bandwidth response of various designs would be the bandwidth measure itself. Hence, the error norm is re-defined as a bandwidth (GHz) based measure which also takes directly matched pole occurrence into account in the original and fitted responses. The differences between bandwidths are summed over the entire frequency range of $[1\ 2]$GHz to calculate the overall error. The results obtained based on the updated error norm are shown in Figure 4.10 and indicate an overall error decrease by 25% and 54% for Bayesian based rational fitting results when compared with double sampled and naïve linear fittings, respectively. This is a significant improvement in favor of the Bayesian fitting according to the new error norm. Figure 4.11 compares the root mean square error norms of the approximated responses belonging to the 11 design cases with respect to linear interpolation, linear interpolation with double sampling, and the semi-adaptive Bayesian based rational interpolation scheme.
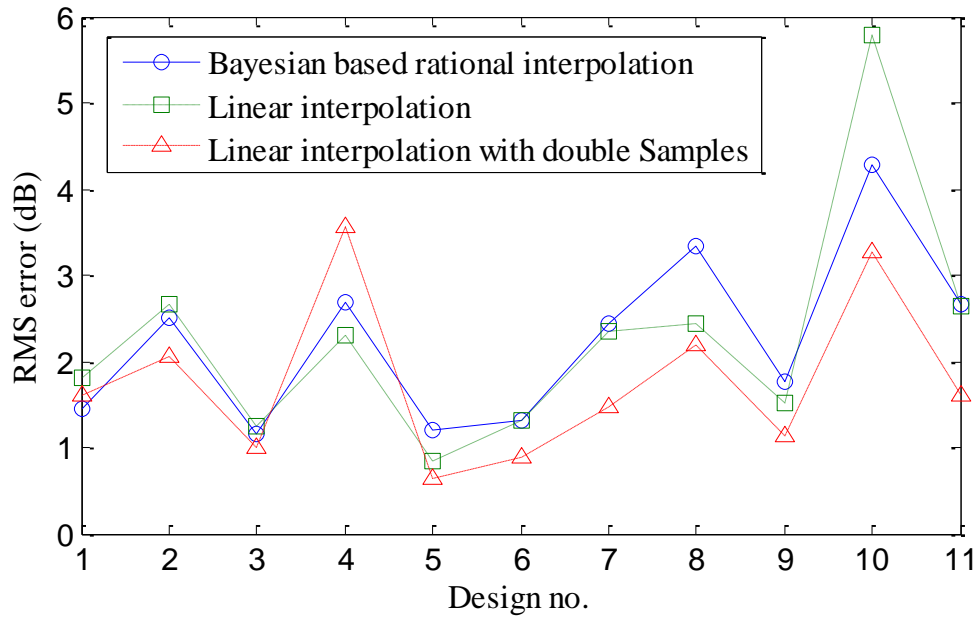
Figure 4.9 Interpolation error (square of return loss data difference) of Bayesian based and linear interpolations for 11 different designs
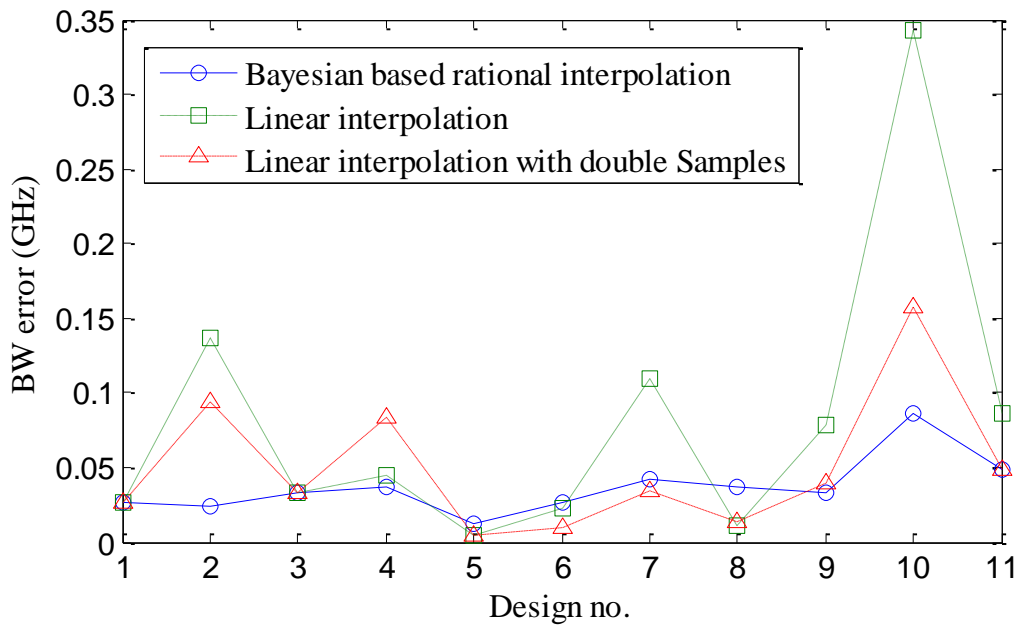
Figure 4.10 Interpolation error (bandwidth difference) of Bayesian based and linear interpolations for 11 different designs

Based on these results, the Bayesian based fittings show a further improvement via use of the 'bisect' classifier by decreasing the root mean square error norm by 28% and 14.5% when compared with the naïve linear and double sampled linear

interpolation, respectively. Despite the existence of rare cases where the Bayesian based fitting is very close to the accuracy performance of the linear interpolation (such as in designs 2, 4 and 5), there is another robustness aspect of this fitting scheme where it outperforms standard linear interpolation schemes and needs to be considered in addition to its overall accuracy advantage. Design cases with relatively larger Bayesian based interpolation errors are re-examined and a representative interval is displayed in Figure 4.12. Although the center plot (Figure 4.12 (b)) is in favor of the double sampled linear interpolation, perturbation of sample data to the left (Figure 4.12 (a)) and to the right (Figure 4.12 (c)) reveals that linear interpolation (with double number of sample data in this case) is more viable to sampling data as opposed to the Bayesian based rational fitting that consistently predicts the pole and approximates the bandwidth with better accuracy. This behavior is observed for all other design cases and is a clear indication of the latter being more robust to uniformly sampled data than naïve linear interpolation.
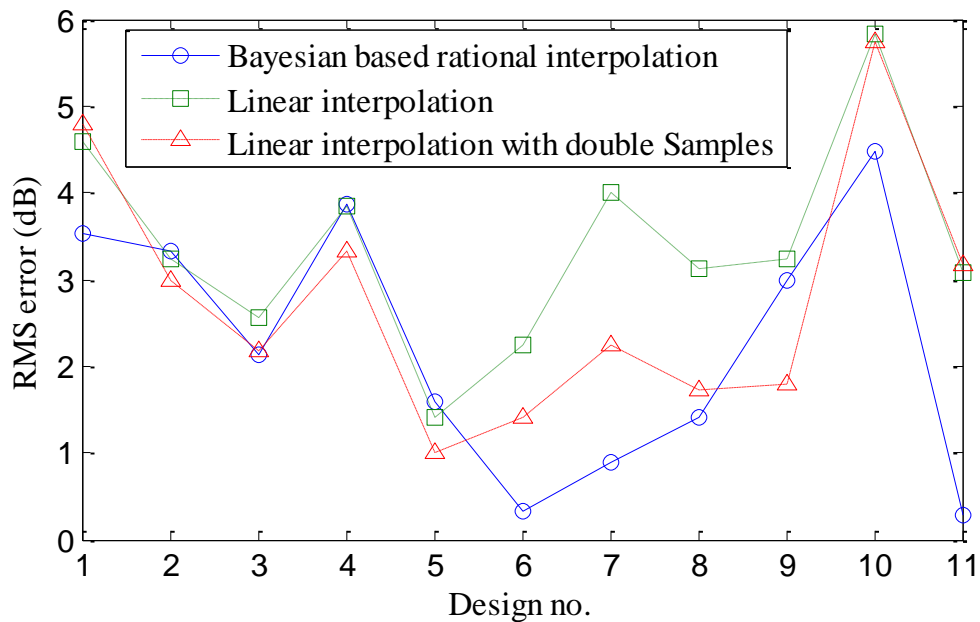
Figure 4.11 Interpolation error (bandwidth difference) of linear interpolations and Bayesian based interpolation integrated with semi-adaptive sampling using the 'bisect' classifier for 11 different designs.
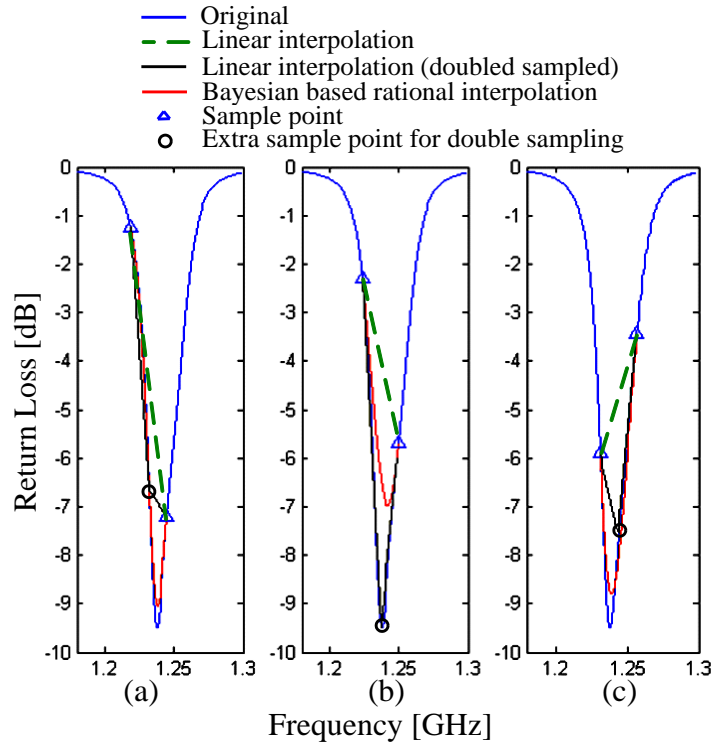
Figure 4.12 Effect of frequency sampling perturbation on rational interpolation (red) and linear interpolation (dashed green) and linear interpolation using double sampled data (black) with a) perturbation at interval [1.220 1.245] of the b) initial interval [1.224 1.249] and with c) perturbation at interval [1.300 1.325]

4.4 **Conclusion**

This chapter presented an interpolation scheme based on Bayesian trained quadratic rational functions for approximating frequency based electromagnetic return loss responses. Results indicate that this scheme is an efficient tool in predicting poles and characterizing resonance based behavior such as bandwidth of RF devices. Although the application of the proposed strategy with uniform sampling does not outperform naïve linear interpolations, when a standard root mean square error norm measure is used, it outperforms when a more reliable error norm associated with the direct response of the designs (here the bandwidth difference measurement is employed). It is also observed that when the proposed semi–adaptive sampling based on the 'bisect' classifier is integrated with the proposed Bayesian rational interpolation scheme, the results are highly enhanced for both error norm measurements. Future work includes application of the Bayes' theorem on higher order rational functions allowing for multi-resonance detections inside the interval of interest and its integration with a

fully adaptive sampling scheme. This would require additional work for preparing an ideal training set of adaptively sampled frequencies and interpolations of arbitrary order rational functions.

5 SPEED-UP TECHNIQUES BASED ON GENERALIZED STOER-BULIRSCH ALGORITHM WITH ADAPTIVE SAMPLING

As discussed in the previous chapter, global design optimization studies via heuristic search techniques relies on fast and accurate reanalysis with enhanced performance. In this chapter, another approximation scheme suitable for the frequency response of electromagnetic systems with multi-resonance behavior is investigated. The proposed technique allows for fast and accurate reanalysis within global electromagnetic design optimization studies.

Rational functions offer an attractive solution for providing a more global approximation taking into account the entire band of the frequency response into consideration when compared with standard interpolation techniques such as linear interpolation, higher order polynomials, cubic splines, etc. They also provide the advantage of well approximating resonances due to their inherent pole predicting behavior. Therefore, rational functions are likely to yield a more general approximation valid for a larger class of problems with a reduced computational effort and are more suitable to approximate frequency dependent electromagnetic responses. As a result, their use has resulted in various representations of resonance type curves with reasonable number of support points (points where the functional values are known) [106-112].

Solving for the coefficients of the rational function is known as the Cauchy method and is first introduced in [120]. The solution within a standard Cauchy based method with techniques such as direct inversion becomes more prone to numerical errors as the number of support points increases (by producing a system of linear equations which is ill-conditioned). A solution alternative to ill-conditioned systems is presented in [112]. The order of the optimum rational function is chosen such that the number of unknown coefficients is less than or equal to the rank of the corresponding stiffness matrix and hence the system to be solved becomes over-determined. Stiffness matrices are constructed via singular value decomposition and the total least squares method is employed to solve for the unknown coefficients. However, a frequency

response with multi-resonances cannot be approximated via the rank constrained strategy as the rank of the system limits the order of the rational model. In addition, each newly added point requires resolving the system and therefore the computational time becomes expensive when integrated with adaptive sampling techniques. An alternative approach to overcome these issues suitable for the solution of the unknown coefficients of a rational interpolation function is a recursive technique initially introduced by Stoer and Bulirsch [123] where the Neville approach is applied to rational functions.

Stoer-Bulirsch technique is a recursive method that adds one support point at a time and solves for the unique rational interpolator that passes through all existing support points. This recursive strategy in turn enhances its suitability to adaptive sampling techniques. When compared with direct inversion solutions of rational interpolations, Stoer-Bulirsch technique is significantly less prone to numerical errors and is not constrained by the rank of the system.

It is well known that adaptive sampling of a frequency response constitutes a key aspect in interpolation and therefore careful selection of sampling points should result in a more successful interpolation. Frequency data sets have been adaptively constructed and integrated to the proper choice of the rational function within Stoer-Bulirsch technique to establish a fast interpolation scheme. Specifically, in [109] two adaptive sampling algorithms for rational interpolation are proposed. Yan et al. [124] proposed an adaptive sampling through rational functions created by following alternative Neville paths based on diagonal paths representing *increments* of the numerator and denominator by one after a specific switching grid is chosen so that that part of the resulting path is parallel to the main diagonal one. The Stoer-Bulirsch interpolations are constructed based on a pre-determined standard diagonal path which is not optimized. Resulting interpolations can still be further improved for accuracy and computational efficiency exploiting another adaptive path.

In this chapter, we propose an approximation technique with an adaptive sampling scheme. The proposed technique is based on a developed generalized Neville algorithm which allows for an off-diagonal path as suggested in [125] in opposition to the conventional diagonal paths in standard Stoer-Bulirsch technique. However, since both the path followed to construct the interpolator and the samples selected directly affect the quality and computational cost of the interpolation process, an optimized route is expected to result in more reliable and cost effective interpolations. To address this

issue, the idea of a generalized Neville path is integrated here to an adaptive sampling strategy. Also, to further enhance the performance of an adaptive Neville path, the resulting algorithm is optimized for numerical stability. Results demonstrate the capability of the optimized method to overcome three common problems of existing methods: premature convergence, catching significant resonances and avoiding spurious oscillations. As a result, the proposed generalized Stoer-Bulirsch algorithm leads to approximations with reduced number of samples and enhanced accuracy norms.

This chapter is organized as follows: Background of the proposed generalized Stoer-Bulirsch algorithm along with numerical stability measures, initial diverse sampling, and adaptive sampling are presented in Section 5.1. Implementation of the proposed scheme to a design optimization problem is given in Section 5.2. The resulting generalized Stoer-Bulirsch algorithm is analyzed and compared with standard Stoer-Bulirsch technique and interpolation schemes with proposed enhancement features in Section 5.3. Discussions and conclusions follow in Section 5.4.

5.1 Background on Generalized Stoer-Bulirsch Technique with Adaptive Sampling

5.1.1 Solutions of rational function interpolations

Occurrence of nulls/poles in the frequency response of electromagnetic systems such as return loss, gain, and efficiency motivate the use of rational functions to approximate these quantities as explained in the previous chapter (see Section 4.1.1). In its general form, a rational function can be described via a fractional polynomial with a numerator of order N and a denominator of order D as

$$\Phi(x) = \frac{a_0 + a_1 x + a_2 x^2 + \cdots}{1 + b_1 x + b_2 x^2 + \cdots} = \frac{a_0 + \sum_{n=1}^{N} a_n x^n}{1 + \sum_{d=1}^{D} b_d x^d} \tag{5.1}$$

The Cauchy method deals with approximating a function by a ratio of two polynomials given by (5.1). Given the values of the function and its derivatives at a few points, the order of the polynomials and their coefficients are evaluated. Once the

coefficients of the two polynomials are known, they can be used to generate the parameter over the entire band of interest.

The solution of coefficients $\left(a_0 \cdots a_N\right)$ and $\left(b_1 \cdots b_N\right)$ of a frequency response function in the above form (5.1), requires $k = N + D + 1$ boundary conditions in the form of function values and/or their derivatives.

Various solution techniques such as direct inversion and total least squares as reviewed in the introduction can be used to solve the resulting linear system of equations. In order to overcome problems such as ill-conditioning for highly nonlinear or large systems associated with these methods, in this thesis, as a second interpolation scheme, an alternative technique that efficiently interpolates frequency response data with reduced number of points and increased accuracy is proposed. This scheme is based on Stoer-Bulirsch algorithm relying on a Neville path that in its most general form is not diagonal as explained in the next section.

5.1.2 Generalized Stoer-Bulirsch technique

Stoer and Bulirsch extended the recursive Neville algorithm (for interpolation using polynomials) to rational functions. Let $\left(x_i, f_i\right)$ denote the ith support point and $\Phi_s^{\mu,\nu}(x) = P_s^{\mu,\nu}(x)/Q_s^{\mu,\nu}(x)$ define a rational function with $\Phi_s^{\mu,\nu}(x_i) = f_i$ for $i = s, s+1, s+2, \cdots, s+\mu+\nu$ where $P_s^{\mu,\nu}(x)$ and $Q_s^{\mu,\nu}(x)$ are polynomials of degrees not exceeding μ and ν, respectively. Stoer-Bulirsch algorithm is used recursively to generate rational interpolators for $\mu \geq 1$ and $\nu \geq 1$ according to the following formulas

$$\Phi_s^{\mu,\nu}(x) = \Phi_{s+1}^{\mu,\nu-1}(x) + \frac{\Phi_{s+1}^{\mu,\nu-1}(x) - \Phi_s^{\mu,\nu-1}(x)}{\dfrac{\alpha_s}{\alpha_{s+\mu+\nu}}\left[1 - \dfrac{\Phi_{s+1}^{\mu,\nu-1}(x) - \Phi_s^{\mu,\nu-1}(x)}{\Phi_{s+1}^{\mu,\nu-1}(x) - \Phi_{s+1}^{\mu-1,\nu-1}(x)}\right]} \tag{5.2}$$

$$\Phi_s^{\mu,\nu}(x) = \Phi_{s+1}^{\mu-1,\nu}(x) + \frac{\Phi_{s+1}^{\mu-1,\nu}(x) - \Phi_s^{\mu-1,\nu}(x)}{\dfrac{\alpha_s}{\alpha_{s+\mu+\nu}}\left[1 - \dfrac{\Phi_{s+1}^{\mu-1,\nu}(x) - \Phi_s^{\mu-1,\nu}(x)}{\Phi_{s+1}^{\mu-1,\nu}(x) - \Phi_{s+1}^{\mu-1,\nu-1}(x)}\right]} \tag{5.3}$$

where $\alpha_i = x - x_i$ For details and derivation the reader is referred to [123].

Following a pre-determined diagonal path in the recursion (Known as the Neville path) as shown in Figure 5.1, calculation of successive interpolators, $\Phi_s^{\mu,v}$, required for each newly added support point becomes straightforward as shown by diagonal branches of the interpolator construction tree in Figure 5.2. As an example, consider the addition of the third support point; the algorithm starts by calculating the function $\Phi_3^{0,1}$ using (5.3) (interpolator of order 0,1 passing through the third support point), followed by $\Phi_2^{1,1}$ using (5.2) (order 1,1 passing through support points 2 and 3), and finally $\Phi_1^{1,2}$ using (5.3) (order 1,2 passing through the support points 1, 2, and 3) as demonstrated graphically in Figure 5.2. Newly constructed interpolators at the third level, $\Phi_3^{0,1}$ and $\Phi_2^{1,1}$, in addition to interpolators at lower levels are available for the calculation of the last interpolator $\Phi_1^{1,2}$ as a result of following the diagonal Neville path. However, if the interpolators are formed following a non-diagonal path, (e.g. dashed line in Figure 5.1), the calculation of the final rational function becomes a difficult task since necessary interpolators are not available. More specifically, based on the recursive scheme as suggested by formulas (5.2) and (5.3), additional intermediate interpolators, '*intermediates*'[1], are needed which can be evaluated recursively via the use of old support points. It is noted that these intermediates also depend on how far the path is from the diagonal.
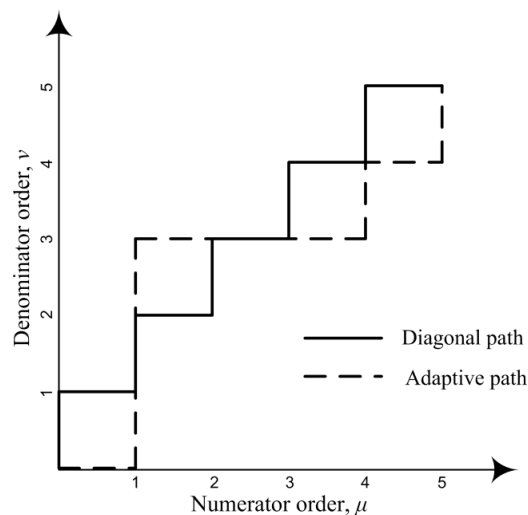
Figure 5.1 Neville path used in constructing a rational function of order $\mu = 5$ and $v = 5$ following diagonal (solid) and non-diagonal (dashed) paths

---

[1] In this context intermediates refer to any interpolator that is different from the final interpolator $\Phi_1^{M,N}$
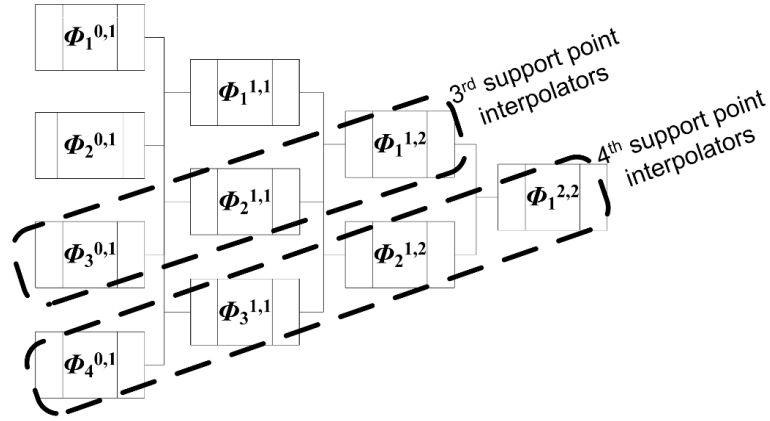
Figure 5.2 Construction tree for interpolators $\Phi_s^{\mu,\nu}$ based on diagonal Neville path algorithm; each branch corresponds to a newly added support point.

Once Stoer-Bulirsch technique attains an interpolator with order M, N with $k = M + N + 1$ sample points depending on a certain error criterion, the new direction is chosen as either $(M + 1, N)$ or $(M, N + 1)$. Consequently, a new sample point is added and the recursive iteration of the newly added point continues. Starting with $s = M + N + 2$, $\mu = 0$ and $\nu = 0$ the adaptive path is calculated until the following criteria are met $s = 1$, $\mu = M$ and $\nu = N + 1$, or alternatively $s = 1, \mu = M + 1$ and $\nu = N$. It is noted that according to recursive algorithm stated by (5.2) and (5.3), the calculation of the last interpolation function $\Phi_1^{M+1,N}(x)$ or $\Phi_1^{M,N+1}(x)$ requires all intermediate interpolation functions such as $\Phi_1^{M,N}(x)$, $\Phi_2^{M,N}(x)$, and ($\Phi_2^{M,N-1}(x)$ or $\Phi_2^{M-1,N}(x)$) to be known a priori. Regardless of the path, $\Phi_1^{M,N}$ and $\Phi_2^{M,N}$ are always available but $\Phi_2^{M,N-1}$ and/or $\Phi_2^{M-1,N}$ are in general not available unless a diagonal path is followed. The path norm r used in determining these intermediates is equal to

$$r = \max(\mu, \nu) - \min(\mu, \nu) \tag{5.4}$$

The missing intermediates are evaluated at the recursive iteration level $s = M + N + 1$ by evaluating the terms $\Phi_2^{M,N-1}$, $\Phi_3^{M,N-2}$, $\cdots$, $\Phi_r^{M,N-r+1}$ using (5.3) if $\Phi_2^{M,N-1}$ is part of the adaptive path or evaluating $\Phi_2^{M-1,N}$, $\Phi_3^{M-2,N}$, $\cdots$, $\Phi_r^{M-r+1,N}$ using (5.2) if $\Phi_2^{M-1,N}$ is on the adaptive path. The intermediates calculated are shown

graphically in Figure 5.3 for the special case of $r = 2$. In addition to being computationally costly and more complicated, following such an arbitrary trajectory of the Neville path leads to numerical difficulties not encountered when a conventional diagonal path is followed. Next section deals with proposed remedies to overcome these numerical instabilities.
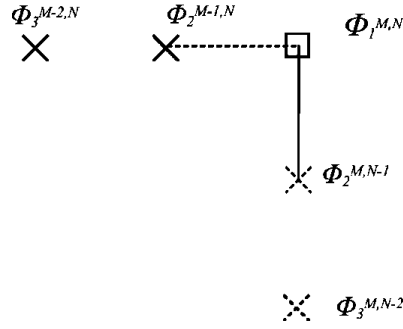
Figure 5.3 Representative interpolators and orders necessary for following alternative paths with path norm $r = 2$. Paths to be followed are associated with points and corresponding interpolators with the same type (dashed or solid)

5.1.3 Numerical stability issues

To avoid numerical instability problems during movement along the horizontal axis μ at $\nu = 0$ (increase of numerator order) or along the vertical axis ν at $\mu = 0$ (increase of denominator order), pure polynomial Neville's approach is employed, instead of constructing interpolators using (5.2) and (5.3), with support points (x_i, f_i) and $(x_i, 1/f_i)$ along the μ and ν directions, respectively. Here, interpolators are constructed according to the following formulas

$$\Phi_s^{0,0}(x) = f_s$$

$$\Phi_s^{\mu,0}(x) = \frac{\alpha_s \Phi_{s+1}^{\mu-1,0}(x) - \alpha_{s+\mu} \Phi_{s+1}^{\mu-1,0}(x)}{\alpha_s - \alpha_{s+\mu}} \quad \mu = 1,2,\cdots \tag{5.5}$$

$$\Phi_s^{0,0}(x) = f_s$$

$$\Phi_s^{0,\nu}(x) = \frac{\alpha_s - \alpha_{s+\nu}}{\alpha_s / \Phi_{s+1}^{0,\nu-1}(x) - \alpha_{s+\nu} / \Phi_s^{0,\nu-1}(x)} \quad \nu = 1,2,\cdots \tag{5.6}$$

Also, measures are taken to overcome a second instability that arises during the calculation of the intermediates with a comparatively high order numerator and low order denominator (e.g. for $\mu = 8$ and $\nu = 2$). This type of instability is a result of an effort to fit pure polynomials with high order differences to responses in regions that contain significant resonances. In essence, polynomials are virtually forced to pass through sharp resonances, i.e. interpolate through abrupt functional value changes. This leads to loss of accuracy in the form of significant digits when high and low intermediates are being subtracted in (5.2) and (5.3). Therefore, instead of following an adaptive path throughout for calculating intermediates, a diagonal path is followed until the minimum value of numerator or denominator order is attained followed by a horizontal or vertical line movement to the final desired interpolator. The proposed stable alternative path for calculating intermediates and the adaptive path used for sampling are shown in Figure 5.4.
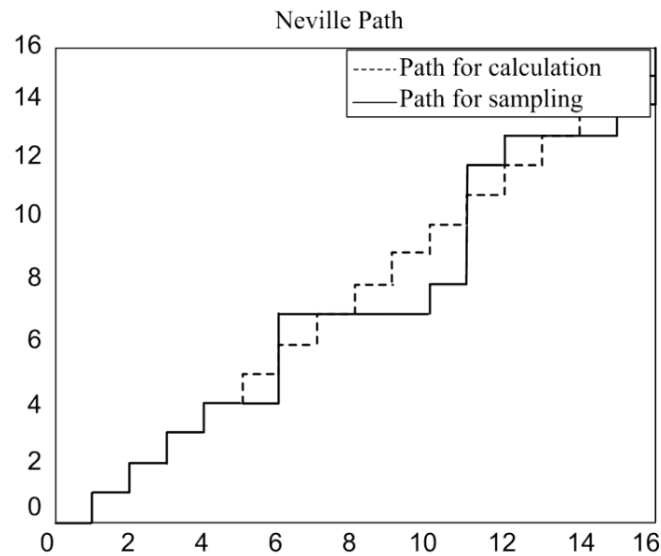
Figure 5.4 Path used for sampling (solid) and for calculating stable intermediates (dashed)

In the following two sections we discuss an adaptive sampling technique using the generalized Stoer-Bulirsch technique to improve the performance of the approximation scheme further.

5.1.4 Initialization with diverse sampling

In this section we introduce the sampling property of the proposed scheme, namely the initial diverse sampling algorithm. The algorithm basically divides the frequency domain into sub-regions based on information related to occurrence of pronounced resonances such that each resonance is confined in one region as shown in Figure 5.5. Diverse sampling is achieved by using pure polynomial interpolations (observed to spread the sampling points) until convergence based on a chosen error norm, ε_{Pol}, is satisfied.
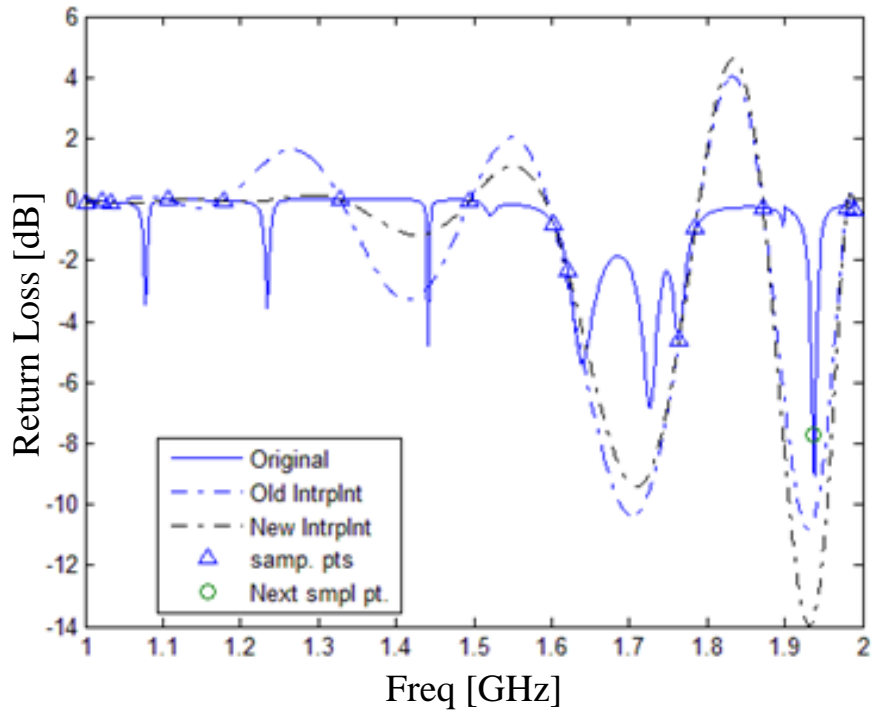
Figure 5.5 Diverse sampling based on pure polynomial interpolation used in initial sampling

The flowchart, shown in Figure 5.6, demonstrates this initialization procedure with diverse sampling. Here, the normalized error norm of two successive interpolators $\phi(x)$ and $\phi'(x)$ is defined as

$$e_1 = \frac{\sum_x |\phi'(x) - \phi(x)|}{\max(\phi'(x)) - \min(\phi(x))} \tag{5.7}$$

where $\phi'(x) = \begin{cases} \phi_1^{M+1,N}(x) \\ \phi_1^{M,N+1}(x) \end{cases}$ and $\phi(x) = \phi_1^{M,N}(x)$, M and N being the numerator and the denominator order, respectively. Here, the iteration number or the number of support points K is $M + N + 1$;
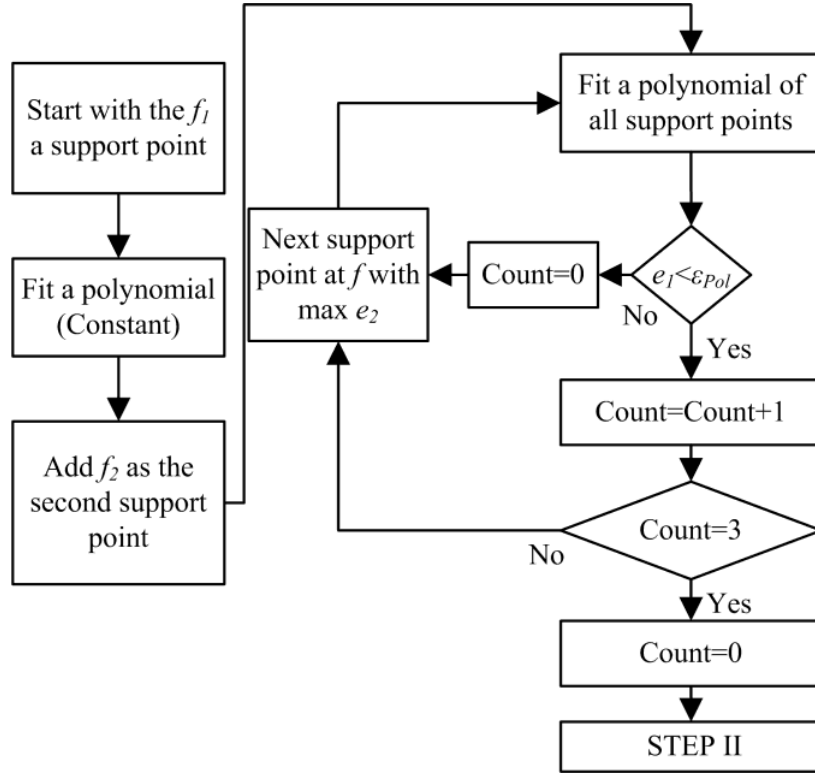
Figure 5.6 Step I: Initial diverse sampling algorithm

Also, the next support point is selected to be the argument that maximizes the second error norm e_2 as follows

$$\underset{x}{\mathrm{argmax}} \left[e_2\right] \tag{5.8}$$

where $e_2 = |\phi'(x) - \phi(x)|$.

The algorithm starts with pure polynomial interpolation until the error norm e_1 drops below a certain threshold ε_{Pol}, that ensures diversity of initial support points.

5.1.5 Adaptive sampling with generalized Neville path

The generalized interpolation algorithm that accounts for the non-diagonal Neville path was introduced in the beginning of Section 5.1. Having established the diverse sampling scheme, this section focuses on a novel technique for integrating frequency adaptive sampling to the generalized Stoer-Bulirsch algorithm. It is noted that once a resonance is correctly interpolated, the proposed method aims to drive the search towards sample data in regions which are likely to exhibit a new resonance.
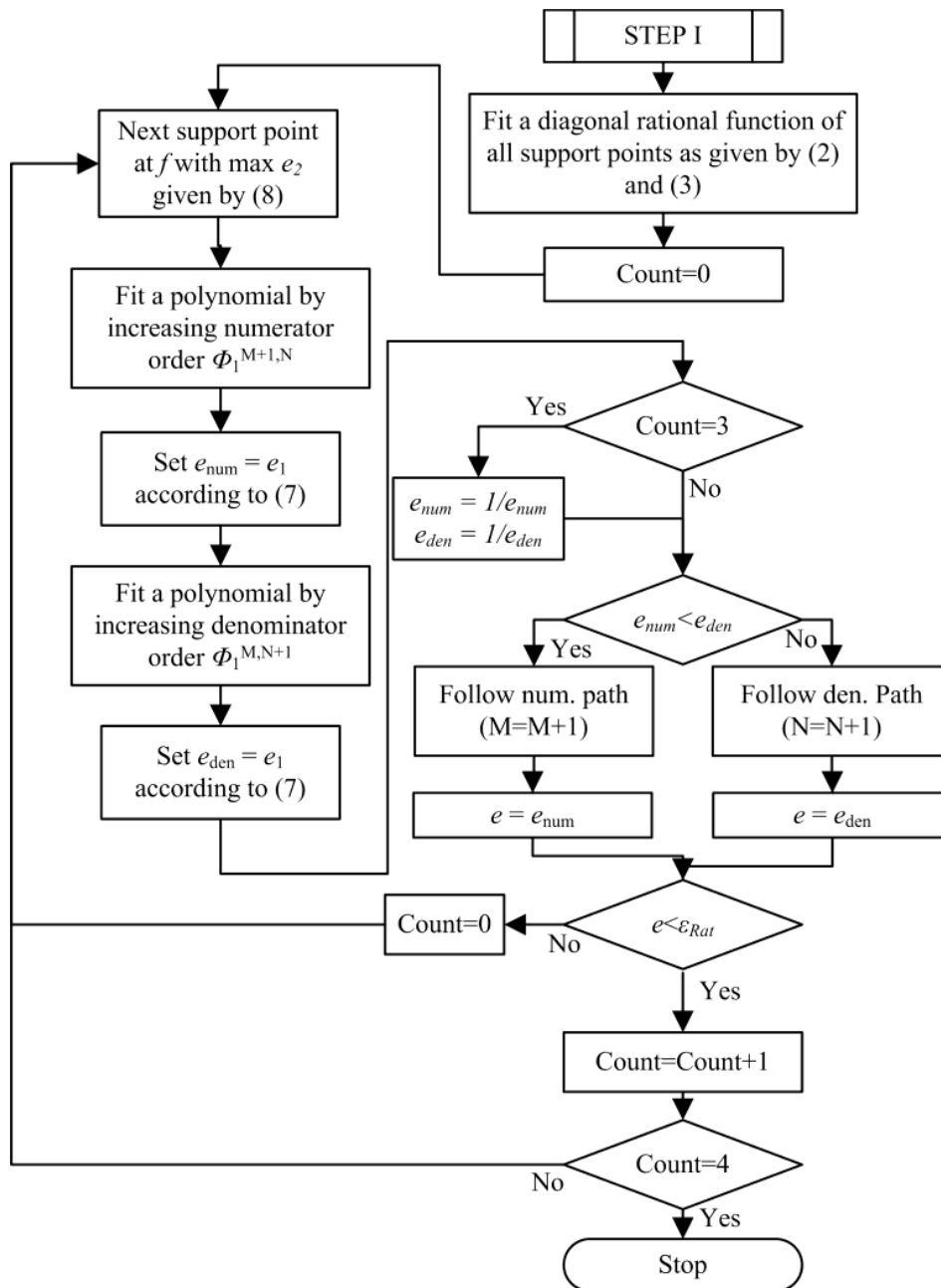
Figure 5.7 Step II: Adaptive sampling with generalized Neville path

The flowchart of the generalized Stoer-Bulirsch technique is shown in Figure 5.7. The algorithm starts with step II by constructing interpolations with previously found support points by following a diagonal path of the Stoer-Bulirsch technique. A diagonal path simply corresponds to a rational function the numerator order of which is equal to the denominator order or one less (first block of step II in Figure 5.7). The next sampling point, as in Step I, is selected according to (5.8). There are two alternative rational functions to be continued with along the non-diagonal Neville path. More specifically, the error norms e_1 given by (5.7) of two rational functions ϕ' of order $(M+1, N)$ and $(M, N+1)$ passing through $K = M + N + 2$ points are compared against each other. The choice determines the next branch of the adaptive path. Interpolation trials suggest that following a path that minimizes the error norm, e_1, between successive interpolators has the effect of decreasing the computational time required to obtain the final interpolation function with the convergence criterion $e_1 \prec \varepsilon_{Rat}$ successively occurring 3 times. Nevertheless, this fast convergence may turn out to be local, in terms of predicting a specific region possibly encapsulating a resonance, causing additional resonances of the overall response to be left out in the final interpolation. On the contrary, following a maximum error path enforces sampling at out-of-local regions that potentially possess resonances. Therefore, a hybrid method is expected to effectively capture maximum number of resonances by allowing for jumps between regions based on the maximum error path once a local convergence based on the minimum error path is reached. This procedure is repeated until the convergence criterion, $e_1 \prec \varepsilon_{Rat}$, successively occurs 4 times.

5.2 Example Application of Interpolation Scheme

The proposed Stoer Burlisch algorithm with adaptive sampling is tested on return loss responses of various representative complex conductor topologies supported by heterogeneous material substrates. Since these are highly likely to produce complex multi-resonance curves during design iterations, speed-up techniques play a critical role to achieve formal design studies within practical timespan. One such design candidate in a topology optimization problem of a broad band patch antenna is shown in Figure

5.8. The goal of the design problem is to improve the bandwidth of an initially unmatched antenna structure via changing the material and conductor distribution. Each substrate layer of the patch antenna is discretized into (20×20) 400 design cells or 800 finite triangular prism elements. Each cell's relative permittivity can range from 0 to 100 and is represented by a design variable in a different color. Also, the radiating conductor's topology varies via the on or off (conductor or no conductor) nature of design cells. Consequently, another 400 cells constitute design variables which are on or off to search for the optimal topology of the conductor. Therefore, total number of design variables N can be evaluated via 400 x number of layers +400 turning the design problem into a large scale one that could be solved using a micro-genetic algorithm (typically running for 100 generations with an average population of 40 individuals).

Computational time for a single layer geometry using a full wave finite element analysis such as the fast spectral domain algorithm [28] and standard linear interpolation through 101 uniformly distributed frequency points within 1-2 GHz corresponds to approximately 1 week. More specifically, the required computational time can be calculated as follows:

$$\# \text{Iterations} \times \# \text{support points} \times \text{iteration time} = (101 \times 40)\text{iteration} \times 100\,\text{supp point} \times$$
$$3\,\text{s}/(\text{iteration} \times \text{supp.point} \times \#\text{layer}) \times \#\text{layers} \approx 12000s \approx 1\,\text{week}/\text{layer}$$
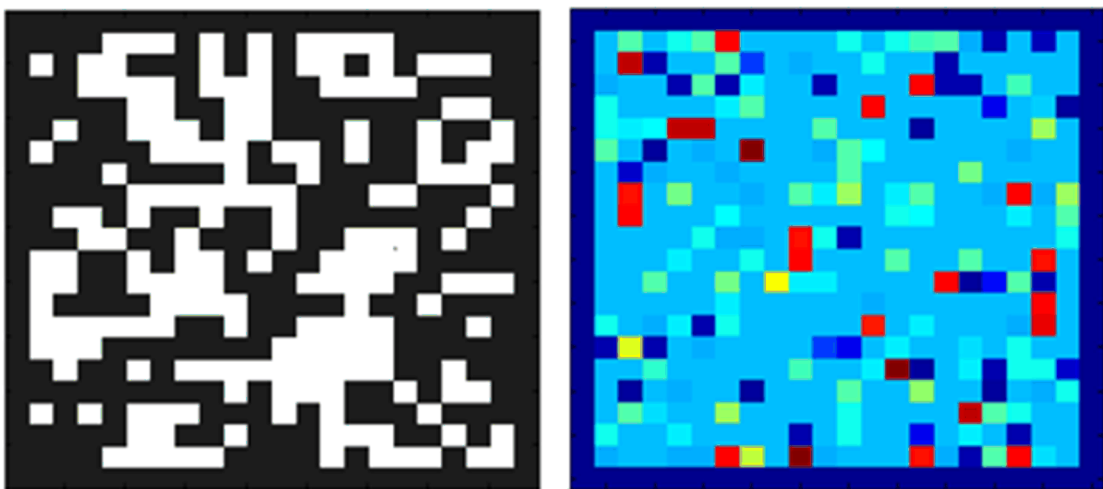
Figure 5.8 Conductor patch (white) distribution (left) on substrate with heterogeneous material composition where ε ranges from 0-100 (right).

The computational time of the design process becomes prohibitively long as the number of layers increases. In the next section, results of variations in the interpolation scheme based on Stoer-Bulirsch technique developed in this thesis are presented.

5.3 **Results**

In this section we will present and compare results of five different interpolation techniques that are combinations of features such as numerical instability measures, initial diverse sampling strategy, and adaptive sampling with generalized Neville path as proposed and introduced in Section 5.1. Their short descriptions are given below.

M1: Stoer-Bulirsch technique: Standard Stoer-Bulirsch Algorithm with diagonal Neville path is implemented.

M2: Stoer-Bulirsch technique with diverse sampling: An initializing diverse sampling criterion (see Section 5.1.4) is integrated with standard Stoer-Bulirsch technique (employing diagonal Neville path). Convergence criterion is defined as the condition $e_1 \prec \varepsilon_{Pol} = 100$ to be met two times successively. The conventional diagonal path is followed until $e_1 \prec \varepsilon_{Rat} = 4$ is met 3 times successively. The error norm e_1 is given in (5.7).

M3: Generalized Neville path with diverse sampling: The adaptive sampling according to the generalized Neville path suggested in Section 5.1.5 is integrated with diverse sampling strategy in Section 5.1.4. The error tolerance of the diverse sampling and generalized Stoer-Bulirsch technique are $\varepsilon_{Pol} = 100$ and $\varepsilon_{Rat} = 4$, respectively. Stopping criterion of the generalized Stoer-Bulirsch technique is explained in Section 5.1.5.

M4: Generalized Neville path with diverse sampling and numerical instability measures: Same as in 3 with equations (5.5) and (5.6) used for calculating polynomials with zero order numerator and denominator. Diagonal path is followed for calculating intermediates whenever possible (Details are given in Section 5.1.3).

M5: Generalized Neville path and numerical instability measures: Same as in M4 with no diverse sampling.

Table 5.1 summarizes the five interpolation strategies.

Table 5.1 Interpolation techniques based on strategies in Section 5.3 of the proposed generalized Stoer-Bulirsch algorithm

	Diverse Sampling	Standard Stoer-Bulirsch technique	Generalized Neville path	Numerical Stability
M1		*		
M2	*	*		
M3	*		*	
M4	*		*	*
M5			*	*

All five strategies were used to construct interpolations to approximate the return loss response of antennas with various material and conductor topologies. Results are shown in Figure 5.9-Figure 5.13. Each interpolation curve is compared to the original response which is numerically calculated using a fine sampling rate of 1 MHz, i.e. 1001 uniformly distributed frequency points are sampled between 1-2 GHz. Since finer sampling does not improve the response further, it can be accepted as the original antenna simulation response.

Our objective being to approximate return loss curves with similar accuracy but reduced number of support points to the original response, the proposed interpolations of return loss curves belonging to eleven different antenna design candidates were compared. These responses vary from smooth single resonance broad bandwidth curves to narrow multi-resonant responses. Figure 5.9-Figure 5.13 summarizes results for the five interpolation strategies in Table 5.1 with the same stopping criterion threshold of $\varepsilon_{Rat} = 4$. According to the results shown in Figure 5.9, when a standard diagonal path is followed, major resonances of the response could not be captured. Starting with a diverse sampling as proposed in method 2 allows of recovering the major first resonance as shown in Figure 5.10. However, this time, there is a shift in the narrower band resonance. Results adopting the proposed hybrid technique based on generalized Neville path plotted in Figure 5.11 show that all major resonances (< -2dB) are successfully captured. However, numerical instabilities in the form of oscillations are observed at the far end of the frequency based response. Upon adopting proposed numerical instability measures, the interpolation of method 4 yields a response as shown in Figure 5.12. Hence, all resonances are finally captured and auxiliary oscillations do not exist. To clearly assess the effect of the initial sampling scheme, interpolation scheme 4 is used without adapting the initial sampling scheme. Corresponding results plotted in Figure 5.13 prompt for an increase in the number of support points (from 33

to 44) with only ~0.1 dB improvement on the accuracy of the fitted curve. A full comparison of each interpolation method for eleven antenna design responses is conducted and quantified using the root mean square (RMS) error. Comparative results are given in Figure 5.14.
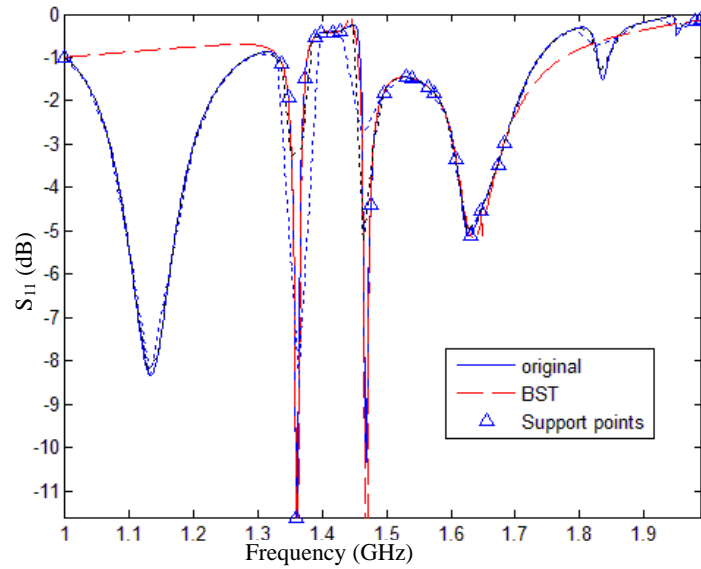
Figure 5.9 Interpolation scheme M1 in Table 5.1: Standard Stoer-Bulirsch technique
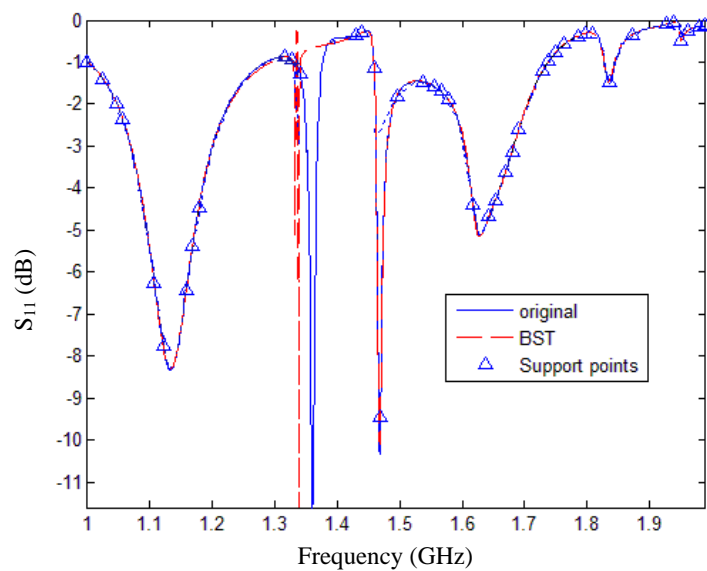
Figure 5.10 Interpolation scheme M2 in Table 5.1: Standard Stoer-Bulirsch technique with diverse sampling
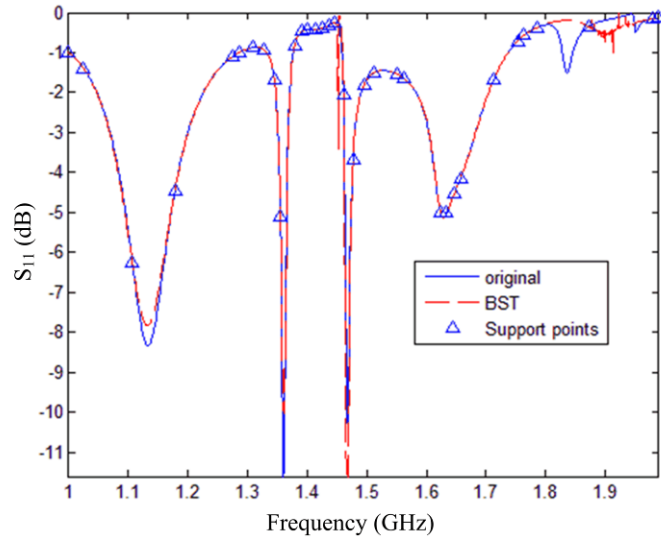
Figure 5.11 Interpolation scheme M3 in Table 5.1: Generalized Neville path with diverse sampling
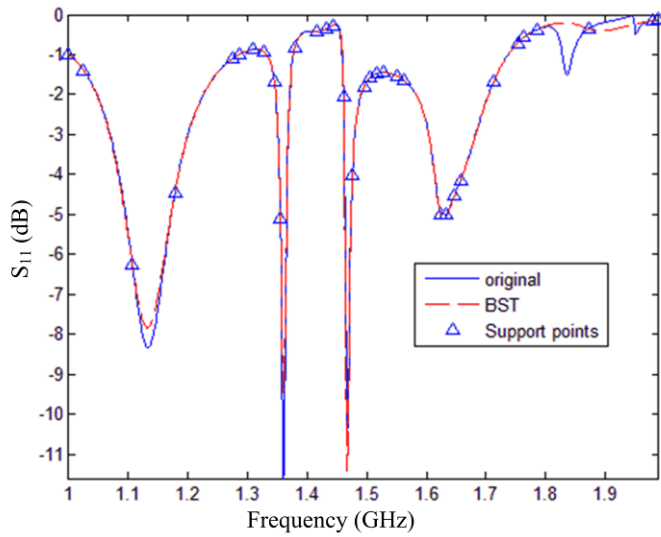
Figure 5.12 Interpolation scheme M4 in Table 5.1: Generalized Neville path with diverse sampling and numerical instability measures
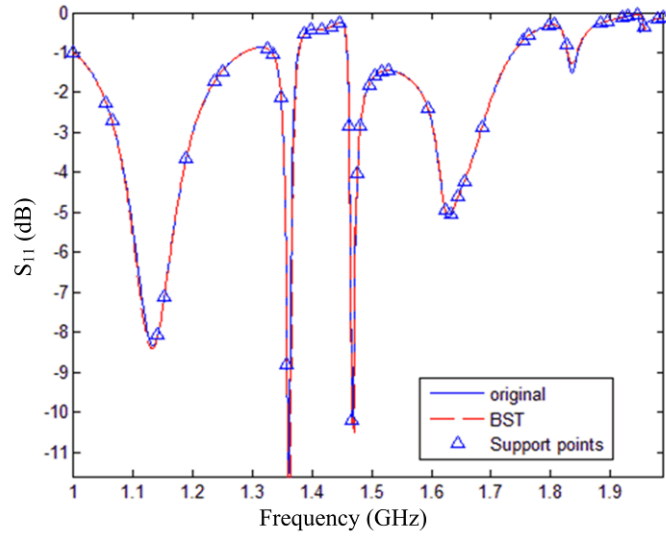
Figure 5.13 Interpolation scheme M5 in Table 5.1: Generalized Neville path with numerical instability measures (no diverse sampling)
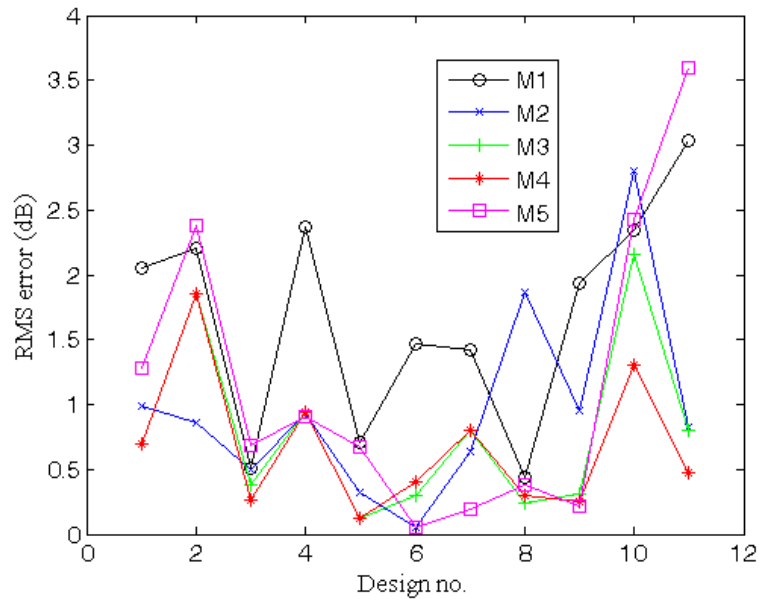
Figure 5.14 Accuracy (root mean square error) of schemes in Table 5.1 for eleven designs

Also, in order to compare each interpolation scheme's overall performance, the average sum of the RMS error of all eleven designs is plotted in Figure 5.15 using the 5 interpolation methods. Results show that the error in using the naïve diagonal Stoer-Bulirsch algorithm (method 1) has dropped by almost 54% when compared with the proposed numerically stable adaptive Stoer-Bulirsch interpolation scheme (method 4).
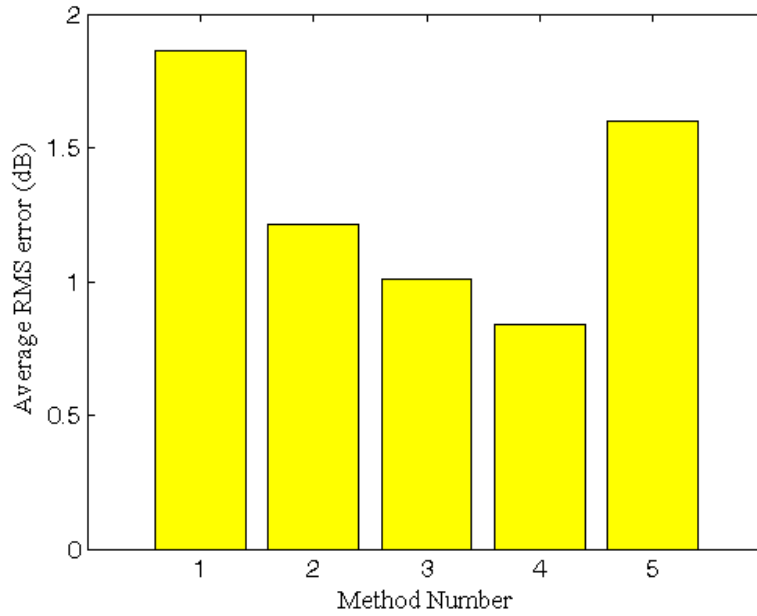
Figure 5.15 Average sum of the error square norm of 11 designs using 5 different
interpolation schemes in Table 5.1

An alternative measure, taking both computational time (number of support points) and accuracy (error norm) into account, refers to the product of the total number of support points with the total error as shown in Figure 5.16.
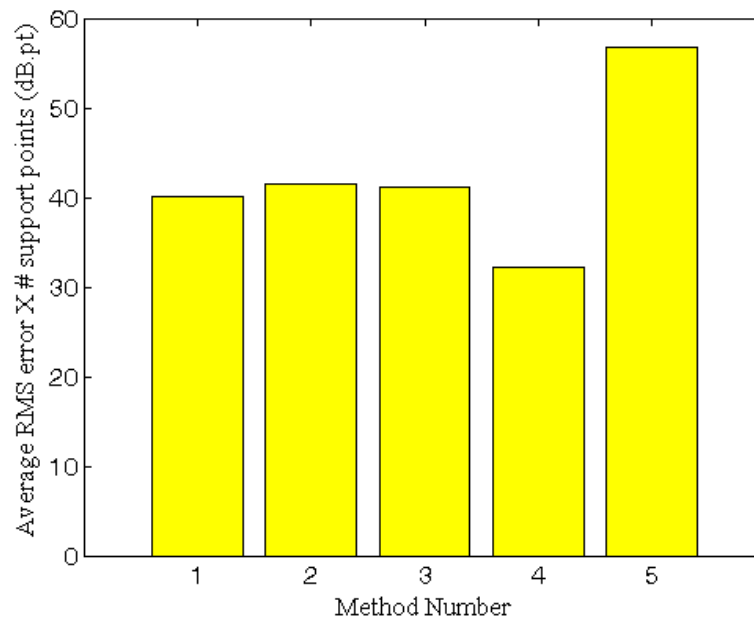
Figure 5.16 Product of the total number of support points with the average sum of the
error square norm vs. interpolation scheme number in Table 5.1

Results prove that the proposed interpolation scheme (method 4) is outperforming others with an overall improvement of 22.5% over the standard Stoer-Bulirsch scheme. In addition, the average total number of required support points has dropped from 89 to 39 points based on the same error norm that correspond to computational time savings of 56% when compared with conventional uniform linear interpolation schemes.

5.4 Discussion and Conclusion

In this chapter a generalized Stoer-Bulirsch approach for adaptively interpolating complex multi-resonant response curves with reduced number of support points and improved accuracy of existing methods was presented. The method relies on upgrading the standard Stoer-Bulirsch technique with a non-diagonal Neville path and makes use of this relaxation in shaping the best path that minimizes error and number of data samples needed. A hybrid technique following a path that minimizes the square error norm, e_1 given by (5.7), allowing for reduced number of support points followed by a path maximizing e_1 that enhances accuracy ensures a compromise between these conflicting merits and outperforms conventional adaptive sampling techniques. The proposed method has been implemented on return loss responses of various antennas with complex conductor shapes with heterogeneous material substrate configurations and resulted in an overall accuracy increase of 54% when compared with the naïve Stoer-Bulirsch interpolation technique. In addition, when compared with conventional uniform linear interpolation schemes, the average total number of required support points has dropped from 89 to 39 points based on the same error norm. This result indicates computational time savings of 56%. It is noted that the proposed technique is perfectly applicable to other electromagnetic response functions and versatile frequency response curves making it an ideal interpolation tool for large scale frequency response type optimization design problems. This is expected to open up new paths for large scale optimization studies of complex electromagnetic structures such as multi-physics responses of metamaterials based devices.

6 CONCLUSIONS AND FUTURE WORK

In this thesis the optimal topology optimization based on the theory of homogenization using asymptotic analysis was applied to the design of electromagnetic materials with desired dielectric constitutive matrices. Unlike other optimal design approaches that target electromagnetic device performance, the proposed tool is capable of designing the material or preferably 'metamaterials' directly by determining its microstructure which is the periodic building block or in formal terms the unit cell of the resulting desired overall structure. The design framework relies on three key modules: 1) Homogenized material model integrated to 2) an effective FEA based analysis framework and 3) a formal design optimization algorithm. The applicability of the resulting design framework is verified by designing materials with various desired isotropic and anisotropic permittivity tensors from available off-the-shelf isotropic constituents. Computational time of the proposed design framework which relies on a heuristic based optimization technique (genetic algorithm) can be effectively reduced in order to find the global optimum (that is usually unique and difficult to find by gradient based techniques without getting trapped in local minima) if the initial available shades are carefully chosen. Therefore, a bound analysis study was applied to the developed homogenized material model to check for feasibility of realizing the desired properties from available constituents before integrating it to the design framework. This bound study is based on a composition method and a statistical discretization approach and is applied on the effective dielectric tensors that are composed of two constituents. The method although restricted to two components can also provide a basis for qualitative feasibility estimations for more than two component materials as discussed in Sections 2.3 and 3.1.1.

The proposed design framework has the potential to open a new era of 'material design' by relaxing the standard device design optimization problem for various electromagnetic performances to a direct consideration of the materials themselves. The proposed framework was applied to an example in literature by designing anisotropic layers of non-reciprocal magnetic photonic crystals that allow for the propagation of electromagnetic waves in one direction only at a specific frequency where the unusual phenomenon of single inflection point takes place. This property has the advantage of

slowing down the group velocity and increasing the wave amplitude drastically allowing for higher Q and gain inside the crystal. What makes this single inflection point unique is that it allows this phenomenon to occur at a frequency far from the band edge and therefore enhances transmittance of waves at the interface of the crystal. The design of the layers for such an MPC is made in this thesis from commercially available ceramic powders with specific isotropic dielectric constants $\varepsilon \in \{20, 70, 140, 240\}$ in order to achieve anisotropic dielectric layers desired for the MPC with $\mathbf{\varepsilon}_{A_1} = \begin{bmatrix} 165 & 0 \\ 0 & 85 \end{bmatrix}$ and fully anisotropic $\mathbf{\varepsilon}_{A_2} = \begin{bmatrix} 159.64 & -20 \\ -20 & 90.36 \end{bmatrix}$ permittivity matrices. Although the design of the first tensor was easily obtained via the design framework because it simply is a diagonal material tensor, the second design with non-zero off diagonal elements did not converge to a solution until the resolution of the design domain was increased. The resolution is an important optimization parameter that determines both the convergence and the resulting microstructure. As it is increased the design convergence becomes more challenging as the originally ill-conditioned on-off problem turns into a more complicated design problem with an enlarged design space where the search takes place. As the design resolution is decreased, the design space may turn out be too narrow for the desired material tensor and the design problem may not be able to topologically find the optimum design. The proposed design framework was successfully implemented to the design of isotropic, anisotropic and fully anisotropic two dimensional electromagnetic constitutive tensors.

The rest of the thesis dealt with another way of effectively reducing the computational time of large scale design optimization problems especially for device performance problems associated with frequency based multi-resonant responses. To address this issue, in Chapter 4 a rational function of second order polynomials and a heuristic based inference method (Bayes theorem) was proposed. As an alternative, in chapter 5 a second method based on a generalized Stoer-Bulirsch algorithm with adaptive sampling was proposed.

Regarding the former, five parameters are in general needed to solve for unknown rational function of this type; four of which are determined by the boundary conditions of the subinterval to be interpolated and the fifth parameter is determined heuristically using the Bayesian classifier. The classifier is trained using a training set of subintervals

with known boundary conditions that determine four parameters and the fifth parameter is calculated optimally. An adaptive frequency sampling scheme was also proposed based on Bayesian theory again for the same boundary conditions. Several mathematical remedies were performed on the boundary conditions attributes in order to separate them as much as possible and enhance the classification procedure. Results indicate that this scheme is an efficient tool in predicting poles and characterizing resonance based behavior such as bandwidth of RF devices. This approach outperforms standard interpolation schemes based on a reliable error norm associated with the direct response of the designs, here the bandwidth difference measurement. It is also observed that when the semi–adaptive sampling is integrated with the proposed Bayesian rational interpolation scheme, the results are enhanced further.

Regarding the second interpolation scheme proposed in Chapter 5 it is based on a generalized Bulirsch-Stoer approach for adaptively interpolating complex multi-resonant response curves with reduced number of support points and higher accuracy. The method relies on upgrading the standard Stoer-Bulirsch technique with a non-diagonal Neville path and makes use of this relaxation in shaping the best path that minimizes error and number of data samples needed. A hybrid technique following a path that minimizes the square error norm, e_1 given by (5.7), allowing for reduced number of support points followed by a path maximizing e_1 that enhances accuracy ensures a compromise between these conflicting merits and outperforms conventional adaptive sampling techniques. The proposed method has been implemented on return loss responses of various complex antenna conductor shapes with heterogeneous material substrate configurations and resulted in an overall root mean square error reduction of 54% when compared with the naïve Stoer-Bulirsch interpolation technique. In addition, when compared with conventional uniform linear interpolation schemes, the average total number of required support points has dropped from 89 to 39 points based on the same error norm. This result indicates computational time savings of 56%. It is noted that the proposed technique is perfectly applicable to other electromagnetic response functions and versatile frequency response curves making it an ideal interpolation tool for large scale frequency response type optimization design problems. This is expected to open up new paths for large scale optimization studies of complex electromagnetic structures such as multi-physics responses of metamaterials based devices.

Contribution of the thesis can be summarized as follows

- Extension of topology optimization method based on the theory of homogenization and asymptotic analysis to the design of electromagnetic materials with desired constitutive parameters
- Design of materials with prescribed isotropic and anisotropic permittivity tensors from available off-the-shelf isotropic constituents
- Design of anisotropic dielectric layers for non-reciprocal magnetic photonic crystals
- Development of two rational interpolation schemes for frequency responses of large scale design studies
  - Bayesian based rational interpolation that infers a parameter controlling resonance detection and samples semi-adaptively.
  - Generalization of Stoer-Bulirsch algorithm with a non-diagonal Neville path to speed up convergence and effectively detect resonances

Future work related to the design methodology includes extending it to three dimensional structures by updating the analysis model in COMSOL Multiphysics-Coefficient Form module. The critical task is related to automatically defining the dirac delta function of the right hand side of (2.18) at the interface of the constituents which are surfaces in three dimensions. In addition, the model could be updated to account for frequency dependency in order to model left handed media. Another extension can be performed on the topology optimization framework by implementing the level set method or adaptive mesh method to yield smoother constituent topologies inside the unit cell. Nevertheless, fabrication of these materials needs to be considered during the design problem definition as realization of complex material distributions might still be restricted to dry powder deposition using grids as presented in Section 2.4.1.3. Also, the method of moment shows to be a valuable tool in image processing to define objects in three-dimensions and can be considered as good candidate to be integrated with topology optimization. In addition to these, the design methodology can be integrated to device performance studies where the optimum of the device could be linked to the design of the optimal electromagnetic material.

Regarding the first approximation technique, application of the Bayes' theorem on higher order rational functions allowing for multi-resonance detections inside the interval of interest and its integration with a fully adaptive sampling scheme are among

potential future work. This would require efforts to prepare an ideal training set of adaptively sampled frequencies and rational interpolations of arbitrary order.

In the second approximation scheme, the generalized Stoer-Bulirsch algorithm based on the non-diagonal Neville path can be extended to multi-dimensional independent variables. In addition, comparing it with vector fitting schemes can be considered in order to obtain an effective fitting convergence measure.

7 REFERENCES

[1]   J. Perruisseau-Carrier and A. K. Skrivervik, "Composite right/left-handed transmission line metamaterial phase shifters (MPS) in MMIC technology," *IEEE Transactions on Microwave Theory and Techniques*, vol. 54, pp. 1582-1589, 2006.

[2]   L. Ran, J. Huangfu, H. Chen, Y. Li, X. Zhang, K. Chen, and J. A. Kong, "Microwave solid-state left-handed material with a broad bandwidth and an ultralow loss," *Physical Review B (Condensed Matter and Materials Physics)*, vol. 70, pp. 073102-3, 2004.

[3]   G. Kiziltas, D. Psychoudakis, J. L. Volakis, and N. Kikuchi, "Topology design optimization of dielectric substrates for bandwidth improvement of a patch antenna," *IEEE Transactions on Antennas and Propagation*, vol. 51, pp. 2732-2743, 2003.

[4]   B.-I. Wu, W. Wang, J. Pacheco, X. Chen, T. M. Grzegorczyk, and J. A. Kong, "A Study of Using Metamaterials as Antenna Substrate to Enhance Gain," *Progress In Electromagnetics Research*, vol. 51, pp. 295-328, 2005.

[5]   J. L. Volakis, G. Mumcu, K. Sertel, C. C. Chen, M. Lee, B. Kramer, D. Psychoudakis, and G. Kiziltas, "Antenna Miniaturization Using Magnetic-Photonic and Degenerate Band-Edge Crystals," *Antennas and Propagation Magazine, IEEE*, vol. 48, pp. 12-28, 2006.

[6]   L. Sungjoon, C. Caloz, and T. Itoh, "Metamaterial-based electronically controlled transmission-line structure as a novel leaky-wave antenna with tunable radiation angle and beamwidth," *IEEE Transactions on Microwave Theory and Techniques*, vol. 52, pp. 2678-2690, 2004.

[7]   L. Sungjoon, C. Caloz, and T. Itoh, "Metamaterial-based electronically controlled transmission-line structure as a novel leaky-wave antenna with tunable radiation angle and beamwidth," *IEEE Transactions on Microwave Theory and Techniques*, vol. 53, pp. 161-173, 2005.

[8]   N. Fang, H. Lee, C. Sun, and X. Zhang, "Sub–Diffraction-Limited Optical Imaging with a Silver Superlens " *Science*, pp. 534-537, 2005.

[9]   O. S. M. David, J. B. Richard, and R. W. Conrad, "Submicron imaging with a planar silver lens," *Applied Physics Letters*, vol. 84, pp. 4403-4405, 2004.

[10]   A. K. Popov and S. A. Myslivets, "Transformable broad-band transparency and amplification in negative-index films," *Applied Physics Letters*, vol. 93, pp. 191117, 2008.

[11]   P. Baccarelli, P. Burghignoli, F. Frezza, A. Galli, P. Lampariello, G. Lovat, and S. Paulotto, "Effects of leaky-wave propagation in metamaterial grounded slabs excited by a dipole source," *Microwave Theory and Techniques, IEEE Transactions on*, vol. 53, pp. 32-44, 2005.

[12]   Y. Chen, K. Sin, H. Jiang, Y. Tang, K. Sasaki, A. Torabi, L. Wang, M. Park, D. Bai, Y. Shen, P. Luo, F. Liu, K. Stoev, W. Lin, and J. Zhu, "High Moment Materials and Fabrication Processes for Shielded Perpendicular Write Head Beyond 200 Gb/in^2," *IEEE Transactions on Magnetics*, vol. 43, pp. 609-614, 2007.

[13] K. Hongo and T. Watanabe, "Lensless surface plasmon head with 1 Tbit/in.(2) recording density," *Japanese Journal of Applied Physics*, vol. 47, pp. 6000-6006, 2008.

[14] J. B. Pendry, "Negative Refraction Makes a Perfect Lens," *Physical Review Letters*, vol. 85, pp. 3967-3969, 2000.

[15] X. Wang, D.-H. Kwon, D. H. Werner, and I.-C. Khoo, "Anisotropic Liquid Crystals for Tunable Optical Negative-Index Metamaterials," *IEEE Antennas and Propagation Society International Symposium*, San Diego, CA, 2008, pp.

[16] S.-W. Lee, Y. Kuga, and A. Ishimaru, "Quasistatic Analysis of Materials with Small Tunable Stacked Split Ring Resonators," *Progress In Electromagnetics Research*, vol. 51, pp. 219–229, 2005.

[17] I. Gil, J. Bonache, J. Garcia-Garcia, and F. Martin, "Tunable metamaterial transmission lines based on varactor-loaded split-ring resonators," *Microwave Theory and Techniques, IEEE Transactions on*, vol. 54, pp. 2665-2674, 2006.

[18] F. Bayatpur and K. Sarabandi, "A Tunable Metamaterial Frequency-Selective Surface With Variable Modes of Operation," *Microwave Theory and Techniques, IEEE Transactions on*, vol. 57, pp. 1433-1438, 2009.

[19] N. Wongkasemand, A. Akyurtlu, and K. A. Marx, "GROUP THEORY BASED DESIGN OF ISOTROPIC NEGATIVE REFRACTIVE INDEX METAMATERIALS," *Progress In Electromagnetics Research*, vol. 63, pp. 295–310, 2006.

[20] Z. Thomas, T. Grzegorczyk, B.-I. Wu, X. Chen, and J. A. Kong, "Design and measurement of a four-port device using metamaterials," *Optics Express*, vol. 13, pp. 4737-4744, 2005.

[21] J. M. F. M. F. M. R. Marqués, "A new 2D isotropic left-handed metamaterial design: Theory and experiment," *Microwave and Optical Technology Letters*, vol. 35, pp. 405-408, 2002.

[22] J. Shin, A. Akyurtlu, and M. Deshpande, "Comments on "Design, fabrication, and testing of double negative metamaterials"," *Antennas and Propagation, IEEE Transactions on*, vol. 53, pp. 891, 2005.

[23] D. L. Sounas, N. V. Kantartzis, and T. D. Tsiboukis, "Focusing Efficiency Analysis and Performance Optimization of Arbitrarily Sized DNG Metamaterial Slabs With Losses," *Microwave Theory and Techniques, IEEE Transactions on*, vol. 54, pp. 4111-4121, 2006.

[24] C. Caloz and T. Itoh. New York: Wiley, 2005.

[25] T. M. Grzegorczyk, C. D. Moss, L. Jie, C. Xudong, J. Pacheco, Jr., and K. Jin Au, "Properties of left-handed metamaterials: transmission, backward phase, negative refraction, and focusing," *Microwave Theory and Techniques, IEEE Transactions on*, vol. 53, pp. 2956-2967, 2005.

[26] Y. Erdemli, K. Sertel, G. R. A., D. E. Wright, and J. Volakis, "Frequency selective surfaces to enhance performance of broadband reconfigurable arrays," *IEEE Transactions on Antennas and Propagation*, vol. 50, pp. 1716-1724, 2002.

[27] T. F. Eibert, Y. E. Erdemli, and J. L. Volakis, "Hybrid finite element-fast spectral domain multilayer boundary integral modeling of doubly periodic structures," *IEEE Transactions on Antennas and Propagation*, vol. 51, pp. 2517-2520, 2003.

[28] T. F. Eibert and J. L. Volakis, "Fast spectral domain algorithm for hybrid finite element/boundary integral modelling of doubly periodic structures," *IEE Proceedings- Microwaves, Antennas and Propagation*, 2000, pp. 329-334.

[29] T. F. Eibert, Y. E. Erdemli, J. L. Volakis, T. Vaupel, and V. W. Hansen, "Frequency selective slot array analysis by hybrid finite element-boundary integral and spectral domain integral equation techniques," *Frequenz*, vol. 56, pp. 234-238, 2002.

[30] A. Bossavit, "Effective Penetration Depth in Spatially Periodic Grids: A Novel Approach to Homogenization," *EMC'94, International Symposium on Electromagnetic Compatibility*, Roma, Italy Dept. Elec. Engng., University La Sapienza, 1994, pp. 859-864.

[31] O. Ouchetto, S. Zouhdi, A. Bossavit, G. Griso, and B. Miara, "Modeling of 3-D periodic multiphase composites by homogenization," *Microwave Theory and Techniques, IEEE Transactions on*, vol. 54, pp. 2615-2619, 2006.

[32] O. Ouchetto, S. Zouhdi, A. Bossavit, G. Griso, and B. Miara, "Effective constitutive parameters of periodic composites," 2005, pp. 2 pp.

[33] O. Ouchetto, S. Zouhdi, A. Bossavit, G. Griso, B. Miara, and A. Razek, "A new approach for the homogenization of 3D metallo-dielectric lattices: the periodic unfolding method," in *PECS-VI: International Symposium on Photonic and Electromagnetic Crystal Structures*. Aghia Pelaghia, Crete, Greece, 1995.

[34] O. Ouchetto, S. Zouhdi, A. Bossavit, G. Griso, B. Miara, and A. Razek, "Homogenization of structured electromagnetic materials and metamaterials," *Journal of Materials Processing Technology*, vol. 181, pp. 225-229, 2007.

[35] A. Bossavit, G. Griso, and B. Miara, "Modelling of periodic electromagnetic structures bianisotropic materials with memory effects," *Journal de Mathematiques Pures et Appliques*, vol. 84, pp. 819-850, 2005.

[36] H. S. Chen, L. X. Ran, J. T. Huangfu, X. M. Zhang, K. S. Chen, T. M. Grzegorczyk, and J. A. Kong, "Magnetic Properties of S-Shaped Split-Ring Resonators," *Progress In Electromagnetics Research*, vol. 51, pp. 231–247, 2005.

[37] H. Chen, L. Ran, J. Huangfu, T. M. Grzegorczyk, and J. A. Kong, "Equivalent circuit model for left-handed metamaterials," *Journal of Applied Physics*, vol. 100, pp. 024915-6, 2006.

[38] L. Rolf, "Electrical conductivity in inhomogeneous media," *AIP Conference Proceedings*, vol. 40, pp. 2-45, 1978.

[39] D. A. G. Bruggeman, "Berechnung verschiedener physikalischer Konstantenvon heterogenen Substanzen," *Annalen der Physik* vol. 24, pp. 636-679, 1935.

[40] G. S. Mario, "Metamaterial homogenization approach with application to the characterization of microstructured composites with negative parameters," *Physical Review B (Condensed Matter and Materials Physics)*, vol. 75, pp. 115104, 2007.

[41] H. T. Banks, V. A. Bokil, D. Cioranescu, N. L. Gibson, G. Griso, and B. Miara, "Homogenization of Periodically Varying Coefficients in Electromagnetic Materials," *Journal of Scientific Computing*, vol. 28, pp. 191-221, 2006.

[42] G. Kristensson, "Homogenization of the Maxwell equations in an anisotropic material," *Radio Science*, vol. 38, pp. 8018, 2003.

[43] D. Cioranescu, A. Damlamian, and G. Griso, "Periodic unfolding and homogenization," *Comptes Rendus Mathematique*, vol. 335, pp. 99-104, 2002.

[44] E. Cherkaev, "Inverse homogenization for evaluation of effective properties of a mixture," *INSTITUTE OF PHYSICS PUBLISHING INVERSE PROBLEMS* vol. 17, pp. 1203–1218, 2001.

[45] A. Bensoussan, J. L. Lions, and G. Papanicolaou, *Asymptotic analysis of periodic structures*. Amsterdam: North-Holland, 1978.

[46] A. F. Starr, P. M. Rye, D. R. Smith, and S. Nemat-Nasser, "Fabrication and characterization of a negative-refractive-index composite metamaterial," *Physical Review B (Condensed Matter and Materials Physics)*, vol. 70, pp. 113102, 2004.

[47] L. Zheng and W.-X. Zhang, "The effective constitutive parameters at interface of different media," *Progress In Electromagnetics Research*, vol. 51, 2005.

[48] D. R. Smith, S. Schultz, P. MarkoÅ¡, and C. M. Soukoulis, "Determination of effective permittivity and permeability of metamaterials from reflection and transmission coefficients," *Physical Review B*, vol. 65, pp. 195104, 2002.

[49] X. Chen, T. M. Grzegorczyk, B.-I. Wu, J. J. Pacheco, and J. A. Kong, "Robust method to retrieve the constitutive effective parameters of metamaterials," *Physical Review E (Statistical, Nonlinear, and Soft Matter Physics)*, vol. 70, pp. 016608-7, 2004.

[50] C. Xudong, W. Bae-Ian, K. Jin Au, and M. G. Tomasz, "Retrieval of the effective constitutive parameters of bianisotropic metamaterials," *Physical Review E (Statistical, Nonlinear, and Soft Matter Physics)*, vol. 71, pp. 046610, 2005.

[51] X. Chen and T. M. G. J. A. Kong, "Optimization approach to the retrieval of the constitutive parameters of slab of general bianisotropic medium," *Progress In Electromagnetics Research*, vol. 60, pp. 1-18, 2006.

[52] H. Chen, L. Ran, J. Huangfu, and T. M. G. J. A. Kong, "Equivalent circuit model for left-handed metamaterials," *Journal of Applied Physics*, vol. 100, pp. 024915-024920.

[53] K. Th, P. Markos, E. N. Economou, D. R. Smith, D. C. Vier, and C. M. Soukoulis, "Impact of inherent periodic structure on effective medium description of left-handed and related metamaterials," *Physical Review B (Condensed Matter and Materials Physics)*, vol. 71, pp. 245105, 2005.

[54] A. Bossavit, "Superconductivity modelling: Homogenization of Bean's model in Three Dimensions, and the Problem of Transverse Conductivity," *IEEE Transactions on Magnetics*, vol. 31, pp. 1769-1774, 1995.

[55] A. Bossavit, "Homogenizing spatially periodic materials with respect to Maxwell equations: Chiral materials by mixing simple ones," *Nonlinear Electromagnetic Systems*, pp. 564-567, 1996.

[56] A. Bossavit, "On the homogenization of Maxwell equations," *COMPEL*, vol. 14, pp. 23-26, 1996.

[57] M. El Feddi, Z. Ren, A. Razek, and A. Bossavit, "Homogenization technique for Maxwell equations in periodic structures," *IEEE Transactions on Magnetics*, vol. 33, pp. 1382-1385, 1997.

[58] A. Bossavit, "Homogenization via Harmonic Analysis," 2006, pp. 1-1.

[59] S. Spagnolo, *Convergence in Energy for Elliptic Operators*: Acedemic Press, 1976.

[60] E. D. Giorgi and S. Spagnolo, "Sulla Convergenza degli integrali delle'energia per operatori ellittici del secondo ordine," *Bollettino dell'Unione Matematica Italiana*, vol. 8, pp. 391-411, 1973.

[61] A. Cherkaev and R. V. Kohn, *Topics in Mathematical Modeling of Composite Materials*, vol. 31. Boston: Birkhauser, 1997.

[62] L. Simon, "On G-Convergence of Elliptic Operators," *Indiana University Mathematics Journal*, vol. 28, pp. 587-594, 1979.

[63] J. Rauch and M. Taylor, "Potential and Scattering Theory on Wildly Perturbed Domains," *Journal of Functional Analysis*, vol. 18, pp. 27-59, 2001.

[64] I. Babuska, *Solution of Problems with Interfaces and Singularities*. New York: Academic Press, 1974.

[65] I. Babuska, "Solution of Interfaces Problems by Homogenization, I," *SIAM Journal on Mathematical Analysis*, vol. 7, pp. 603-634, 1977.

[66] I. Babuska, "Solution of Interfaces Problems by Homogenization, II," *SIAM Journal on Mathematical Analysis*, vol. 7, pp. 635-645, 1977.

[67] I. Babuska, "Solution of Interfaces Problems by Homogenization, III," *SIAM Journal on Mathematical Analysis*, vol. 8, pp. 923-937, 1977.

[68] N. Bakhvalov and G. Panasenko, "Homogenization: Averaging Process in Periodic Media," *Mathematics and its Applications*, vol. 36, 1990.

[69] J. Keller, "Darcy's Law and the Two-Space Method," *Nonlinear Partial Differential Equations in Engineering and Applied Sciences*, pp. 429-443, 1980.

[70] E. Sanches-Palencia, "Non Homogeneous Media and VibrationTheory," in *Lecture Notes in Physics*, vol. 127: Spronger Verlag, 1980.

[71] E. Yablonovitch, "Silicon nano-photonics: where the photons meet the electrons," *Solid-State Circuits Conference, 2005. ESSCIRC 2005. Proceedings of the 31st European*, 2005, pp. 23-25.

[72] J. S. Jensen, O. Sigmund, L. H. Frandsen, P. I. Borel, A. Harpoth, and M. Kristensen, "Topology design and fabrication of an efficient double 90 photonic Crystal waveguide bend," *Photonics Technology Letters, IEEE*, vol. 17, pp. 1202-1204, 2005.

[73] S. Wang and J. Kang, "Topology optimization of nonlinear magnetostatics," *IEEE Transactions on Magnetics*, vol. 38, pp. 1029-1032, 2002.

[74] R. Courant, "Variational methods for the solution of problems of equilibrium and vibration," *Bulletin of the American Mathematica Society*, vol. 49, pp. 1-23, 1943.

[75] R. W. Clough, "The Finite Element in Plane Stress Analysis," *Proc. 2nd ASCE Conference on Electronic Computation*, Pittsburgh, PA, 1960, pp.

[76] L. A. Schmit, "Structural design by systematic synthesis," *Proc. 2nd ASCE Conference on Electric Computations*, Pittsburgh, PA, 1960, pp.

[77] O. C. Zienkiewicz, R. l. Taylor, and J. M. Too, "Reduced integration technique in general analysis of plates and shells," *International Journal for Numerical Methods in Engineering*, vol. 3, pp. 275-290, 1971.

[78] O. C. Zienkiewicz and P. D. V., "Automatic mesh generation scheme for plane and curved surfaces by 'isoparametric' coordinates
" *International Journal for Numerical Methods in Engineering*, vol. 3, pp. 519-528, 1971.

[79] A. G. M. Michell, "The limits economy in frame structures," *Philosophie Magazine*, vol. 8, pp. 589-597, 1904.

[80] G. I. N. Rozvany, "Grillages of maximum strength and maximum stiffness," *International Journal of Mechanical Sciences* vol. 14, pp. 651-666, 1972.

[81] G. I. N. Rozvany, M. Zhou, and T. Birker, "Generalized shape optimization without homogenization " *Journal of Structural Optimization*, vol. 4, pp. 250-252, 1992.

[82] G. I. N. R. N. Olhoff, K. T. Cheng, and J. E. Taylor, "On the solid plate paradox in structural optimization," *Journal of Structural Mechanics*, vol. 10, pp. 1-32, 1982.

[83] G. I. N. Rozvany, "Aims, scope, methods, history and unified terminology of computer-aided topology optimization in structural mechanics," *Structural and Multidisciplinary Optimization*, vol. 21, pp. 90-108, 2001.

[84] M. P. Bendsoe and N. Kikuchi, "Generating Optimal Topologies in Structural Design Using a Homogenization Method," *Computer Methods in Applied Mechanics and Engineering*, vol. 71, pp. 197-224, 1988.

[85] T. E. Bruns and D. A. Tortorelli, "Topology optimization of non-linear elastic structures and compliant mechanisms," *Computer Methods in Applied Mechanics and Engineering*, vol. 190, pp. 3443-3459, 2001.

[86] O. Sigmund and J. Petersson, "Numerical instabilities in topology optimization: A survey on procedures dealing with checkerboards, mesh-dependencies and local minima," *Structural Optimization*, vol. 16, pp. 68-75, 1998.

[87] B. Hassani and E. Hinton, "A review of homogenization and topology optimization I--homogenization theory for media with periodic structure," *Computers & Structures*, vol. 69, pp. 707-717, 1998.

[88] B. Hassani and E. Hinton, "A review of homogenization and topology opimization II--analytical and numerical solution of homogenization equations," *Computers & Structures*, vol. 69, pp. 719-738, 1998.

[89] B. Hassani and E. Hinton, "A review of homogenization and topology optimization III--topology optimization using optimality criteria," *Computers & Structures*, vol. 69, pp. 739-756, 1998.

[90] D. N. Dyck, D. A. Lowther, and E. M. Freeman, "A method of computing the sensitivity of electromagnetic quantities to changes in materials and sources," *IEEE Transactions on Magnetics*, vol. 30, pp. 3415-3418, 1994.

[91] J.-K. Byun and S.-Y. Hahn, "Topology optimization of electrical devices using mutual energy and sensitivity," *IEEE Transactions on Magnetics*, vol. 35, pp. 3718-3720, 1999.

[92] S. Wang and J. Kang, "Topology ootimization of nonlinear magnetostatics," *IEEE Transactions on Magnetics*, vol. 38, pp. 1029-1032, 2002.

[93] J.-K. Byun, J.-H. Lee, I.-H. Park, H.-B. Lee, K. Choi, and S.-Y. Hahn, "Inverse problem application of topology optimization method with mutual energy concept and design sensitivity," *IEEE Transactions on Magnetics*, vol. 36, pp. 1144-1147, 2000.

[94] C. S. Koh and S.-Y. Hahn, "A continuum approach in shape design sensitivity analysis of magnetostatic problems using the boundary element method," *IEEE Transactions on Magnetics*, vol. 23, pp. 1771-1774, 1993.

[95] I.-H. Park, H.-B. Lee, I.-G. Kwak, and S.-Y. Hahn, "Design sensitivity analysis for steady state eddy current problems by continuum approach," *Conference on the Computation of Electromagnetic Fields*, Miami, Fl, 1994, pp.

[96] D. N. Dyck and D. A. Lowther, "Composite microstructure of permeable material for the optimized material distribution method of automated design," *IEEE Transactions on Magnetics*, vol. 33, pp. 1828-1831, 1997.

[97] J. S. Jensen and O. Sigmund, "Systematic design of photonic crystal structures using topology optimization:low-loss waveguide bends," *Applied Physics Letters*, vol. 84, pp. 2022–2024, 2004.

[98] K.Hirayama, Y.Tsuji, T.Nomura, K.Sato, and S.Nishiwaki, "Application of topology optimization to H-plane waveguide component " *IEICE TRANSACTIONS on Electronics*, vol. 2, pp. 282–287, 2007.

[99] T. Nomura, K. Sato, K. Taguchi, and T. Kashiwa, "Topology Optimization Method for Antenna Design using FDTD Method," *IEICE Transactions on Electronics*, vol. 12, pp. 2196–2205, 2006.

[100] F. J. Villegas, T. Cwik, Y. Rahmat-Samii, and M. Manteghi, "A Parallel Electromagnetic Genetic-Algorithm Optimization (EGO) Application for Patch

Antenna Design," *IEEE Transactions on Antennas and Propagation*, vol. 52, pp. 2424-2435, 2004.

[101] D. R. Jones, "A Taxonomy of Global Optimization Methods Based on Response Surfaces," *Journal of Global Optimization*, vol. 21, pp. 345, 2001.

[102] P. Alotto, A. Caiti, G. Molinari, and M. Repetto, "A Multiquadrics Based Algorithm for the Acceleration of Simulated Annealing Optimization Procedures," *IEEE Transactions on Magnetics*, vol. 32, pp. 1198-1201, 1996.

[103] L. Lebensztajn, C. A. R. Marretto, M. C. Costa, and J. L. Coulomb, "Kriging: A Useful Tool for Electromagnetic Device Optimization," *IEEE Transactions on Magnetics*, vol. 40, pp. 1196-1199, 2004.

[104] S. Eng Swee, M. Sasena, J. L. Volakis, P. Y. Papalambros, and R. W. Wiese, "Fast parameter optimization of large-scale electromagnetic objects using DIRECT with Kriging metamodeling," *IEEE Transactions on Microwave Theory and Techniques*, vol. 52, pp. 276-285, 2004.

[105] P. Burrascano, S. Fiori, and M. Mongiardo, "Review of Artificial Neural Networks Applications in Microwave Computer-Aided Design," *International Journal of Microwave and Millimeter-Wave Computer-Aided Engineering*, vol. 9, pp. 158-174, 1999.

[106] J. Ureel, N. Fache, D. De Zutter, and P. Lagasse, "Adaptive frequency sampling of scattering parameters obtained by electromagnetic simulation," *Antennas and Propagation Society International Symposium*, Seattle, WA, USA, 1994, pp. 1162-1165.

[107] T. Dhaene, J. Ureel, N. Fache, and D. De Zutter, "Adaptive frequency sampling algorithm for fast and accurate S-parameter modeling of general planar structures," *IEEE MTT-S International Microwave Symposium Digest*, Orlando, FL, USA, 1995, pp. 1427-1430.

[108] R. Abacherli, M. Mattes, E. Suter, and J. R. Mosig, "Combining the Genetic Algorithm Approach and the Model-Based Parameter Estimation into an Adaptive Frequency Sampling Algorithm," *European Microwave Conference*, London, UK, 2001, pp. 1-4.

[109] K. Arash and D. Vijaya Kumar, "Adaptive Frequency Sampling Tools as AIDS in Electromagnetic Modeling and Design," *Canadian Conference on Electrical and Computer Engineering*, Ottawa, Canada, 2006, pp. 2326-2330.

[110] X. Lan, W. Chao-Fu, L. Le-Wei, K. Pang-Shyan, and L. Mook-Seng, "Fast characterization of microstrip antenna resonance in multilayered media using interpolation/extrapolation methods," *Microwave & Optical Technology Letters*, vol. 28, pp. 342-346, 2001.

[111] R. S. Adve, T. K. Sarkar, S. M. Rao, E. K. Miller, and D. R. Pflug, "Application of the Cauchy method for extrapolating/interpolating narrowband system responses," *IEEE Transactions on Microwave Theory and Techniques*, vol. 45, pp. 837-845, 1997.

[112] K. Kottapalli, T. K. Sarkar, Y. Hua, E. K. Miller, and G. J. Burke, "Accurate computation of wide-band response of electromagnetic systems utilizing narrow-band information," *IEEE Transactions on Microwave Theory and Techniques*, vol. 39, pp. 682-687, 1991.

[113] M. E. Tipping and N. D. Lawrence, "A variational approach to robust Bayesian interpolation," *IEEE 13th Workshop on Neural Networks for Signal Processing*, 2003, pp. 229-238.

[114] Z. Yibin, P. C. Doerschuk, and J. E. Johnson, "Symmetry-constrained 3-D interpolation of viral X-ray crystallography data," *IEEE Transactions on Signal Processing*, vol. 48, pp. 214-222, 2000.

[115] P. Fearnhead, "Exact Bayesian curve fitting and signal segmentation," *IEEE Transactions on Signal Processing*, vol. 53, pp. 2160-2166, 2005.

[116] S. F. Peik, R. R. Mansour, and Y. L. Chow, "Multidimensional Cauchy method and adaptive sampling for an accurate microwave circuit modeling," *IEEE Transactions on Microwave Theory and Techniques*, vol. 46, pp. 8, 1998.

[117] R. Lehmensiek and P. Meyer, "Creating accurate multivariate rational interpolation models of microwave circuits by using efficient adaptive sampling to minimize the number of computational electromagnetic analyses," *IEEE Transactions on Microwave Theory and Techniques*, vol. 49, pp. 12, 2001

[118] R. Lehmensiek, P. Meyer, and M. Müller, "Adaptive sampling applied to multivariate, multiple output rational interpolation models with application to microwave circuits," *International Journal of RF & Microwave Computer-Aided Engineering*, vol. 12, pp. 332-340, 2002.

[119] Y. El-Kahlout and G. Kiziltas, "An Efficient Optimization Framework for Material and Conductor Designs of Antennas," *International Conference on Electromagnetics in Advanced Applications*, Torino, Italy, 2007, pp. 555-558.

[120] A. L. Cauchy, "Sur la formule de Lagrange relative a l'interpolation," *Analyse Algebrique*.

[121] A. Garcia-Lamperez, S. Llorente-Romano, M. Salazar-Palma, and T. K. Sarkar, "Efficient electromagnetic optimization of microwave filters and multiplexers using rational models," *IEEE Transactions on Microwave Theory and Techniques*, vol. 52, pp. 508-521, 2004.

[122] A. G. Lamperez, T. K. Sarkar, and M. S. Palma, "Generation of accurate rational models of lossy systems using the Cauchy method," *IEEE Microwave and Wireless Components Letters*, vol. 14, pp. 490-492, 2004.

[123] J. Stoer and R. Bulirsch, *Introduction to Numerical Analysis*, 3 ed. New York, Berlin, Heidelberg: Springer-Verlag, 2002.

[124] Y. Ding, K.-L. Wu, and D. G. Fang, "A broad-band adaptive-frequency-sampling approach for microwave-circuit EM simulation exploiting Stoer-Bulirsch algorithm," *IEEE Transactions on Microwave Theory and Techniques*, vol. 51, pp. 928-934, 2003.

[125] Y. El-Kahlout and G. Kiziltas, "Global design optimization of complex electromagnetic devices via efficient frequency response interpolations," *IEEE International Symposium on Antennas and Propagation*, San Diego, CA. USA, 2008, pp. 1-4.

[126] A. Sihvola, *Electromagnetic Mixing Formulas & Applications*. London, UK: Institution of Electrical Engineers, 1999.

[127] J. C. M. Garnett, "Colors in metal glasses and in metal films," *Transactions of the Royal Society*, vol. 203, pp. 385-420, 1904.

[128] P. S. Neelakanta, *Handbook of Electromagnetic Materials*. FL: CRC, 1995.

[129] O. Wiener, "Zur Theorie der Refraktionskonstanten," *Berichte über die Verhandlungen der Königlich-Sächsischen Gesellschaft der Wisseschaften zu Leipzig,*, vol. 62, pp. 256-277, 1910.

[130] Z. Hashin and S. Shtrikman, "A Variational Approach to the Theory of the Effective Magnetic Permeability of Multiphase Materials," *Journal of Applied Physics*, vol. 33, pp. 3125-3131, 1962.

[131] D. J. Bergman, "Bounds for the complex dielectric constant of a two-component composite material," *Physical Review B*, vol. 23, pp. 3058, 1981.

[132] D. J. Bergman, "Hierarchies of Stieltjes Functions and Their Application to the Calculation of Bounds for the Dielectric-Constant of a 2-Component Composite Medium," *Siam Journal on Applied Mathematics*, vol. 53, pp. 915-930, 1993.

[133] A. H. Sihvola, "How strict are theoretical bounds for dielectric properties of mixtures?," *Geoscience and Remote Sensing, IEEE Transactions on*, vol. 40, pp. 880-886, 2002.

[134] S. Torquato, *Random Heterogeneous Materials: Microstructure and Microscopic Properties*. Berlin: Springer, 2002.

[135] A. K. Sen and S. Torquato, "Effective conductivity of anisotropic two-phase composite media," *Physical Review B*, vol. 39, pp. 4504, 1989.

[136] C. Engstrom, "Bounds on the effective tensor and the structural parameters for anisotropic two-phase composite material," *Journal of Physics D: Applied Physics*, vol. 38, pp. 3695-3702, 2005.

[137] B. Beche and E. Gaviot, "A new formulation to shape the concept of bounds in effective dielectric tensors for superlattices with two directions of periodicity," *Journal of Physics A: Mathematical and General*, vol. 38, pp. 11157-10067, 2005.

[138] G. Kiziltas and Z. N. Wing, "Automated fabrication of three dimensional dielectric composites for RF applications," *IEEE Antennas and Propagation Society International Symposium and USNC/URSI National Radio Science*, Albuquerque, USA, 2006, pp.

[139] R. Gajic, R. Meisels, F. Kuchar, and K. Hingerl, "Refraction and rightness in photonic crystals," *Optics Express*, vol. 13, pp. 8596-8605, 2005.

[140] M. Notomi, "Negative refraction in photonic crystals," *Optical and Quantum Electronics*, vol. 34, pp. 133-143, 2002.

[141] C. Luo, M. Ibanescu, S. G. Johnson, and J. D. Joannopoulos, "Cerenkov Radiation in Photonic Crystals," *Science*, vol. 299, pp. 368 - 371, 2003.

[142] S. O'Brien and J. B. Pendry, "Magnetic activity at infrared frequencies in structured metallic photonic crystals," *Journal of Physics: Condensed Matter*, vol. 14, pp. 6383-6394, 2002.

[143] G. Mumcu, K. Sertel, and J. L. Volakis, "Miniature Antennas and Arrays Embedded Within Magnetic Photonic Crystals," *IEEE Antennas and Wirelss Propagation Letters*, vol. 5, pp. 168-172, 2006.

[144] E. Yablonovich, "Inhibited Spontaneous Emission in Solid-State Physics and Electronics," *Physical Review Letters*, vol. 58, pp. 2059, 1987.

[145] A. Figotin and P. Kuchment, "Band-Gap Structure of the Spectrum of Periodic Dielectric and Acoustic Media. I. Scalar model," *SIAM Journal on Applied Mathematics*, vol. 56, pp. 68-88, 1996.

[146] A. Figotin and P. Kuchment, "Band-Gap Structure of the Spectrum of Periodic Dielectric and Acoustic Media. II. 2D Photonic Crystals," *SIAM Journal on Applied Mathematics*, vol. 56, pp. 1561-1620, 1996.

[147] A. Figotin and I. Vitebsky, "Nonreciprocal magnetic photonic crystals," *Physical Review E*, vol. 63, pp. 066609, 2001.

[148] A. Figotin and I. Vitebskiy, "Electromagnetic unidirectionality in magnetic photonic crystals," *Physical Review B*, vol. 67, pp. 165210, 2003.

[149] G. Mumcu, K. Sertel, J. L. Volakis, I. Vitebskiy, and A. Figotin, "RF Propagation in Finite Thickness Unidirectional Magnetic Photonic Crystals," *IEEE Transactions on Atennas and Propagation*, vol. 53, pp. 4026-4034, 2005.

[150] G. Mumcu, K. Sertel, and J. L. Volakis, "Superdirective miniature antennas embedded within magnetic photonic crystals," *Antennas and Propagation Society International Symposium, 2005 IEEE*, 2005, pp. 10-13 vol. 2A.

[151] G. Mumcu, K. Sertel, J. L. Volakis, I. Vitebskiy, and A. Figotin, "RF propagation in finite thickness nonreciprocal magnetic photonic crystals," *Antennas and Propagation Society International Symposium, 2004. IEEE*, 2004, pp. 1395-1398 Vol.2.

[152] R. A. Chilton and R. Lee, "Chirping unit cell length to increase frozen-mode bandwidth in nonreciprocal MPCs," *Microwave Theory and Techniques, IEEE Transactions on*, vol. 54, pp. 473-480, 2006.

[153] R. A. Chilton, J. Kyung-Young, R. Lee, and F. L. Teixeira, "Frozen Modes in Parallel-Plate Waveguides Loaded With Magnetic Photonic Crystals," *Microwave Theory and Techniques, IEEE Transactions on*, vol. 55, pp. 2631-2641, 2007.

[154] J. Han and M. Kamber, *Data Mining: Concepts and Techniques*. Simo Fraser University: Morgan Kaufmann Publisher, 2001.